

**Two-Dimensional Material-Based Nanosensors for Detection of
Low-Molecular-Weight Molecules**

Yibo Zhu

Submitted in partial fulfillment of the
requirements for the degree of
Doctor of Philosophy
in the Graduate School of Arts and Sciences

COLUMBIA UNIVERSITY

2018

© 2018
Yibo Zhu
All rights reserved

ABSTRACT

Two-Dimensional Material-Based Nanosensors for Detection of Low-Molecular-Weight Molecules

Yibo Zhu

Low-molecular-mass small molecules play important roles in biological processes and often serve as disease-related biomarkers for diagnosis. Accurate detection of small molecules remains challenging for conventional sensors due to their limited sensitivities. Two-dimensional (2D) materials, thanks to their atomic level thickness, can be extraordinarily sensitive to external perturbations and therefore well-suited for sensing applications. This dissertation explores the use of 2D materials, including primarily graphene and transition metal dichalcogenides, in the detection of low-molecular-weight and low-charge molecules.

This work starts with the study of methods that allow for efficient and clean transfer of graphene grown on Cu using chemical vapor deposition (CVD), which is a critical step for achievement of large-area and high-quality graphene for device fabrication. In addition to the conventional wet-etching transfer method, we have studied on the method of electrochemical delamination, which is more time-efficient and allows for recycling of the Cu foil. Generation of bubbles during the electrochemical reaction is minimized by tuning the experimental parameters, thereby minimizing transfer-induced damages to graphene.

We then fabricate the graphene-based field effect transistor (FET) and use the graphene FET as biosensors. First, the sensor is configured as an electrolyte-gated FET. With appropriate biochemical functionalization of the graphene, the FET sensors have been used to detect multiple small-molecule biomarkers including glucose and insulin via their affinity binding with receptors. Then, on a flexible substrate, we demonstrate real-time measurement of tumor necrosis factor alpha, a signal protein that regulates immune cells. We then simplified the sensor structure using a bottom local-gate to replace the external electrode as required in the previous electrolyte gated FET. Using the bottom local-gated FET sensor we have carried out real-time monitoring of the variation of pH in solutions.

In addition to the electrical sensors, highly sensitive and multifunctional plasmonic sensors have also been developed by combining the unique optical properties of graphene with engineered metallic metasurfaces. The plasmonic sensors operating in mid-infrared region are configured as either metallic metasurface or hybrid graphene-metallic metasurface. Using a metallic metasurface, we demonstrate simultaneous quantification and fingerprinting of protein molecules. Using a hybrid graphene-metallic metasurface, we demonstrate optical conductivity-based ultrasensitive biosensing. In contrast to refractive-index-based sensors, the sensitivity of the hybrid metasurface sensor is not limited by the molecular masses of analytes. A monolayer of the sub-nanometer chemicals can be readily detected and differentiated on the hybrid metasurface. Reversible detection of glucose is carried out via the affinity binding of glucose with boronic acid immobilized on the graphene of the hybrid metasurface. The lowest detection limit achieved in our work is 36 pg/mL, which is considerably lower than that for the existing optical sensors.

Despite the high sensitivity of graphene, the zero band-gap of graphene fundamentally impedes its use in digital electronic devices. In contrast, two-dimensional semiconductors, such as transition metal dichalcogenide (TMDC) with non-zero band gaps, holds great potential for developing practical electronic devices and sensors. Monolayers of TMDC materials are particularly attractive for development of deeply scaled devices, although the contact resistance between metal and the monolayer TMDC has been so large to significantly limit the performance of the devices. We present a high-performance monolayer MoS₂ FET with a monolayer graphene as bottom local gate. The graphene gate is found to significantly improve the dielectric strength of the oxide layer compared to the lithographically patterned metal gate. This in turn allows for the use of very thin gate dielectric layer (~5 nm) and application of a strong displacement field to lower the contact resistance. Benefiting from the low contact resistance, the monolayer MoS₂ FET offers a high on/off ratio (10⁸) and low subthreshold slope (64 mV/decade). Additionally, thanks to the highly efficient electrostatic coupling through the ultrathin gate dielectric layer, short-channel (50 nm and 14 nm) devices are realized that exhibit excellent switching characteristics.

In summary, this dissertation presents significant contributions to 2D material-based electronic and optoelectronic nanosensors, especially for detection of small molecules. Perspectives are made in the end of the thesis, on future studies needed to realize practical applications of these sensors and other 2D material-based products.

TABLE OF CONTENTS

List of Figures	iv
List of Tables	xiii
Acknowledgements	xiv
Dedication	xvi
Chapter 1. Introduction	1
1.1 Biochemical sensors	1
1.1.1 Nanomaterial-based biosensors	2
1.1.2 Affinity biosensors	4
1.2 Two-dimensional materials	6
1.2.1 Physical properties of two-dimensional materials	6
1.2.2 Benefits of two-dimensional materials for biosensing	8
1.3 Research scope and goals	12
1.4 Thesis outline	13
Chapter 2. Preparation and characterization of graphene	15
2.1 Introduction to growth and transfer of large-area graphene	16
2.1.1 Chemical vapor deposition of monolayer graphene	16
2.1.2 Wet and dry transfer methods	17
2.2 Electrochemical delamination transfer method	19
2.2.1 Principle and setup	19
2.2.2 Transfer procedure	21
2.3 Characterization of transferred graphene	22
2.3.1 Optical microscopy of graphene	22

2.3.2 Raman spectroscopy of graphene	23
2.3.3 Atomic force microscopy of graphene	24
2.4 Chapter summary	25
Chapter 3. Graphene field effect sensors	27
3.1 Introduction to field effect sensors	27
3.1.1 Principle of field effect biosensing	27
3.1.2 Review of field effect biosensors	28
3.2 Solution-gate graphene field effect sensors	31
3.2.1 Device design and fabrication	31
3.2.2 Affinity based glucose detection	32
3.2.3 Real-time monitoring of insulin level	46
3.2.4 Tumor necrosis factor alpha sensing on flexible substrate	51
3.3 Bottom local-gate graphene field effect sensors	53
3.3.1 Sensor design and fabrication	55
3.3.2 Real-time monitoring of solution pH level	57
3.4 Chapter summary	62
Chapter 4. Graphene-metallic metasurface plasmonic sensors	64
4.1 Introduction to plasmonic sensors	64
4.1.1 Standard surface plasmonic resonance sensor	64
4.1.2 Refractive-index based localized plasmonic sensors	65
4.2 Metallic metasurface based mid-infrared sensors	67
4.2.1 Sensor design and fabrication	68
4.2.2 Quantification and fingerprinting of Immunoglobulin G	69

4.3 Graphene-metallic hybrid metasurface based sensors	72
4.3.1 Sensor principle, design and fabrication	74
4.3.2 Detection of monolayer small-size chemical molecules	76
4.3.3 Detection of sub-nanometer metallic nanoparticles	81
4.3.4 Reversible measurement of glucose	83
4.3.5 Dependence of sensitivity on metasurface geometry	86
4.3.6 Enhancement of molecule vibrational fingerprints	92
4.4 Chapter summary	93
Chapter 5. Graphene bottom local-gated molybdenum disulfide transistors	95
5.1 Introduction to transition metal dichalcogenide	95
5.1.1 Preparation of two-dimensional transition metal dichalcogenide	96
5.1.2 Electrical properties of transition metal dichalcogenide	97
5.2 Field effect transistors with graphene bottom local gate	98
5.2.1 Device design and fabrication	99
5.2.2 Electrical characterization	102
5.2.3 Short-channel transistors	106
5.2.4 Device performance on flexible substrate	108
5.3 Chapter summary	109
Chapter 6. Conclusions and perspectives	111
6.1 Summary of contributions	111
6.2 Future work	112
Bibliography	114

List of Figures

Figure 1.1: Applications of biosensors in different fields. [Adapted from http://menon.us]	1
Figure 1.2: Schematic of atomic structure of single-layer graphene.	6
Figure 1.3: Potential applications based on graphene and other 2D materials. [Adapted from D. Akinwande, <i>et al.</i> Nature Communication, 2014.]	7
Figure 1.4: Band structures of graphene and MoS ₂ monolayers. (a) atomic structure and band diagram of monolayer graphene. (b) Atomic structure and band diagram of monolayer MoS ₂ . ·	8
Figure 1.5: Comparison of atomic structures of 0D fullerene, 1D carbon nanotube and 2D graphene, all of which consist of carbon atoms. [Adapted from D.M. Guldi <i>et al.</i> Chemical Communications, 2011.]	9
Figure 1.6: Illustration of effects of material specific surface area on sensitivity.	10
Figure 2.1: Procedure of CVD graphene synthesis on Cu foil. Inset: Photograph of a Cu foil after graphene growth.	16
Figure 2.2: Dry transfer process of CVD graphene.	17
Figure 2.3: Wet transfer process of CVD graphene.	18
Figure 2.4: Setup for electrochemical delamination transfer of graphene.	20
Figure 2.5: A delaminated PMMA/Graphene (size 1 cm ²) layer floating on water.	21
Figure 2.6: Photograph of monolayer graphene transferred on rigid substrates: (a) 285 nm thick SiO ₂ and (b) glass slide.	22
Figure 2.7: Microscope photo of transferred graphene using EC delamination. (a) A large complete single crystal graphene. (b) A specifically selected local area showing wrinkles, single and bilayers.	23

Figure 2.8: Example of a microscopy photo and corresponding Raman spectra of monolayer graphene. 24

Figure 2.9: Atomic force microscopy of transferred CVD monolayer graphene on polished SiO₂.
 (a) AFM image of as-transferred graphene after PMMA dissolved in acetone (left), and after annealing at 350 degree celcius for 4 hours in Ar/H₂ forming gas (right). (b) Thickness of the graphene monolayer after anealling. The average step height of 3.6 nm is approaching the thickness of exfoliated monolayer graphene. 25

Figure 3.1: Schematics of a field effect transistor. 27

Figure 3.2: Examples of field effect biosensors based on 1D materials. (a) Silicon nanowire gas sensors. [Adapted from J. Kong et al. Science, 2000.] (b) Carbon nanotube sensors of detection of DNA. [Adapted from C. Staii et al. Nano Letters, 2005.] (c) Study of binding kinetics of molecules using silicon nanowire field effect biosensors. [Adapted from X. Duan, et al. Nature Nanotechnology, 2012.] 29

Figure 3.3: Example of graphene field effect sensors. (a) Gas sensor capable of detecting individual gas molecules. [Adapted from F. Schedin et al. Nature Materials, 2007.] (b) Sensor array for detection of biomolecules. [Adapted from N. Gao et al. PNAS, 2016.] 30

Figure 3.4: Schematic of the nanosensor configured as a solution-gated graphene field effect transistor. An Ag/AgCl electrode inserted into the solution served as the gate electrode, while the electrical double layer at the solution-graphene interface served as the gate capacitor. 31

Figure 3.5: (a) Micrograph of a fabricated device. The graphene conducting channel connected the source and drain electrodes. (b) Coupling of boronic acid and graphene via π - π stacking interactions between the pyrene group and graphene. (c) Formation of a glucose-boronate ester at a physiological pH of 7.4. 34

Figure 3.6: Transfer characteristics of the pristine graphene and the PBA-functionalized graphene. Dashed lines: Transfer characteristics of the pristine graphene exposed to glucose solutions (0.1 mM to 25 mM). Solid lines: Transfer characteristics after rinsing with PBA solution. V_{NP} shifted from 0.33 V to 0.575 V. Legend: Glucose concentrations. 35

Figure 3.7: Raman spectra of the graphene before and after exposure to PBA solution. (a) Signature peaks of the boronic acid and the graphene-pyrene interaction were observed after immersing in PBA solution. (b) Fitting of the measured 2D band to the Lorentz equation. 36

Figure 3.8: Characterization of graphene using Raman spectroscopy (a) after immersing in 1 mM boric acid solution, (b) after immersing in 1 mM PBA solution. 37

Figure 3.9: Influence of solution replenishment on transfer characteristics measurements. In the two measurements when fresh buffer was added to the device, the source-drain current at each gate voltage as well as the neutral point voltage were highly coincident. 39

Figure 3.10: Transfer characteristics measured when the device was exposed to glucose solutions (concentration ranging from 2 μ M to 25 mM). The curve shifted to the left as a result of the increase in the glucose concentration. Inset: Monotonic decrease of I_{DS} at $V_{GS} = 0.4$ V. .. 40

Figure 3.11: Transfer characteristics measured with glucose solutions on the butyric acid functionalized graphene. The n-type doping induced by PBTA remained unchanged when the sensor was exposed to glucose. 41

Figure 3.12: Neutral point voltage shift ratio $\Delta V_{NP,G}/\Delta V_{NP,B}$ as a function of glucose concentration. Glucose concentration is on logarithmic scale. Inset: Inset: The solid line is a fit to the Hill-Langmuir equation, yielding an equilibrium dissociation constant (K_D) of 38.6 μ M. Glucose concentration is on linear scale. 42

Figure 3.13: Measurements of fructose using 9-anthracene-boronic acid (ABA) as receptor. The p-doping induced by boronic acid, and the n-doping upon glucose binding were qualitatively consistent with the observations in glucose measurements using PBA. 44

Figure 3.14: Measurements of fructose using PBA as receptor. The p-doping induced by boronic acid, and the n-doping upon glucose binding were comparable to the observations in glucose measurements. 45

Figure 3.15: Principle of the graphene nanosensor for insulin detection. The sensing surface is prepared through Schiff-base reaction between aptamer IGA3 and the graphene immobilized PASE linker. The aptamer specifically binds to insulin in the sample solution, promoting the formation of both parallel and anti-parallel G-quadruplex, which brings negatively charged insulin and DNA strands to the close vicinity of graphene surface, causing disturbances to the carrier concentration in the bulk of graphene and yielding detectable signals. 47

Figure 3.16 Detection of insulin using the aptameric nanosensor. (a) Transfer characteristics measured when the aptamer-functionalized graphene was exposed to insulin solutions (concentration: 100 pM to 1 μM). The transfer characteristic curve shifted to the left as a result of the increase of the insulin concentration. 49

Figure 3.17: Real-time measurement of insulin concentration changes. The responses are demonstrated by the changes of the drain-source current I_{ds} 50

Figure 3.18: Device design and measurement setup of the flexible graphene FET sensor. 52

Figure 3.19: Transfer characteristics measured when the aptamer-functionalized graphene, in flat (a) and bent (b) status, exposed to TNF- α solutions (concentration: 5 nM to 500 nM). The transfer characteristic curve shifted to the left as a result of the increase of the TNF- α concentration. 53

Figure 3.20: Schematic of the graphene-based FET nanosensor. Graphene serves as the conducting channel, while a 20-nm-thick HfO₂ layer between the graphene and the substrate-supported gate electrode serves as the dielectric layer. 54

Figure 3.21: Fabricated sensors. Left: Photograph of a 4-inch wafer on which the devices were fabricated. Right: Microscopic photo of close-up of the channel region. 55

Figure 3.22: Transfer characteristic of the bottom local-gate graphene FET in air. 56

Figure 3.23: Dependence of the nanosensor characteristics on pH. (a) Transfer characteristic curves obtained at varying pH values. The $V_{SG, DP}$ shifts linearly to higher gate voltages with increasing pH (57.6 mV/pH). (b) Dependence of the Dirac point voltage on pH. The solid line represents a linear fit. 57

Figure 3.24: Independence of transconductance of the pH levels. 58

Figure 3.25: Schematics of the coupling effect between the C_{LG} and C_{SG} 60

Figure 3.26: Real time measurements of pH: the source-drain current I_{DS} varied consistently and reversibly with pH at a fixed gate voltage ($V_{SG} = 0.75$ V). 61

Figure 4.1: Schematics of the setup of a standard SPR sensor. [Adapted from M. Copper *et al.* Nature Reviews, 2002.] 64

Figure 4.2: Two modes of the LSPR sensors: bulk refractive index sensing and local refractive index-based molecular sensing. [Adapted from K. Mayer *et al.* Chemical Reviews, 2011.] 66

Figure 4.3: Sensor design. (a) Schematics of the sensor without graphene. (b) Scanning electron microscope photo of the fabricated sensor. Scale bar 1 μ m. (c) Close-up of the circled region in (b). The gaps between neighboring antenna nanorods were approximately 30 nm. 68

Figure 4.4: Top view of the electrical field distribution over a pair of gold antenna nanorods, calculated using finite-difference time-domain (FDTD) simulation. The near field is strongly confined in the close vicinity of the gold nano-antennas. 69

Figure 4.5: Detection of IgG. (a) Amide I and II bands after immobilization of monolayer protein A/G. (b) Shift of plasmon resonance caused by the binding of IgG and protein A/G. 70

Figure 4.6: Fitting of the data points to the Langmuir isotherm yields a dissociation constant ~ 1.1 nM. 71

Figure 4.7: Increase in the intensity of amide I band confirmed successful binding of IgG. 72

Figure 4.8: Schematic illustration and microscopy characterization of the hybrid metasurface. (a) Schematic of the graphene-metallic metasurface, with pyrene groups adsorbed on the graphene surface. (b) Optical micrograph of the device. 74

Figure 4.9: (a) Scanning electron microscopy photo of the nanorod antennas coated by monolayer graphene. Inset: Close-up image of the graphene suspended over the 30 nm nanogap. (b) Optical absorbance of the metasurface with as-transferred graphene. 75

Figure 4.10: Detection of sub-nanometer chemical molecules. (a) Chemical structure of ACN, AP, and BAP. (b) Raman spectroscopy of graphene treated by different chemicals. (c) Characterization of the carrier doping (Δn) using field effect transistors. (c) Shift of the plasmonic resonance frequency by the molecular doping. (d-f) Dependence of the amount of resonance shift on the carrier density. 77

Figure 4.11: Influence of carrier density and mobility to the absorption spectroscopy of the metasurface. (a) Dependence of the amount of resonance shift on the carrier density. (b) Independence of the Q factor of the carrier mobility. (c) Equivalent circuit model of the metasurface. (d) Frequency response of the current I_{tot} 78

Figure 4.12: Calculation of the effective graphene inductance and resistance in the circuit model. Frequency dependent inductance L_G (a) and resistance R_G (b) at $n=1 \times 10^{12} \text{cm}^{-2}$ and different mobilities. 80

Figure 4.13: Detection of 0.8 nm Al nanoparticles. (a) Characterization of carrier doping of Al particles. Inset: Bandgap diagram before and after deposition of Al. (b) Measurement results on pure Au metasurface. (c) Measurement results on hybrid metasurface. (d) Comparison of the results. Inset: SEM photo of the deposited Al nanoparticles on graphene. 82

Figure 4.14: Control experiments on pure metallic metasurface functionalized with boronic acid. (a) Schematics of sensor configuration. (b) Measurement results. 83

Figure 4.15: Quantitative measurements of glucose on the hybrid metasurface. (a) Configuration of the hybrid metasurface sensor. (b) Measurement of glucose from 2 nM to 20 mM on the hybrid metasurface. (c) FET characterization of the n-doping introduced by glucose-boronic acid binding. (d) Dependence of $|\Delta\omega_r|$ on the glucose concentration. (e) Langmuir fitting of the measured $|\Delta\omega_r|$. (f) Reversible measurement of glucose. Each data point is the average of 9 measurements on three devices and the error bar represents the standard deviation. 85

Figure 4.16: Dependence of the sensitivity on antenna geometry. Left: SEM photos of rod, disk and diamond antennas. Gap length $g=30$ nm. Scale bars, 100 nm. Right: Comparison of the relative shifts obtained with different geometries. 86

Figure 4.17: Near-field simulation for three antenna geometries. Left: pure metallic antennas. Right: Graphene-coated antennas. 88

Figure 4.18: Study of the effects of the gap size on the sensitivity. (a) SEM photos of rod antennas with $g=30$, 100, and 200 nm. (b) Comparison of the relative shifts obtained with

different gap sizes. (c) Near-field simulation for $g=100$ and 200 nm. (d) Plots of $|\Delta\omega_r/\omega_{r0}|$ and K at $\Delta n=10^8\text{cm}^{-2}$ for different antenna geometries. 90

Figure 4.19: Further improvement of sensitivity by shrinking the gap length. (a) Fabrication process of the 10 nm gap between neighboring antennas. (b) SEM photos of a pair of antennas at each step of fabrication. (c) Comparison of the sensitivities for $g=30$ and 10 nm. (d) Detection of 200 pM glucose with $g=10$ nm. 91

Figure 4.20: Enhancement of glucose fingerprints. Optical absorption (ΔR) measured before and after drop-coating (a) 500 picomolar and (b) 50 picomolar glucose on the device. 93

Figure 5.1: Device structure and characterization. (a) Schematic of the graphene bottom local-gate MoS₂ field effect transistor. (b) Microscopy photo of the MoS₂ dry-transferred onto the graphene/HfO₂. Inset: Raman mapping of the MoS₂ A1g band (green) and the graphene 2D band (red). (c) Raman spectroscopy of the MoS₂ and graphene. (d) Optical micrograph of the fabricated devices with graphene gate (upper) and metal gate (lower). Scale bars: 1 μm . (e) Measurement of the gate leak current through the dielectric layer of different thickness, on graphene gate electrodes. (f) Breakdown field and voltage for the graphene gated devices as a function of the dielectric thickness. 100

Figure 5.2: Fabrication process of the device. (a) Patterning of the graphene ribbon. (b) Gate voltage dependent conductivity of the patterned graphene ribbon. (c) Aligned transfer of the CVD monolayer MoS₂. 102

Figure 5.3: Comparison of device geometries and extraction of contact resistance. (a) Schematics and transport characteristics of the partially gated and fully gated devices. The channel lengths of both devices were 1.5 μm . $T_{\text{Hf}} = 16$ nm. (b) Extraction of R_C using transmission line method for the graphene gated device. Four channels with various channel

lengths (0.4, 0.6, 0.8 and 1 μm) were fabricated on a same MoS_2 flake. Inset: Gate voltage dependence of R_C . Error bars represent the standard error of the linear fitting. 103

Figure 5.4: Electrical characterization of device performance. (a) – (c) Characterization of devices with $T_{\text{Hf}} = 16$ nm. (a) Output curves (I_{DS} as a function of V_{DS} at different V_{GG}) for a 600 nm long channel. V_{GG} increased from 0 to 9.5 V in 0.5 V steps, and then to 9.8 V. (b) Transport characteristics of a 400 nm channel. Inset: Transconductance g_m as a function of V_{GG} . (c) Field effect carrier mobilities (without exclusion of the contact resistance) at different channel length. (d) – (e) Transport characteristics of a device with $T_{\text{Hf}} = 8$ nm and $L_{\text{Ch}} = 1.5$ μm . (d) I_{DS} plotted in logarithmic scale, showing a SS of 64 mV/decade. Inset: zoom-in of the subthreshold regime; and (e) I_{DS} plotted in linear scale with V_{DS} increased up to 1 V and V_{GG} up to 1.7 V, which led to a high on/off ratio of 1.8×10^8 . Both (d) and (e) show very small hysteresis. 105

Figure 5.5: Characterization of short-channel devices. SEM photo and transport characteristics of a 50 nm channel (a-b) and a 14 nm channel (c-d). $T_{\text{Hf}} = 2.5$ nm. The SS was 73 mV/decade for the 50 nm channel and 86.5 mV/decade for the 14 nm channel. (e) On/off ratio as a function of V_{DS} . The on/off ratio decreased with V_{DS} for both channels, reflecting that the source and drain electrodes started to control the channel conductance. 107

Figure 5.6: Characterization of the device fabricated on flexible PEN substrate. (a) Upper: Optical micrograph of the MoS_2 transferred on graphene gate. Lower left: High contrast micrograph for visualization of the MoS_2 flake and graphene gate. Lower right: Photograph of a fabricated device. (b) Transport characteristics of the device on flexible substrate. 109

List of Tables

Table 1-1: Comparison of 1D, 2D and 3D materials for biosensing application.	11
Table 4-1: Parameter setup for simulation of the equivalent circuit.	81

Acknowledgements

I would like to express my sincerest thanks to my family, colleagues and friends, whose kind help and support have been indispensable throughout my doctoral study.

First, I would like to thank my PhD advisors, Dr. Qiao Lin and Dr. James Hone, personally and professionally, for their invaluable, never-ending support and inspiring guidance. I appreciate the opportunity provided by Dr. Lin to join Columbia University and his laboratory. Starting from the first day of joining the group, Dr. Lin has introduced me to a microscopic world involving electronics, mechanics and biology, where he has guided me to discover research interests, launch research projects, and publish research results, without reservation. He also generously introduces me to my co-advisor Dr. Hone, who gives me access to a fantastic nano-world. In discussion with Jim, I have learned so much about the nanomaterials, from experimental techniques to theoretical knowledge. His smiling face and enthusiasm has motivated me to explore more possibilities in the laboratories.

It is so fortunate that I can collaborate with Dr. Nanfang Yu and his student Zhaoyi Li, whose expertise, patience and generosity made it possible for me to create metasurface biosensors in their brand-new laboratory. Their detailed and vivid illustrations have allowed me to understand many physical processes I never heard about.

I am also thankful to Dr. Qian Wang at the University of South Carolina and his students Enoch Adogla and Yok Maturavongsadit, for their help with organic chemistry.

I was delighted, at early stages of my doctoral study, to be able to work under the supervision of more senior researchers, Dr. Yufeng Hao and Dr. Cheng Wang. Their experiences and stories equipped me with more intelligence and courage in the pursuit of higher academic goals.

Moreover, I would like to thank other members of the Lin lab. They are Jing Zhu, Yuan Jia, Zhuang Hao, Yijun Li, Jaeyoung Yang, Bing Song, Timothy Olsen, Hao Sun, Xuejun Wang, Dongyang Wang, Yihan Zhang, Zhixing Zhang, and Chao Su. I also would like to thank other members of the Hone lab, Cheng Tan, Ghidewon Arefe, Christopher DiMarco, Nick Petrone, Lei Wang, Changjian Zhang, Xian Zhang, Fan Zhang, Xu Cui, Bumho Kim, Younghun Jung, Sanghoon Chae, Young Duck Kim, Baichang Li, Nate Finney, Junqiang Hu, Yuanda Gao, Dongjea Seo, Mufeng Hu, Daniel Rhodes, and Xiaochi Liu. I also appreciate the help of Jaeun Yu, Qizhi Xu, and Boyuan Zhang from the lab of Dr. Collin Nuckolls with device characterization.

I cannot forget to thank my girlfriend, Shiqi Wang, for her company at the challenging times of my research. I am so lucky and proud that she always trusts in me and stands with me. I also have to thank my good brothers, Xue Liu and Dexi Wang, who have always been there whenever I need them since my high-school time. I also thank my relatives who have helped my parents handle so many things when I am thousands of miles away from my lovely hometown.

Last but not least, I am very grateful to my parents, Ailian Zhang and Qiusheng Zhu. Their selfless, unconditional love, support, and encouragement are the reason why I am able to finish all my study and complete this dissertation.

To my parents

Chapter 1

Introduction

1.1 Biochemical sensors

Biochemical sensors, or biosensors in the context of this thesis, are devices used for detection of biochemical analytes. A biosensor typically consists of two major parts including a biological element and a transducer unit. The biological element, derived using chemical or biological methods, are responsive to a specific analyte or a category of analytes via physical interactions or chemical reactions. The transducer serves as a component to convert the responses of the biological element to detectable signals, and eventually readable information.

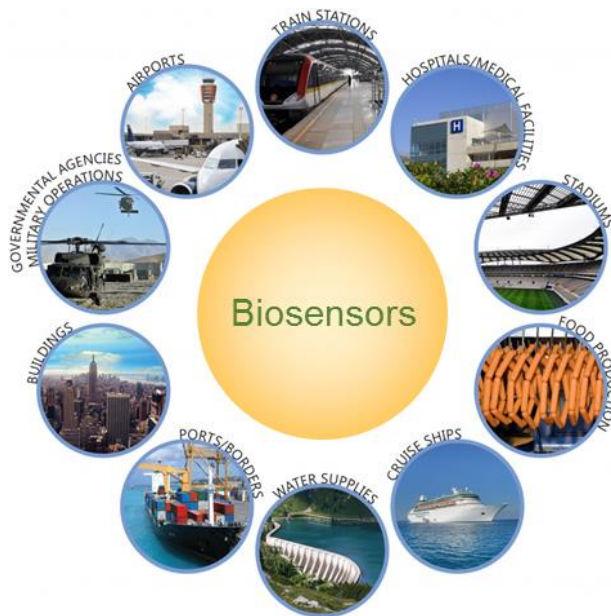


Figure 1.1: Applications of biosensors in different fields. [Adapted from <http://menon.us>]

Biosensors are important for both fundamental research and practical applications (Figure 1.5).

Sensitive and accurate quantification and identification of biochemical samples would be a

prerequisite for most biological and chemical studies, especially for those related to pharmaceutical engineering and nanobiology¹. Biosensors are also used in hospitals for monitoring physiological parameters and levels of biochemical analytes to evaluate the health condition of patients. Early diagnosis of disease also relies on accurate and sensitive detection of related biomarkers. In addition, biosensors also find applications in inspection of safety-related analytes such as hazardous additives, poisons and explosives.

1.1.1 Nanomaterial-based biosensors

Conventional biosensing methods in clinical and research laboratories, such as enzyme-linked immunosorbent assay (ELISA), mostly require professionally trained personnel in handling of biological samples, operation of instruments, and interpretation of measurement results, and are therefore not well-suited to personal daily use. Some of them, such as standard surface plasmonic resonance (SPR) biosensors have encountered insufficient sensitivity in detection of certain low-molecular-weight analytes and cannot satisfy the requirement in advanced biological and chemical researches². To overcome these limitations, researchers have strived to develop miniaturized, sensitive and rapidly responsive biosensors. Some of the new-generation biosensors employ nanomaterials as the transducers, which in size are comparable to the nanometric target analytes, therefore can more efficiently interact with the analytes and sense the weak perturbances. For example, localized surface plasmon resonance (LSPR) sensors, based on nanoengineered metamaterials, have significantly improved the sensitivity over the standard SPR devices. Field effect biosensors that use semiconducting nanomaterials as transducing units also demonstrate higher sensitivities to biomolecules, chemical and gas molecules than traditional biosensors. Below is a brief review of biosensors that are based on nanomaterials, covering the

most commonly used electrical methods and optical methods, including electrochemical reaction, field effect, impedance, piezoelectricity and plasmonic resonance-based sensors.

Electrochemical sensors rely on the oxidation or reduction of the analytes that involves transfer of electrons and generation of currents. Catalysis such as enzymes can be added to facilitate the reaction and speed the sensor response. Decoration of the metal electrodes with nanomaterials such as metal nanoparticles³, or use of conducting nanomaterials (e.g. carbon nanotube)⁴ as electrodes proved to significantly improve the sensitivity by increasing the effective area for analyte adsorption and reaction. Electrochemical sensors have been so far successfully miniaturized and commercialized for portable and implantable applications, particularly in the continuous glucose monitoring, although the need of enzyme and the dependence on the oxygen concentration makes the sensors accuracy susceptible to variations of external environmental conditions. Other than the electrochemical sensors, the nanomaterials, combined with the affinity binding of receptor and target molecules, have also enabled sensitive detection using impedance-based sensors. Measurement of the impedance of a dielectric as a function of the analyte concentration made it possible to quantify the analytes without generating significant current and therefore amenable to sensing principles other than the electrochemical method. For example, affinity binding of glucose to the boronic acid confined by polymer solution or hydrogel was found to change the impedance of the solution or the hydrogel⁵, thereby allowing for electrical based continuous monitoring of the glucose level without the need of enzymes. Piezoelectric materials, which can output electrical power upon mechanical deformation, provided unique opportunities to develop self-powered biosensors^{6,7}. Binding of charged molecules on the piezoelectric materials, for example the ZnO nanowires⁸, can vary the surface charge density of

the materials, and hence enable self-powered biosensing. Due to the large charges needed to influence the properties of the nanowires, this method is in general only applicable to large and highly charged molecules.

On the other hand, for optical sensors, the sub-wavelength dimension of the nanomaterials and artificial nanostructures offer unique opportunities to control and confine the light. Metasurfaces, consisting of engineered nanostructures, proved to be able to strongly enhance the interaction between the electro-magnetic field and the adsorbed biomolecules, which in turn improved the sensitivity of plasmonic resonance-based sensors. Moreover, also based on the metasurfaces, the surface enhanced Raman spectroscopy (SERS)^{9,10} and surface enhanced infrared absorption spectroscopy (SEIRAS)^{11,12} can reveal the spectral fingerprints of molecules to facilitate identification of analytes. A more detailed introduction to the optical sensors would be given in Chapter 4.

1.1.2 Affinity biosensors

In contrast to the electrochemical reactions which irreversibly consume the analytes, affinity binding represents non-covalent intermolecular interactions such as hydrogen bonds and van de Walls force. The reversible affinity binding between analytes and receptors, without converting the analytes into other materials, is appropriate to develop reusable biosensors and allows for more accurate quantification of the analytes. The specificity of the sensor is also improved by use of receptors that selectively bind to the target molecules. Commonly used receptors in affinity sensor include antigen/antibody, aptamers and some low-molecular-wright biochemical

molecules. Usually, the affinity binding involves complex physiochemical process; conventional affinity assays such as ELISA can be time-consuming.

Use of nanomaterials as transducers can drastically improve the response speed and simplify the assay setup. Specifically, a very thin layer or even monolayer of receptor molecules is immobilized on the surfaces of nanomaterials for recognition of target molecules. The nanomaterials with high sensitivity to weak perturbation allows them to significantly and rapidly respond to the affinity binding of target molecules to the receptors. The high sensitivity also makes it possible to detect low-molecular-weight analytes without use of more complex assay such as competitive assay. Various biosensors including optical, electrical, mechanical and magnetic biosensors have been developed with improved sensitivity, selectivity and robustness. For example, the real-time transduction of the binding process between protein and receptors using silicon nanowire field effect transistors revealed the binding kinetics and allowed determination of the binding parameters such as equilibrium constant¹. Similarly, binding kinetics and affinity constant of DNA hybridization have been studied using the multichannel graphene field effect transistors at single-base level¹³. The supramolecular binding between glucose and boronic acid also allows for colorimetric quantification of glucose by immobilizing boronic acid on the metallic nanoparticles¹⁴. Employing metallic nanoparticles enhanced fluorescence, highly sensitive fluorescent biosensors are also developed to detect the acetylcholinesterase inhibitors¹⁵. Use both of the two-dimensional graphene and engineered metallic metasurfaces, a multimode affinity sensor that detects the variations in graphene conductivity, mechanical resonator resonance frequency and the plasmonic resonance frequency has been reported¹⁶.

1.2 Two-dimensional materials

Two-dimensional (2D) nanomaterial refers to materials consisting of a single layer or a few layers of atoms, of which the thickness is less than one or several nanometers. Since the discovery of graphene^{17,18}, the first 2D material consisting of single-layer carbon atoms in hexagonal lattice (Figure 1.1), many other materials have been added to the 2D material category, and a lot of important physical properties unique to the 2D system have been demonstrated. Applications based on the 2D materials have also emerged in different fields and brought up improvements in the performance of optoelectronic devices or energy storage¹⁹⁻²².

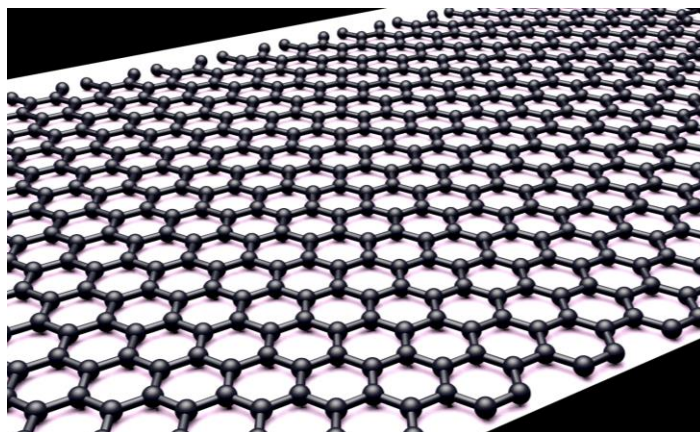


Figure 1.2: Schematic of atomic structure of single-layer graphene.

1.2.1 Physical properties of two-dimensional materials

The ultrathin thickness of the 2D materials make them exhibit extraordinary mechanical, electrical and optical properties. The monolayer graphene is proved to be highly flexible, transparent, and conductive. It owns the highest Young's modulus (~ 1 TPa)²³ among the existing materials. In visible light region, the optical absorption of monolayer graphene is only 3%. It also shows extremely high carrier mobility above 10^4 $\text{cm}^2\text{V}^{-1}\text{s}^{-1}$ at room temperature²⁴. Therefore,

graphene has become a very strong candidate for development of energy-efficient nano-mechanical-electrical-systems, flexible and wearable devices²⁵, for applications such as integrated circuits, portable electronics, personal healthcare devices, and nanobiology study (Figure 1.2).



Figure 1.3: Potential applications based on graphene and other 2D materials. [Adapted from D. Akinwande, *et al.* Nature Communication, 2014.]

The zero-bandgap of single-layer graphene makes it a semimetal. Experimental studies also demonstrate that the conductivity of graphene can only be tuned in a limited range by the electrical field, typically within one order of magnitude^{17,18}. Thus, the monolayer graphene is unfortunately not appropriate for development of logic circuits. Instead, the transition metal dichalcogenide (TMDC) 2D layers are semiconductors with non-zero band gaps²⁶⁻²⁸. Particularly, the monolayer molybdenum disulfide (MoS_2), a most widely studied 2D TMDC, has a direct

band-gap (E_g) of 1.8 eV (Figure 1.3)²⁹. The MoS₂ has therefore enabled exploration of digital logic devices based on atomically thin materials.

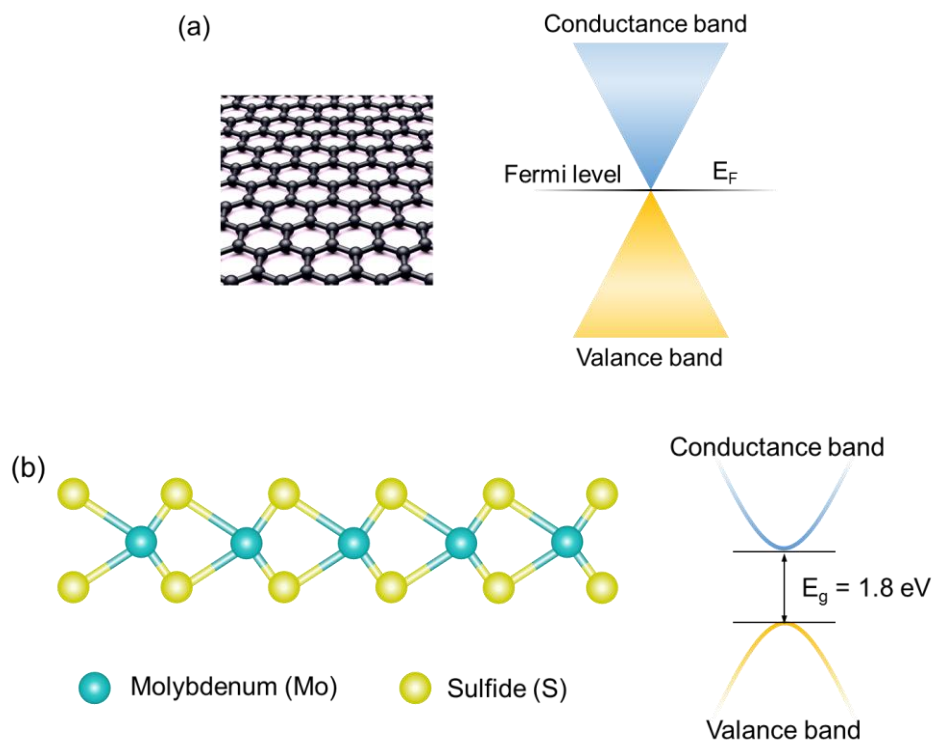


Figure 1.4: Band structures of graphene and MoS₂ monolayers. (a) atomic structure and band diagram of monolayer graphene. (b) Atomic structure and band diagram of monolayer MoS₂.

1.2.2 Benefits of two-dimensional materials for biosensing

The long-lasting interest in nanomaterials comes from the increasing demands that cannot be fulfilled by conventional bulk materials. For example, the number of transistors on a single microprocessor chip is expected to continuously increase for higher performance of computers, but rather challenging for existing silicon-based fabrication technologies. Thus, the search for alternative materials that can perform desirable functions within even smaller space and cost less energy is urgent. Before the emergence of 2D materials, other nanomaterials including the one-

dimensional (1D) carbon nanotube (CNT) and silicon nanowire (SiNW), as well as zero-dimensional (0D) fullerene and quantum dots (Figure 1.4), have already attracted much attention and demonstrated certain unique functionalities of nanomaterials.

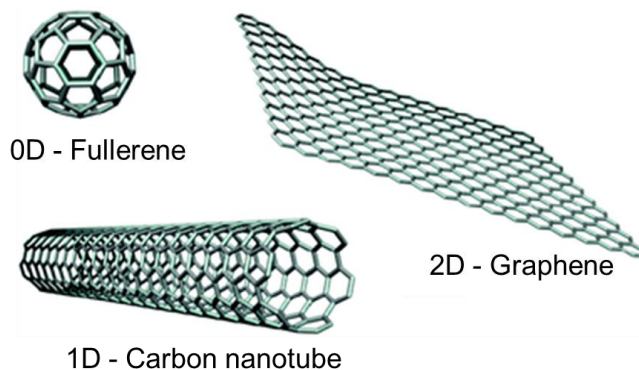


Figure 1.5: Comparison of atomic structures of 0D fullerene, 1D carbon nanotube and 2D graphene, all of which consist of carbon atoms. [Adapted from D.M. Guldi *et al.* Chemical Communications, 2011.]

Nevertheless, the preparation and manipulation of 0D materials generally is difficult and requires confinement using solution, hydrogels and other bulk materials. In contrast, 1D materials which can be extended along one direction make them optically visible, and amenable to modern micro and nanofabrication processes. In the past two decades, the optoelectronic properties of 1D materials have been intensively studied. Progress is still being made on the highly scaled electronic devices toward commercialization of the devices, which appears challenging due to the difficulties in preparing highly ordered, high-density 1D materials with uniform properties over large area³⁰. Hence, the planar 2D structure would be more desirable in the sense that it is unlimitedly extendable over the two-dimensional space, while the few-atom thickness allows for the retainment of significant and unique properties of nanomaterials. The 2D materials are not

only amenable to fabrication of scalable nanodevices, but also enables exploration of some quantum effects that otherwise are not possible.

In addition to the scalability needed for device fabrication, the 2D materials can also deliver higher sensitivity and thus very promising for sensor applications. In a biosensor, given the same biological sensitive elements (e.g. a same antibody), the sensitivity of the sensor will be determined by the transducer units, or the properties of the materials composing the transducer. Although the sensitivities of different sensing principles and different materials vary a lot from each other, in general the nanomaterials show higher sensitivity than bulk materials, in particular when the receptors are only immobilized on the outer surface of the material³¹. This is because that the nanomaterials, due to their small unit volumes, typically own large specific surface area (SSA), defined as the total surface area per unit mass (m^2/g).

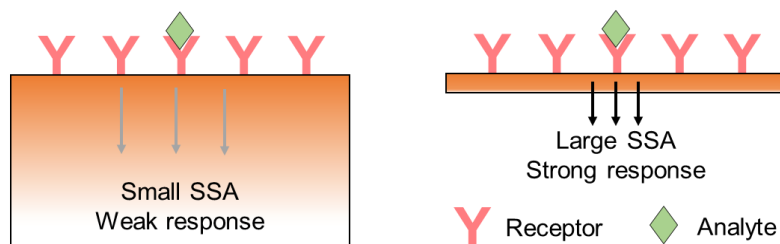


Figure 1.6: Illustration of effects of material specific surface area on sensitivity.

For the analytes adsorbed at the material surface, the influence of these analytes on the material properties would decrease with the distance from the surface. Note that the measured signals reflect the changes of the properties of the entire material rather than that at the surface, therefore the larger the SSA is, the stronger the measured responses would be (Figure 1.5). Comparison of the SSA of bulk carbon ($<900 \text{ m}^2/\text{g}$), CNT ($100 - 1000 \text{ m}^2/\text{g}$) and graphene ($\sim 2600 \text{ m}^2/\text{g}$) found

that SSA of monolayer graphene is much higher than the other two. This should also be applicable to other 2D materials, which therefore become ideal materials for developing biosensors (Table 1-1).

Table 1-1: Comparison of 1D, 2D and 3D materials for biosensing application

Materials	Sensitivity	Device fabrication	Device scalability
3D bulk materials	Low	Possible	Low
1D materials (e.g. carbon nanotube)	High	Possible but challenging	Possible but process-wise challenging
2D materials (e.g. graphene)	High	(I) low-cost mass production (II) planar structures easy to pattern and integrate	High

On the other hand, scalable fabrication of the devices would be prerequisite of commercialization of the biosensors. While scalable synthesis of carbon nanotubes is possible, the electrical properties (semiconducting or metallic) of the nanotubes have not been precisely controlled and the nanotube density is relatively low. In contrast, the wafer-scale growth of monolayer graphene and transition metal dichalcogenide have been demonstrated, together with the time and cost-efficient transfer methods. Characterization of their electrical and optical properties revealed high quality of these materials, making the 2D materials well-suited for development of scalable biosensors and other devices.

1.3 Research scope and goals

Based on the introduction to the state of the art for biochemical sensors, the unique mechanical, chemical and optoelectronic properties of 2D materials holds strong potential to overcome certain limitations for existing biosensors. Research on 2D materials based biosensors have also demonstrated their functionality in detection of different analytes, from gas molecules, to deoxyribonucleic acid (DNA) and biomolecules. However, most of these works have focused on examination of the sensor performance based on quantification of electrically charged biomarkers or polarized molecules, while it remains challenging to detect the small molecules with weak or no charges. Also, the biology elements and sensing principles have mostly been adapted from existing biosensor, thus some of the issues associated with the conventional sensing principles await to be addressed. The thesis would be focused on use of 2D materials in detection of analytes that are difficult to measure on conventional platforms, especially the analytes with low-molecular-weight and low-charges, as well as exploration of new sensing principles with the 2D materials.

The research goals and tasks are briefly listed below:

- (1) Preparation of large-area high-quality 2D materials and fabrication of devices.
- (2) Detection of small molecules with low molecular mass, especially those carrying low electric charges or non-charged molecules.
- (3) Understanding of the interaction of biochemical molecules with 2D materials.
- (4) Exploration of novel sensing principles based on the unique properties of 2D materials, which are other difficult, if no possible, to be realized with other materials.

1.4 Thesis outline

Chapter 2 of this thesis introduces the preparation and characterization of large area graphene, which is a key step to obtaining high-performance devices. In this chapter, we mainly develop an electrochemical delamination transfer method of CVD graphene grown on copper. This method significantly reduces the costs of time and materials, as well as damages to graphene during the transfer process.

Starting from Chapter 3 the thesis details the progress in detection of small molecules using the graphene FET sensors, based on the affinity binding between the small molecules with their receptors. This method shortens the response time and alleviates the influences of environmental conditions on sensor functionality. This chapter first focuses on proof-of-principle on conventional solution-gate FET sensors, and then presents a bottom local-gate configured graphene FET sensor that is more compact and integrable.

In Chapter 4 we introduce plasmonic biosensors using both graphene and metasurface, e.g. engineered nanostructures for control of electromagnetic fields on demand. The plasmonic sensors operating in mid-infrared regime enable single measurement-based analyte quantification and identification. When graphene is loaded, the tunable optical conductivity of graphene makes the hybrid metasurface an ultrasensitive plasmonic sensor, whose detection limit is independent of the molecular-mass and therefore drastically improved compared to conventional refractive index-based plasmonic sensors.

Chapter 5 presents a FET with monolayer MoS₂ as the semiconducting channel and monolayer graphene as a bottom local gate electrode. This device shows significant improvements in more than one parameters in the transport characteristics. Potentially it not only can function as highly sensitive biosensors, but also serve as logic unit in next-generation electronic devices. Finally, the contributions of this thesis and plan of future works are summarized in Chapter 6.

Chapter 2

Preparation and characterization of graphene

Graphene was discovered as the first 2D materials in 2004, by mechanical exfoliation from the bulk graphite onto the SiO₂ substrates. The small flakes of graphene, typically few micrometers long and wide, have shown ultrahigh room-temperature carrier mobility ($>10^4 \text{ cm}^2\text{V}^{-1}\text{s}^{-1}$), excellent optical transparency ($>97\%$) as well as great mechanical strength (Young's modulus $>1\text{TPa}$). While these extraordinary physical properties of the single-atom-thick material have attracted huge attention for industries in different fields, from electrical, optical to energy and environmental, use of graphene in practical applications has been impeded by the low efficiency in exfoliation of graphene and the large variance in quality of the mechanically isolated flakes. Therefore, chemical based controllable and precise synthesis of the graphene has been important to make people practically benefit from this new material. Among the different methods, chemical vapor deposition (CVD)³²⁻³⁴, one of the earliest studied and most widely used, has allowed for achievement of large-area monolayer graphene while not significantly degrading its physical properties. Since the CVD graphene is usually synthesized on substrates made of specific materials such as germanium and copper³⁴⁻³⁷, to use the CVD graphene for desired purposes it is required to transfer the graphene from the growth substrate to different target substrates. Due to the single-atom thickness, graphene is extremely sensitive to external influences, mechanical or chemical. Therefore, it is difficult to transfer the large area graphene intact, continuous and clean, and with low cost of time and materials. This chapter will introduce

the progress we have made in transfer of CVD graphene grown on copper foil, with focus on the optimization of the direct delamination of graphene based on the electrochemical reactions.

2.1 Introduction to growth and transfer of large-area graphene

2.1.1 Chemical vapor deposition of monolayer graphene

CVD of graphene involves pyrolysis of carbon-source materials to achieve disassociated carbon, and then formation of the atomic structure of graphene. Usually, a catalysis is applied to reduce the temperature and time required for this process, for example, metal, such as copper (Cu) in graphene growth. The process of the graphene CVD procedure is done in a tube furnace, starting with heating of the furnace under protection of argon (Ar) to approximately 1000 degree Celsius and annealing of Cu in hydrogen (H_2) environment sequentially. Then the carbon source gas methane (CH_4) is introduced for reaction, followed by cooling down under protection of Ar (Figure 2.1).

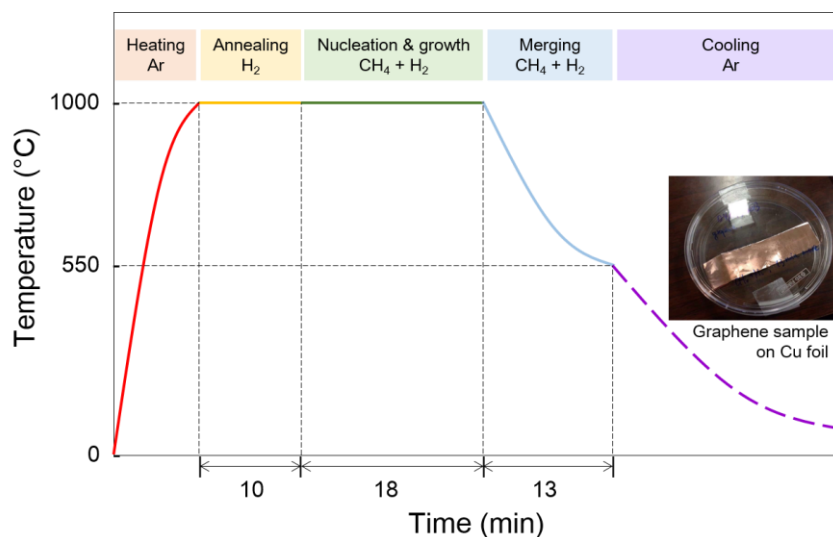


Figure 2.1: Procedure of CVD graphene synthesis on Cu foil. Inset: Photograph of a Cu foil after graphene growth.

2.1.2 Wet and dry transfer methods

To make use of the CVD graphene, different transfer methods have been developed to release the monolayer graphene from the growth substrate and transfer it onto desired substrate. Using a polymer layer, such as poly(methyl methacrylate) (PMMA) as a supporting layer has been found most effective to facilitate the transfer without excessive damage to graphene^{38,39}. The PMMA layer can be used in either dry transfer and wet transfer processes as detailed in the following.

Dry transfer process: After graphene growth, 500 nm PMMA was spin-coated on top of graphene/Cu foil for protection. A stamp made of polydimethylsiloxane (PDMS) was attached by pressing. The copper foil was removed by wet etching in copper etchant. The exposed graphene was cleaned and blow-dried, and then transferred onto the substrate. The PMMA stamp was released from the PMMA/graphene layer at 170 °C (Figure 2.2). Finally the protection PMMA layer on graphene was dissolved in organic solvents.

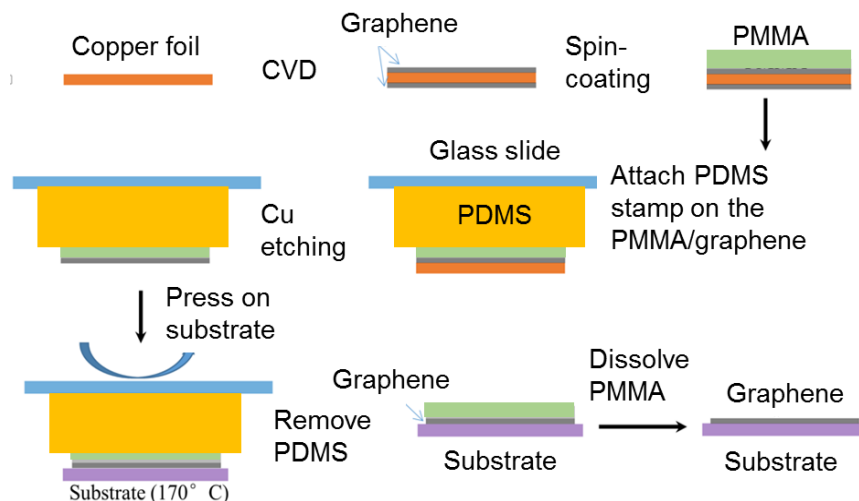


Figure 2.2: Dry transfer process of CVD graphene.

Wet transfer process: A protection polymer layer (PMMA 495K A4) was firstly spin-coated on graphene. The Cu foil was then etched in Cu etchant. The backside of the PMMA/Gr layer was then triple-cleaned by floating on DI water bath, then directly transferred on the substrate and allowed to dry at room temperature. After 45 min baking at 170 °C the PMMA layer was dissolved in acetone bath.

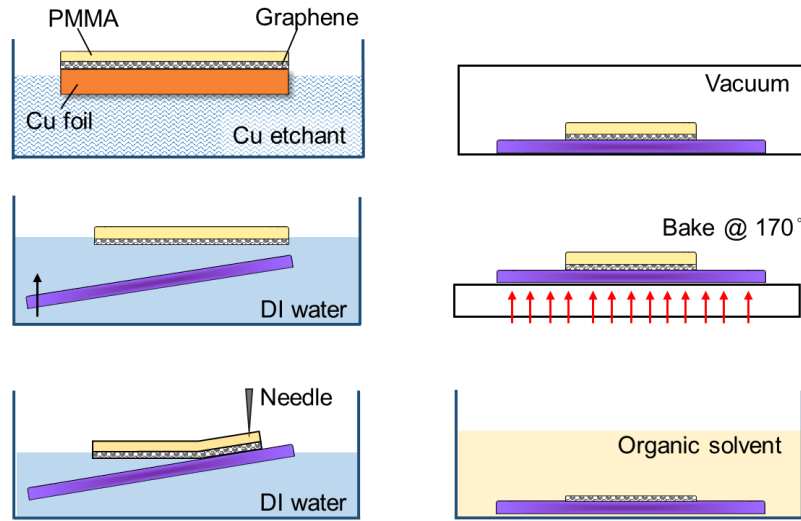


Figure 2.3: Wet transfer process of CVD graphene.

To compare two different transfer methods, we evaluate their performance in completeness, cleanness, handling difficulties and costs of time. For the dry transfer method, it allows for aligned-transfer of the graphene under the assistance of the PDMS/glass stack. But due to the mechanical force applied on the graphene during attaching and removing the PDMS stamp, the transferred graphene may be mechanically damaged. In contrast, the wet transfer methods can deliver very continuous graphene but it is difficult to accurately control the position of the graphene/PMMA when scoping it in water. Both of these two methods, due to the need of removing the copper substrate using chemical etching, irreversibly consume the copper and take long time.

2.2 Electrochemical delamination transfer method

The high costs of time and materials make the conventional wet and dry transfer methods not amenable to mass production of graphene. In contrast, direct delamination of graphene that does not require etching of the Cu substrate is more promising. Due to the strong Van der Waals force between the graphene and the Cu foil, mechanically peeling the graphene off the Cu will be very difficult and can generate large damages to graphene. It is therefore more realistic to “peel” the graphene off using chemical methods. It was found that the gaseous H₂ bubbles would be generated at the interface of Cu and graphene when the Cu was configured as the cathode in an electrolysis cell. The H₂ bubbles force separation of graphene from the Cu and hence allows for transfer of graphene, which is called electrochemical delamination (ECD) transfer or “bubble” transfer⁴⁰. In this way, the Cu can be recycled after the transfer and reused for future growth. Unfortunately, even with polymeric support layer, such as PMMA, the bubbles would still cause severe damages to the graphene.

2.2.1 Principle and setup

Recently, researchers have noticed that a very thin the oxide layer of Cu (Cu₂O) can be formed because the oxygen in air can permeate to the surface of Cu through the graphene domain boundaries, defects or wrinkles, which are frequently present on the CVD graphene. Given that reduction of copper oxide can take place at a lower potential than that for hydrogen evolution, it is possible to separate the graphene from Cu by selective removing the natural oxide layer sandwiched in between of graphene and Cu. Some works have been reported on reducing the damages in EC delamination of graphene⁴¹, but they only explore use of the costly platinum as

the anode electrode and NaCl as electrolyte. Here we demonstrate bubble-free ECD transfer with less expensive Cu as both the anode and cathode.

As introduced above, the bubble-free ECD transfer is based on selective reduction of the oxide layer on the Cu surface and release of graphene from the growth substrate. In the EC reaction ($\text{Cu}_2\text{O} + \text{H}_2\text{O} + 2\text{e}^- \rightarrow 2\text{Cu} + 2\text{OH}^-$), the Cu_2O is reduced to Cu, which minimizes the consumption and allows recycle of Cu. The experimental setup is compact, consisting of Cu anode, PMMA/graphene/Cu cathode, power source with tunable outputs and some accessories such as cables and clips (Figure 2.4). The PMMA/graphene/Cu is then connected to the negative output of the power supply while a Cu foil is connected to the positive end and secured on a positioner for convenient control. Here we use aqueous alkali solution (sodium hydroxide, NaOH, 1 M) as the electrolyte. In this electrolyte, it only contains Na^+ , H^+ and OH^- , which will not introduce significant doping or damage to graphene.

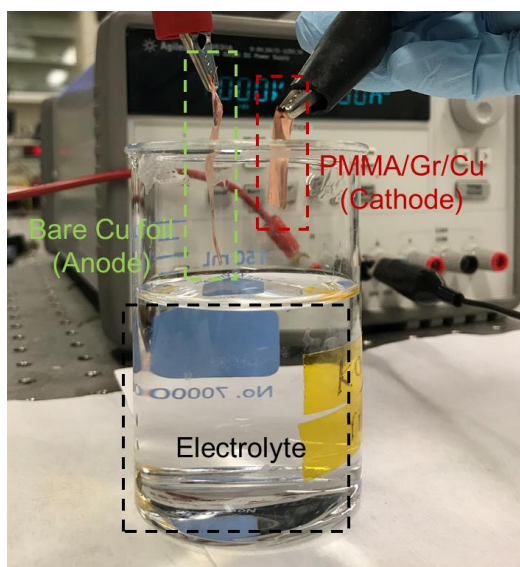


Figure 2.4: Setup for electrochemical delamination transfer of graphene.

2.2.2 Transfer procedure and results

Similar to the previously introduced transfer methods, first a polymer layer (PMMA 495K) is spin-coated on graphene as a supporting layer. It is critical to choose correct potential and process speed. For the unreferenced, two-electrode cell, the delamination is expected to start at a voltage of approximately 2 V, which may vary for different sizes of graphene and concentrations of the NaOH, and needs to be tested for specific conditions to obtain best transfer results. First the Cu anode secured on the positioner is inserted into the electrolyte, and the bottom end of the cathode PMMA/Gr/Cu is allowed to touch the electrolyte. Once the delamination starts, the cathode foil is proceeded to finish the delamination. The PMMA/Gr layer released using this method is clean, transparent and continuous without bubbles (Figure 2.5). The PMMA/Gr layer is then moved to fresh deionized water to remove any NaOH on the backside and then transferred to the target substrate by scoping in water. The water sandwiched between the graphene and the substrate is forced to rapidly evaporate in vacuum for overnight. The substrate is then baked at 180 degree Celsius for 1 hour. Finally the PMMA is removed in organic solvent such acetone and chloroform.

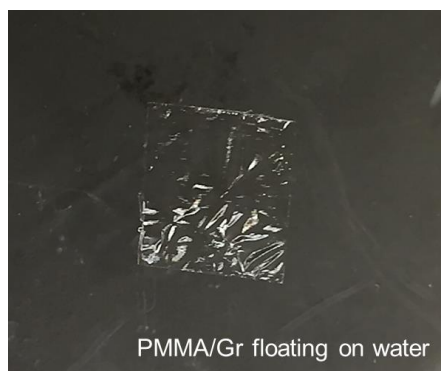


Figure 2.5: A delaminated PMMA/Graphene (size 1 cm²) layer floating on water.

The monolayer graphene is clearly visible at specific optical conditions. Usually it can be directly observed using bare eyes on oxidized Si substrate with 285 nm thick SiO₂ (Figure 2.6), although on transparent substrate (e.g. glass) it is much more difficult to visualize monolayer graphene. Here the optical microscopy (OM), Raman spectroscopy and atomic force microscopy (AFM) are used to characterize the layer numbers and quality of the graphene.

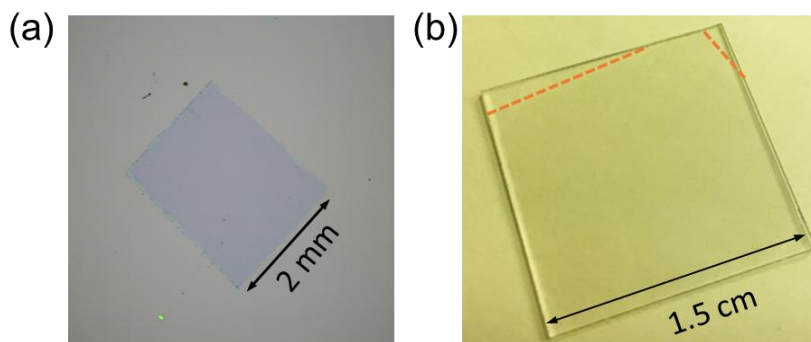


Figure 2.6: Photograph of monolayer graphene transferred on rigid substrates: (a) 285 nm thick SiO₂. (b) glass slide.

2.3 Characterization of transferred graphene

2.3.1 Optical microscopy of graphene

While during synthesis of graphene the experimental conditions have been selected to grow monolayer graphene, sometimes bilayer or even few layer graphene may appear at the center of the crystal. Additional graphene layers beyond the single layer, if any, typically appear as small grains in isolated local regions, and can be easily identified on the basis of the brightness and contrast under an optical microscope when transferred onto a 285-nm thick SiO₂ coated silicon substrate (Figure 2.7). Wrinkles, cracks or other deformation or defects of graphene sometimes can also be recognized on the OM when they are not smaller than few micrometers.

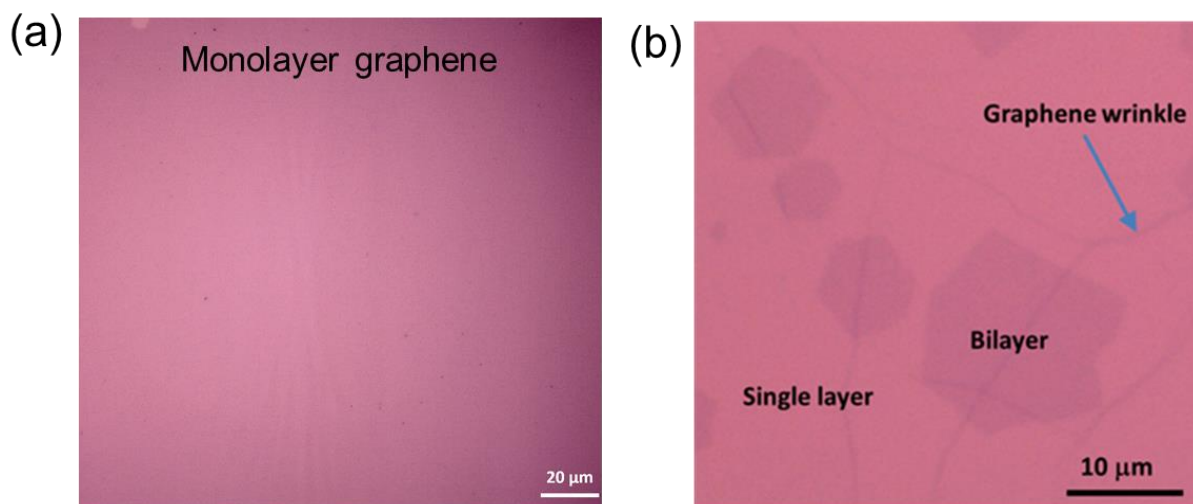


Figure 2.7: Microscope photo of transferred graphene using EC delamination. (a) Continuous monolayer graphene. (b) A specifically selected local area showing wrinkles, single layer and bilayers of graphene.

2.3.2 Raman spectroscopy of graphene

The monolayer graphene, when examined using Raman spectroscopy, should show two or three bands, including a G band around 1587 cm^{-1} attributable to the in-plane vibrational of the sp^2 hybridized carbon atoms, a 2D band around 2680 cm^{-1} due to a two-phonon lattice vibration, and sometimes a D band around 1350 cm^{-1} known as disorder band and represents defects of graphene or presence of a ring in the proximity of graphene. The Raman spectra are measured at multiple positions on the graphene sample using an exciting laser of 532 nm. The large ratio of the peak intensities of 2D band to G band (>2) is strong evidence of monolayer graphene⁴². D-band around 1350 cm^{-1} is not observed at majority of the sample, although we see D-band at some local positions (Figure 2.8) affected by impurities or residues during transfer, which should not impact use of graphene in our applications.

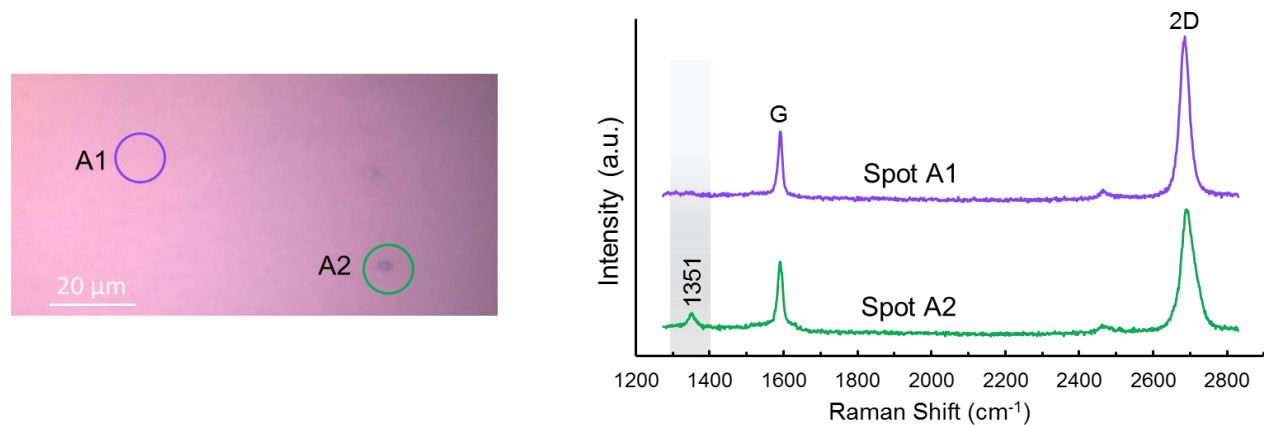


Figure 2.8: Example of a microscopy photo and corresponding Raman spectra of monolayer graphene.

2.3.3 Atomic force microscopy of graphene

Atomic force microscopy (AFM) is widely used to characterize the topography and thickness of the 2D materials⁴³⁻⁴⁵. Usually mechanically exfoliated 2D flakes including graphene exhibit smoother surface than transferred CVD materials. This is because defects and wrinkles can form during synthesis and transfer of the CVD materials. For example, the organic residue such as PMMA will adsorb on the surface of graphene and cannot be completely removed using organic solvents, which has been a key factor degrading the electrical properties of graphene. The roughness of the as-transferred CVD graphene are typically above 1 nm and the thickness is also 1 or 2 nm, larger than expected values as observed on mechanically exfoliated layers. High-temperature annealing under protection of H₂ and Ar, or in ultra-high vacuum can further clean the graphene surface (Figure 2.9)^{46,47}. Removing of the polymer layer using even stronger organic solvents, or using alternative polymers to PMMA can also effectively improved the surface roughness of the transferred graphene^{24,48-50}.

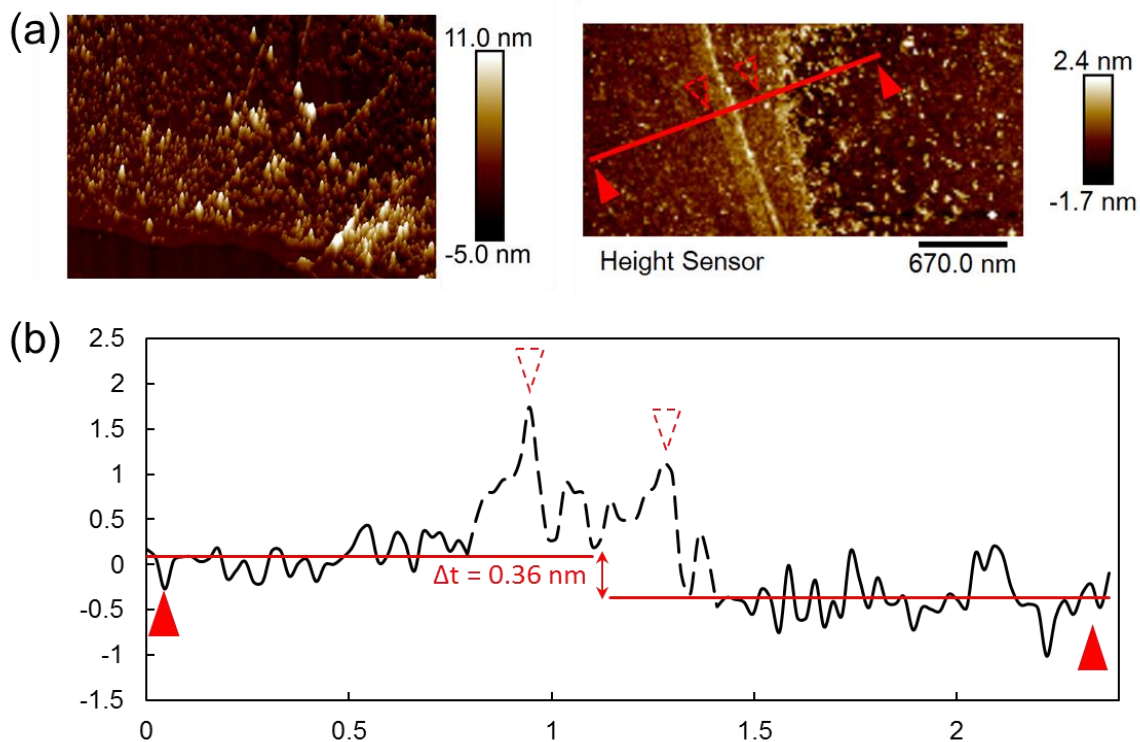


Figure 2.9: Atomic force microscopy of transferred CVD monolayer graphene on polished SiO₂. (a) AFM image of as-transferred graphene after PMMA dissolved in acetone (left), and after annealing at 350 degree celcus for 4 hours in Ar/H₂ forming gas (right). (b) Thickness of the graphene monolayer after anealling. The average step height of 3.6 nm is approaching the thickness of exfoliated monolayer graphene.

2.4 Chapter summary

In this chapter we introduced the procedure of preparation of graphene using CVD method on Cu foil as well as transfer of the graphene to desired substrates. To overcome some drawbacks of conventional transfer methods, we have explored and optimized electrochemical delamination transfer. The EC delamination transfer is more time efficient and allows for recycling of the Cu. To minimize the damages to graphene during transfer process we have modified the existing EC

delamination procedure to minimize generation of bubbles between Cu and graphene during transfer, and reduce contact of graphene with ions other than OH^{-1} and H^{+} groups.

The layer number and quality of graphene are characterized using optical microscopy and Raman spectroscopy, which indicate high-quality monolayer graphene. Atomic force spectroscopy is used to characterize the topography and layer number of the CVD graphene. Due to the adsorption of polymer residue on graphene surface, further cleaning such as annealing may be required for applications sensitive to nanoscale contaminants. Improvements of the transfer methods as well as the CVD growth process, should continue to be made to achieve better completeness, cleanness, flatness of the graphene⁵¹.

Chapter 3

Graphene field effect sensors

3.1 Introduction to field effect sensors

3.1.1 Principle of field effect biosensing

Semiconducting materials are the basis for development of field effect transistors because their electrical conductivities are tunable by external electrical field. The conductivity (σ) of a material is determined by the product of its carrier density and mobility:

$$\sigma = (n\mu_e + p\mu_h)q$$

where, σ is the conductivity, n represents the density of electrons, μ_e represents the electron mobility, p is the density of holes, μ_h is the hole mobility and q is the elementary charge.

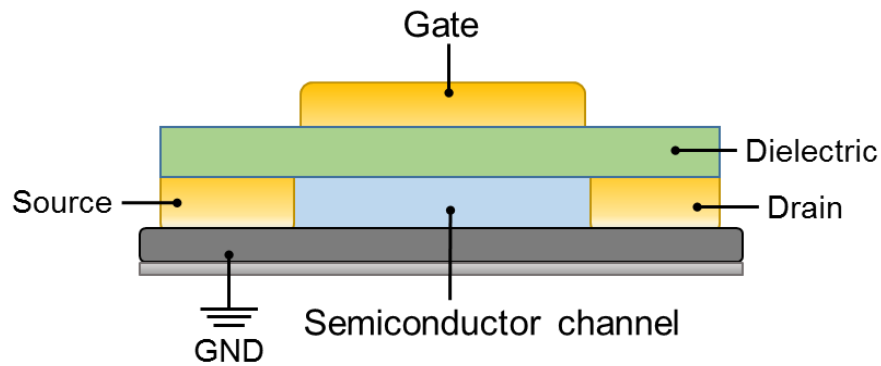


Figure 3.1: Schematics of a field effect transistor

When configured as a field effect transistor (FET, Figure 3.1), the conductivity can be altered by applying a gate voltage through a dielectric layer, as a result of modulation of the carrier density:

$$I_D = \mu_{eff} C_G (V_G - V_{TH}) V_D W/L$$

where I_D is the drain current, μ_{eff} is the effective mobility, C_G is the gate capacitance, V_G is the gate voltage, V_{TH} is the threshold voltage, V_D is the source-drain bias, W is the channel width, and L is the channel length.

In the context of biochemical sensing, two principles may be used with the FET⁵²⁻⁵⁵. First, the target molecules attached on the semiconducting material are charged and can change the surface electro static potential. This is equivalent to a variance of the electrostatic gate voltage, and can typically apply to detection of charged biomolecules in solution⁵⁶. Second, the molecules bound to the material can generate doping via charge transfer, for example a strong p-dopant can inject more holes. This principle is usually applied to detection of non-charge or weak-charged molecules such as organic and gas molecules^{57,58}. In some situations, two of the processes exist and collectively influence the sensor performance⁵⁹. In both cases, the sensitivity of the sensor can be determined by the derivative of the conductivity with respect to the gate voltage or the carrier density.

$$\partial I_D / \partial V_G = C_G \mu_{eff} V_D W / L$$

$$\partial \sigma / \partial n = q \mu e$$

It is apparent that, to increase the sensitivity, we will need to increase the gate capacitance or the material carrier mobility, which explains why the high carrier mobility of graphene leads to high sensitivity of the FET sensors.

3.1.2 Review of field effect biosensors

Before emergence of graphene, 1D materials like carbon nanotube and silicon nanowire have demonstrated the power of nanomaterials in field effect sensing (Figure 3.2). For example,

people have used carbon nanotubes to detect biomarkers and gas molecules. Binding kinetics of protein receptors and its target molecules were studied on silicon nanowire based FET sensors by reaching the sensitivity lower than the limit of conventional SPR biosensors^{1,60,61}.

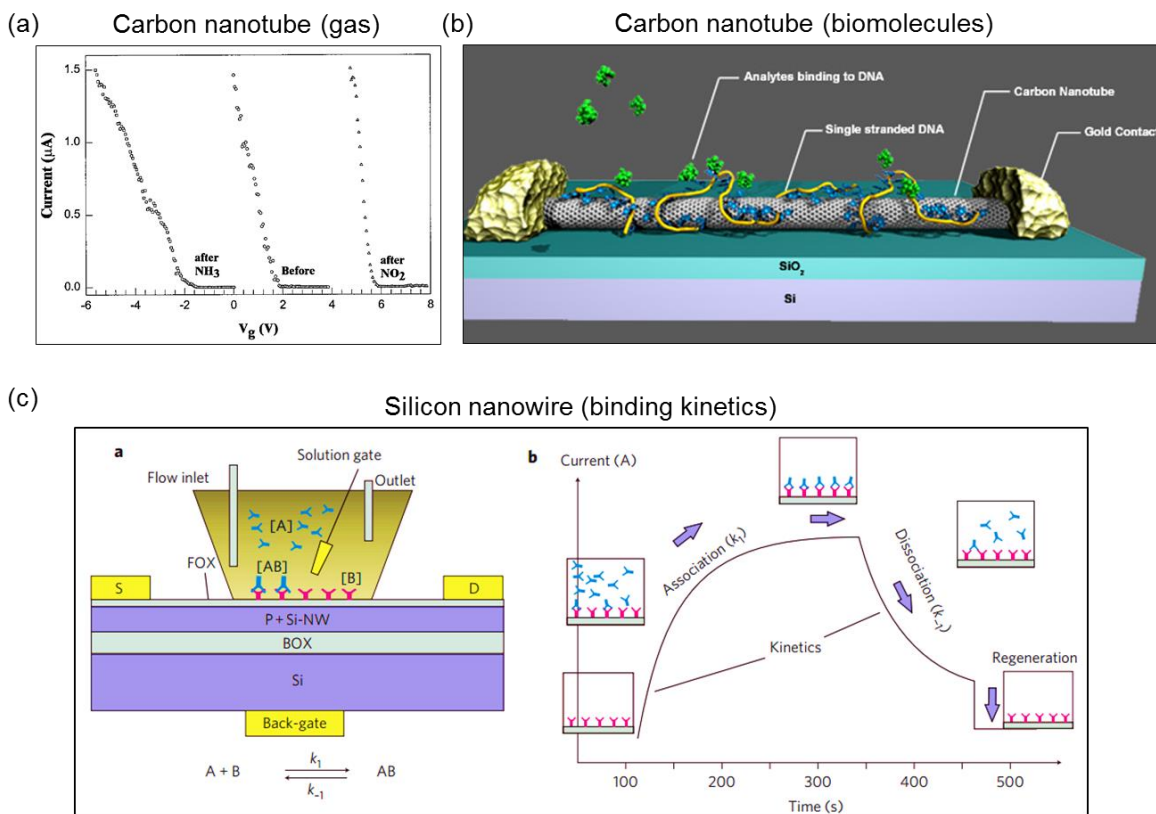


Figure 3.2: Examples of field effect biosensors based on 1D materials. (a) Silicon nanowire gas sensors. [Adapted from J. Kong *et al.* Science, 2000.] (b) Carbon nanotube sensors of detection of DNA. [Adapted from C. Staii *et al.* Nano Letters, 2005.] (c) Study of binding kinetics of molecules using silicon nanowire field effect biosensors. [Adapted from X. Duan, *et al.* Nature Nanotechnology, 2012.]

Nevertheless, scalable fabrication of 1D material-based devices have been difficult because these materials are not easily controllable, especially at high density over large area. In contrast, 2D materials like graphene, can be prepared at wafer scale with excellent continuity. Also, graphene

has higher mobility than most other materials at room temperature. These unique advantages make graphene an excellent candidate for biosensing applications. For example, individual gas molecules can be detected using graphene FET; scalable devices were already successfully prepared for detection of DNA and other biomarkers. Also, thanks to its high transparency and flexibility, graphene based wearable diagnosis and therapy equipment have also been demonstrated^{62,63}.

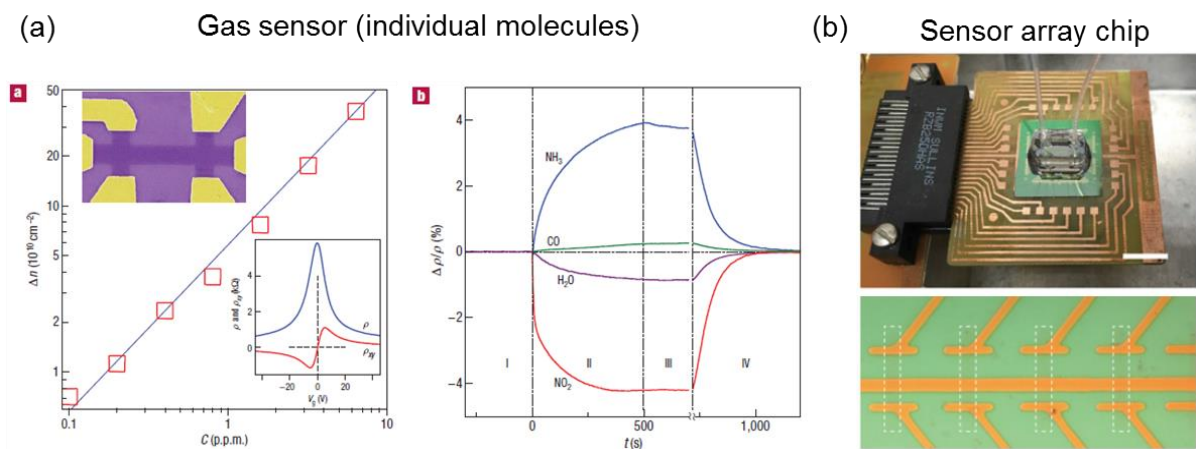


Figure 3.3: Example of graphene field effect sensors. (a) Gas sensor capable of detecting individual gas molecules. [Adapted from F. Schedin *et al.* Nature Materials, 2007.] (b) Sensor array for detection of biomolecules. [Adapted from N. Gao *et al.* PNAS, 2016.]

To date, most of the graphene FET based sensors have been used to detect highly charged molecules or strong dopant analyte, such as protein and DNA strand. The high mobility and large specific surface area of graphene should allow us to make measurements of even smaller biomarkers such as monosaccharides and low-molecular-weight proteins, which are also playing very important roles in our metabolic system.

3.2 Solution-gate graphene field effect sensors

3.2.1 Device design and fabrication

The nanosensor was configured as a solution-gated graphene FET (Figure 3.4). The graphene, serving as the conducting channel, was functionalized with receptors that can interact with target analytes. A polydimethylsiloxane (PDMS)-based open well ($\sim 20 \mu\text{L}$) was bonded to the substrate; and glucose solution was placed into the well. An Ag/AgCl reference electrode, mounted on a three-axis positioner, was inserted into the solution to serve as the gate electrode. An electrical double layer (EDL) formed at the interface of the graphene and solution served as the gate capacitor.

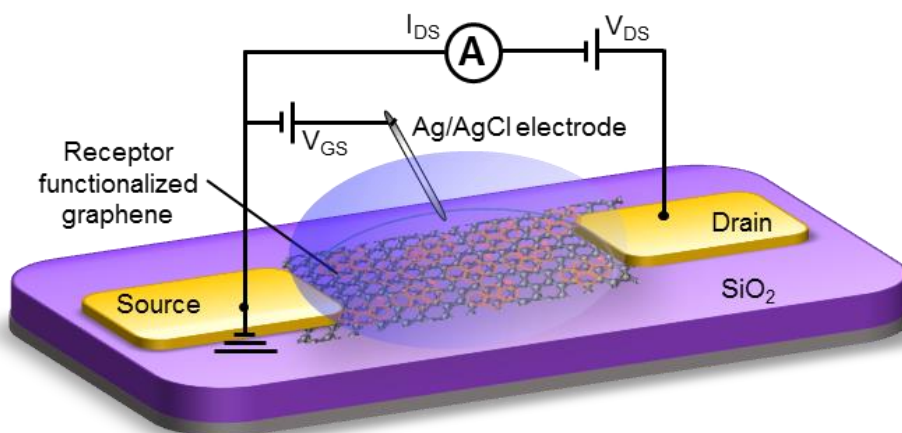


Figure 3.4: Schematic of the nanosensor configured as a solution-gated graphene field effect transistor. An Ag/AgCl electrode inserted into the solution served as the gate electrode, while the electrical double layer at the solution-graphene interface served as the gate capacitor.

The device was fabricated using micro and nanofabrication techniques on a silicon wafer with 285 nm wet thermal grown oxide. The substrate was washed using acetone, isopropanol (IPA) and deionized (DI) water sequentially and then further cleaned using reactive oxygen plasma to

remove tiny organic residue. Graphene grown on Cu foil was cut into 3 mm by 3 mm and transferred onto the substrate. Photolithography, with a bilayer resist (S1811 and LOR 3A), was used to pattern the source and drain electrodes, which were then metallized using electron beam evaporator (5/20/20 nm Cr/Pd/Au). Lift-off was completed by rinsing the chip in Remover PG and then gently washed using IPA and DI water. The graphene was then patterned into a rectangular channel (typically 20 μm by 30 μm) using photolithography and reactive oxygen etching. The chip was then again rinsed in Remover PG, IPA and DI water, gently blow dried using compressed nitrogen, and stored in vacuum before tests.

3.2.2 Affinity based glucose and insulin sensing on rigid substrate

Glucose, one of the uncharged, low-molecular-weight molecules, is of fundamental importance to people life health. Abnormal levels of glucose concentration in blood, if not properly monitored and corrected, can cause severe or even life-threatening complications to patients with diabetes or other related diseases. Graphene FET based enzymatic sensors have been reported to enable sensitive detection of glucose⁶⁴. Unfortunately, due to the irreversible, consumptive nature of the enzyme-catalyzed electrochemical reactions of glucose, as well as the undesirable byproduct (e.g., hydrogen peroxide) generated in the reactions of enzymes and glucose, these enzyme-based sensors would suffer from significant limitations in stability and accuracy when operating in physiological environments⁶⁵.

In contrast, affinity sensing, based on non-reactive equilibrium binding of analyte with an affinity receptor, neither consumes the target analyte nor produces any byproduct, therefore can potentially be implanted for stable and accurate glucose monitoring⁶⁶. Affinity glucose sensing

has been implemented using optical, mechanical, and electrical methods on conventional or microscale platforms.^{5,67-69} While demonstrating the potential of affinity glucose sensing, these methods typically require complex sensor structures (e.g., moving mechanical components or physical barriers), and may not have sufficient sensitivity in human bodily fluids such as tears or saliva, in which glucose concentrations are one or two orders of magnitude lower than that in blood⁷⁰⁻⁷³. Affinity glucose sensing using functional nanomaterials is to date rather scarce. Boron-doped graphene quantum dots have been used for affinity glucose sensing, although its requirement of an additional optical measurement system is not amenable to miniaturization⁷⁴. Boronic acid functionalized carbon nanotubes (CNTs) have also been used for glucose detection in deionized water. Nevertheless, these sensors relied on the contact among the randomly distributed, entangled nanotubes and may not be well suited to practical applications because of a lack of consistency and stability⁷⁵. Furthermore, the underlying sensing mechanisms have not been clarified due to the difficulties in precise determination of the weak doping induced by the affinity binding in the semiconducting CNTs.

This section presents an atomically thin, graphene-based sensor for affinity-based detection of glucose, an uncharged, low-molecular-weight molecule. This nanosensor employs a graphene FET in which graphene is functionalized with boronic acid for glucose recognition. In contrast to the multi-step chemical modification procedure that is required for enzyme based graphene glucose sensors, the functionalization in our sensor is enabled by a simple one-step method via the interaction of graphene with pyrene-terminated boronic acid. This method allows boronic acid to be closely attached to the graphene surface, thereby the binding of boronic acid with glucose can significantly change the electrical properties of graphene, and enables sensitive

detection of the glucose molecules. Moreover, the bipolar transfer characteristics of graphene, thanks to its vanishing bandgap and high mobility, exhibit significant and definitive shifts upon glucose-boronic acid binding. This shift can reflect affinity binding-induced charge transfer to graphene, or changes in the electrostatic potential in the immediate proximity of graphene, thereby allowing for insights into the underlying physicochemical mechanisms for affinity glucose recognition on the nanomaterial. For potential clinical applications, the coupling of graphene with boronic acid via stable chemical bonding eliminates the needs for mechanical movable structures or physical barriers that are commonly used in existing affinity glucose sensors^{5,76}. Therefore, it simplifies the device design and potentially enables a consistent, rapidly responsive measurement for noninvasive glucose monitoring. For example, wearable glucose monitoring devices can be realized by integrating these sensors with contact lens to detect the glucose concentration in tears.

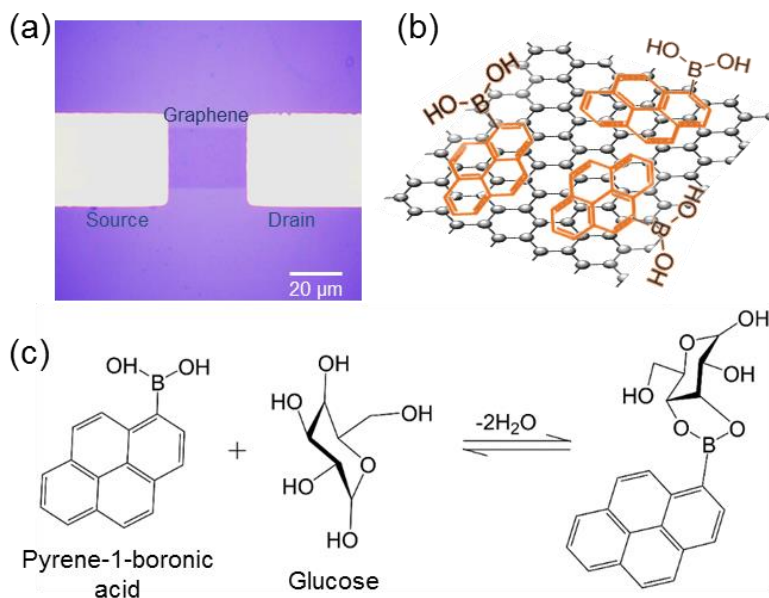


Figure 3.5: (a) Micrograph of a fabricated device. The graphene conducting channel connected the source and drain electrodes. (b) Coupling of boronic acid and graphene via π - π stacking

interactions between the pyrene group and graphene. (c) Formation of a glucose-boronate ester at a physiological pH of 7.4.

The affinity glucose nanosensor was configured as a solution-gated graphene FET (Figure 3.5). The graphene, serving as the conducting channel, was functionalized with pyrene-1-boronic acid (BAP) via π - π stacking interactions. Binding of glucose and the boronic acid formed a glucose-boronate ester complex, inducing changes in the electric conductance of the graphene, which was measured to determine the glucose concentration.

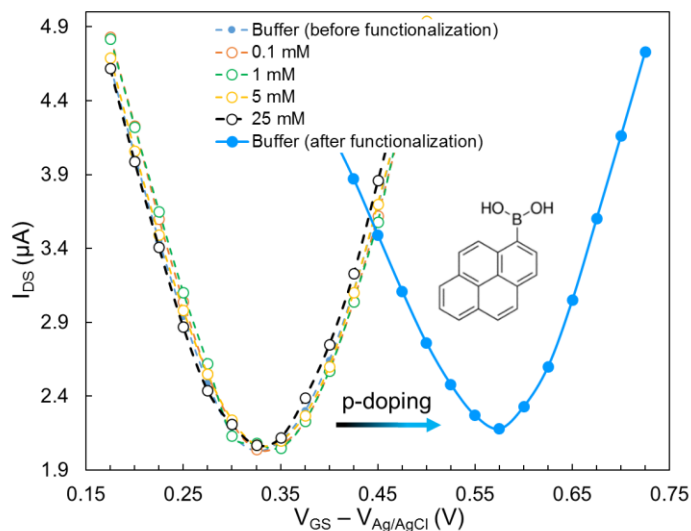


Figure 3.6: Transfer characteristics of the pristine graphene and the PBA-functionalized graphene. Dashed lines: Transfer characteristics of the pristine graphene exposed to glucose solutions (0.1 mM to 25 mM). Solid lines: Transfer characteristics after rinsing with PBA solution. VNP shifted from 0.33 V to 0.575 V. Legend: Glucose concentrations.

In a solution-gated FET, the capacitance of the double layer can be influenced by the solution composition. Prior to any chemical functionalization of the graphene, we first examined the fluctuations of the EDL capacitance that can possibly be attributed to changes in the glucose

concentration. Glucose was dissolved in phosphate buffered solution (pH 7.4) to obtain desired concentrations (2 μM to 25 mM). The same solutions were used in all of the subsequent experiments. Without any chemical functionalization of graphene, the transfer characteristics (source-drain current I_{DS} as a function of gate voltage V_{GS}) measured at the different glucose concentrations were almost indistinguishable (Figure 3.6). This suggested that glucose, at the selected concentration range, did not either interact with graphene or vary the capacitance of the double layer, in agreement with previous related studies^{75,77}.

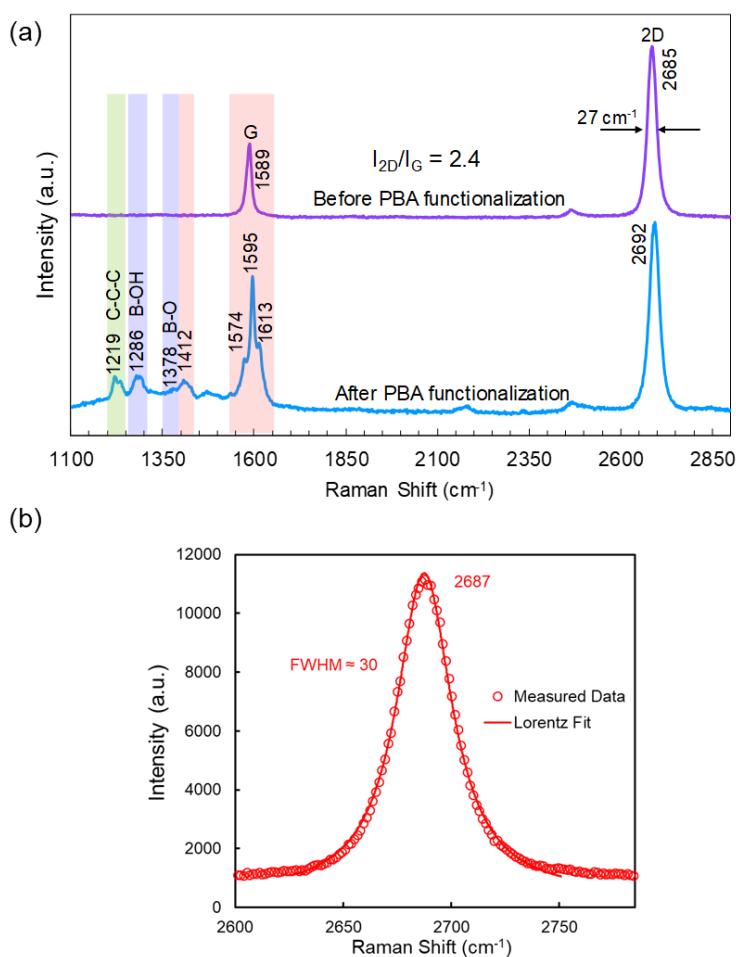


Figure 3.7: Raman spectra of the graphene before and after exposure to PBA solution. (a) Signature peaks of the boronic acid and the graphene-pyrene interaction were observed after immersing in PBA solution. (b) Fitting of the measured 2D band to the Lorentz equation.

This device was then immersed in PBA solution for 4 hours at room temperature, followed by sequentially rinsing in acetonitrile, isopropanol and deionized water to remove free PBA. In prior to the chemical functionalization, in the Raman spectrum (Figure 3.7) of the graphene at the channel region, the ratio of the intensity of the 2D band to the G band (I_{2D}/I_G) was 2.5, and the full width at half maximum (FWHM) of the 2D band was ~ 27 from Lorentz fitting, both of which were further evidence of monolayer graphene^{42,78} in addition to the color contrast observed under microscope (Figure 1b). The Raman spectrum of the PBA solution-rinsed graphene exhibited signature peaks of BOH bending (1286 cm^{-1}), B-O stretching (1378 cm^{-1}), and G-band splitting (1574, 1595, 1613 cm^{-1}) due to the graphene-pyrene π - π stacking interaction⁷⁹⁻⁸². Also, the 2D band shifted to a higher wavenumber (from 2685 to 2692 cm^{-1}), which was considered as a result of chemical doping⁸³.

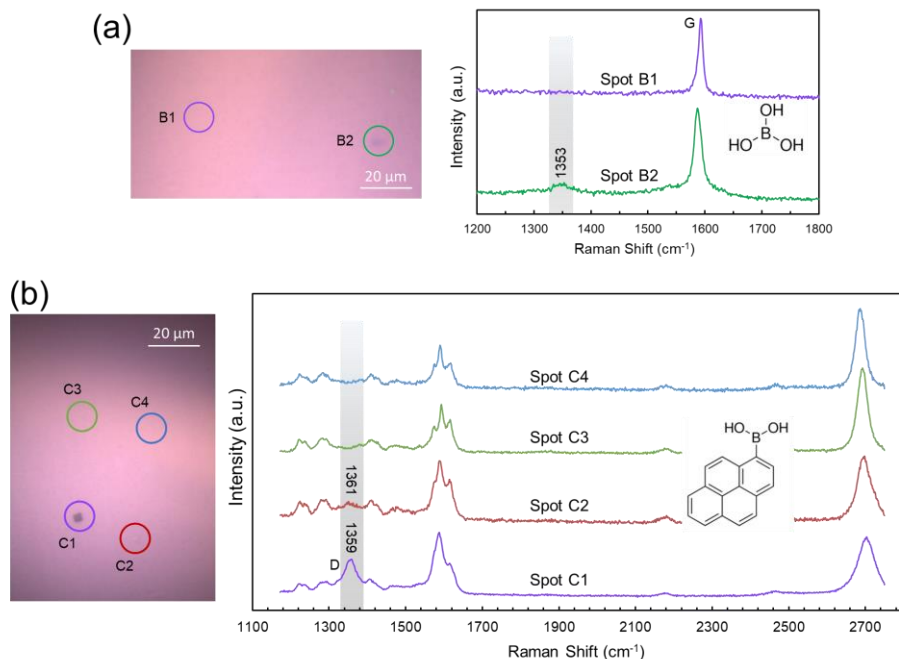


Figure 3.8: Characterization of graphene using Raman spectroscopy (a) after immersing in 1 mM boric acid solution, (b) after immersing in 1 mM PBA solution.

To confirm that these peaks come from the immobilization of BAP via the pyrene-graphene interaction, rather than reaction of boronic acid to graphene, a graphene sample was, transferred onto a SiO₂-coated substrate, was sequentially exposed to 1 mM boric acid aqueous solution, and exposure to 1 mM PBA acetonitrile solution. Raman spectra was respectively taken of the graphene sample after each of these treatment steps. The Raman spectra remained the same before and after exposure to boric acid (Figure 3.8), without displaying any peaks indicative of boric acid even at sample positions exhibiting a pronounced D-band. This implied that boric acid did not attach to graphene without other functional groups. In contrast, after exposure to PBA, the spectra exhibited peaks that are attributable to B-O stretching, BOH bending, and π - π interaction, respectively. These results confirm that, in our experiments, the boronic acid was coupled to graphene via π - π interaction of pyrene and graphene. The measured transfer characteristics (Figure 3.6) also verified the chemically induced p-type doping, represented by the increase of the neutral point voltage V_{NP} (the gate voltage at which I_{DS} attains its minimum) from 0.33 V to 0.575 V. These observed characteristics of the boronic acid as well as the graphene-pyrene interaction confirmed that the BAP molecules were successfully immobilized on the graphene.

To investigate the potential interruption of the PBA-graphene coupling by replenishment of sample solution during the nanosensor testing, we measured the transfer characteristics of PBA-functionalized graphene with fresh buffer solution added to, removed from, and then added again to nanosensor. In the two measurements when fresh buffer was added to the device, the source-drain current at each gate voltage as well as the neutral point voltage were coincident within

~1.5% (Figure 3.9), implying that the influence of the solution replenishment was negligible. It is thus believed that any significant response in the subsequent measurements would be attributable to the glucose-boronic acid binding.

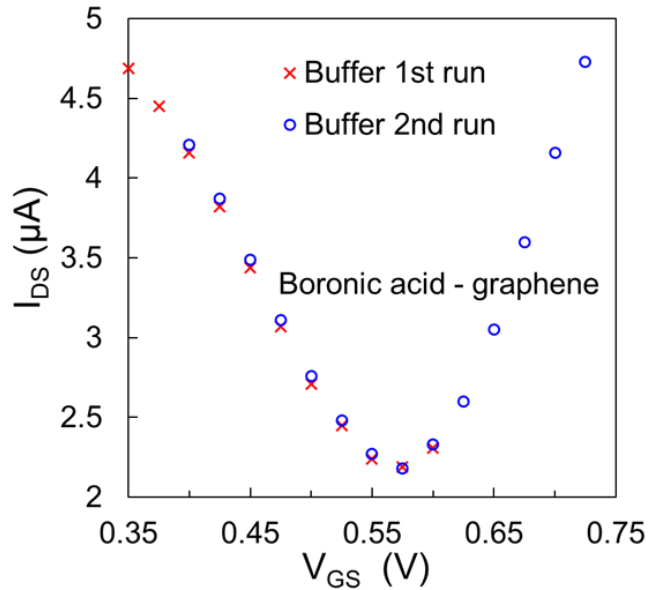


Figure 3.9: Influence of solution replenishment on transfer characteristics measurements. In the two measurements when fresh buffer was added to the device, the source-drain current at each gate voltage as well as the neutral point voltage were highly coincident.

Then the sensor was tested by exposure to glucose solution at different concentrations. The transfer characteristics curve was found to shift to the left significantly. For example, the shift was ~0.115 V as the glucose concentration increased from 0 to 25 mM (Figure 3.10). This suggests that the binding of glucose and boronic acid generated n-type doping to graphene. As the estimated transconductance (i.e., the slope of linear sections of the transfer characteristics curve) did not change significantly, the carrier mobility of the graphene was believed to be

approximately constant. Rather, changes in the carrier concentration of graphene was considered the main contributor to the observed shift of V_{NP} .

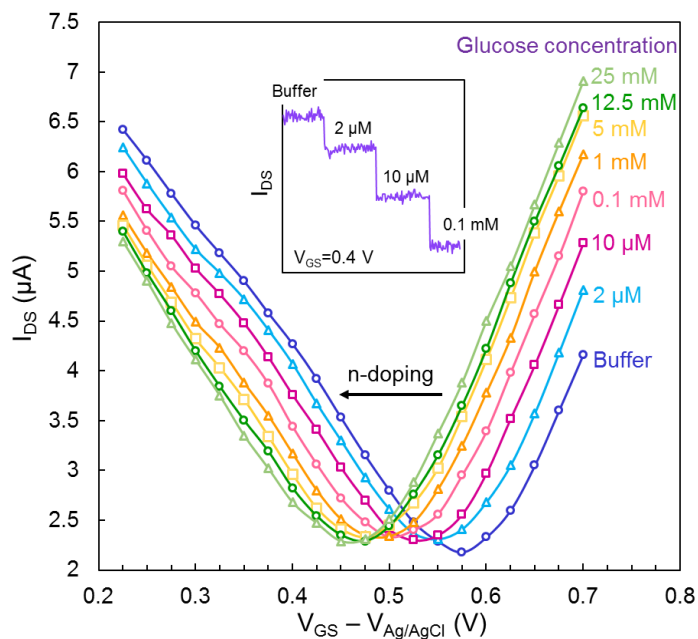


Figure 3.10: Transfer characteristics measured when the device was exposed to glucose solutions (concentration ranging from 2 μM to 25 mM). The curve shifted to the left as a result of the increase in the glucose concentration. Inset: Monotonic decrease of I_{DS} at $V_{GS} = 0.4$ V.

Measurements using butyric-acid functionalized graphene were also performed to serve as control. The measured transfer characteristics were highly coincident (Figure 3.11), suggesting that there was no significant interaction of glucose and butyric acid, and that the replenishment of the sample solution did not significantly impact the transfer characteristics measurement. We also examined variations in the source-drain current I_{DS} with the glucose concentration at a fixed gate voltage V_{GS} . It was observed that I_{DS} decreased monotonically with glucose concentration when V_{GS} was lower than the neutral point voltage V_{NP} , and this trend was reversed when $V_{GS} > V_{NP}$ (Figure 3.10), which was due to the shift of the transfer characteristics. Using this observed

dependence of I_{DS} on the glucose concentration, we estimate that, with a noise level of ~ 17 nA for I_{DS} , the resolution of the nanosensor for glucose measurements was approximately $0.46 \mu\text{M}$, appropriate for monitoring of glucose in human bodily fluids such as saliva and tears^{71,72}. We further studied the change of V_{NP} before and after PBA functionalization, denoted $\Delta V_{NP,B}$, and the further changes of V_{NP} after the graphene was exposed to glucose, denoted $\Delta V_{NP,G}$. Here, $\Delta V_{NP,B} = V_{NP,B} - V_{NP,P}$, and $\Delta V_{NP,G} = V_{NP,B} - V_{NP,G}$, where $V_{NP,P}$ and the $V_{NP,B}$ are the neutral point voltages measured in fresh buffer for pristine graphene and PBA-functionalized graphene, respectively; $V_{NP,G}$ is the neutral point voltage for PBA-functionalized graphene measured in glucose solution.

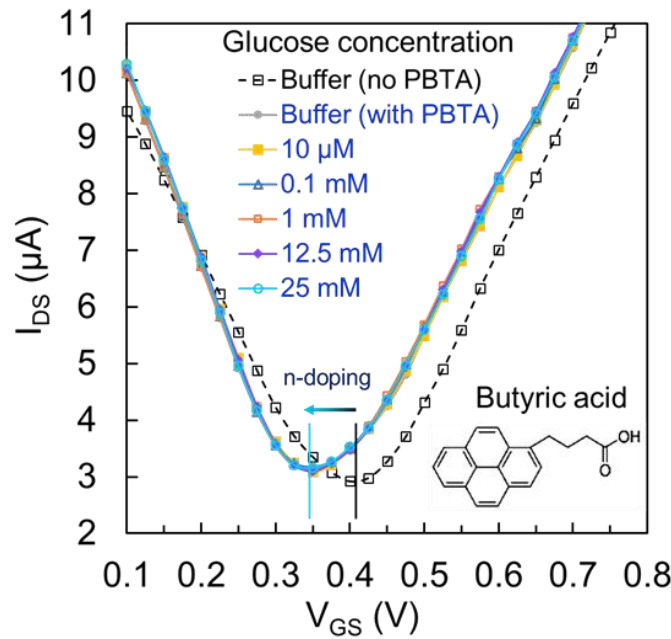


Figure 3.11 Transfer characteristics measured with glucose solutions on the butyric acid functionalized graphene. The n-type doping induced by PBTA remained unchanged when the sensor was exposed to glucose.

We observed that both $\Delta V_{NP,B}$ and $\Delta V_{NP,G}$ varied from device to device, possibly because of artifacts such as organic residue left on graphene from the fabrication process. These artifacts could have caused a device-to-device disparity in chemical functionalization of graphene, and hence in the doping level at a given glucose concentration. Interestingly, at a given concentration, the ratio $\Delta V_{NP,G}/\Delta V_{NP,B}$ did not vary significantly from device to device, with a variation of less than 6% for the three nanosensor devices tested (Figure 3.12).

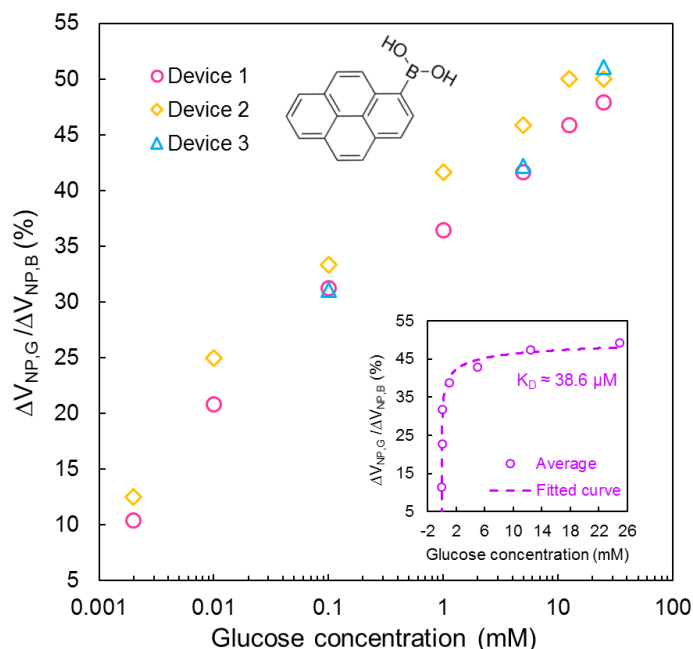


Figure 3.12: Neutral point voltage shift ratio $\Delta V_{NP,G}/\Delta V_{NP,B}$ as a function of glucose concentration. Glucose concentration is on logarithmic scale. Inset: Inset: The solid line is a fit to the Hill-Langmuir equation, yielding an equilibrium dissociation constant (K_D) of 38.6 μM . Glucose concentration is on linear scale.

To explain this observation, we note that $\Delta V_{NP,B}$ is the shift of V_{NP} caused by functionalization of boronic acid and $\Delta V_{NP,G}$ is by glucose-boronic acid binding, therefore $\Delta V_{NP,G}/\Delta V_{NP,B}$ can be regarded as a measure of the fraction of boronic acid that is occupied by glucose. Since under

conditions of constant temperature and pH as were approximately the case in our experiment, the fraction of boronic acid that binds to glucose is solely dependent on the glucose concentration. This suggests that $\Delta V_{NP,G}/\Delta V_{NP,B}$ should be a function of glucose only and independent of the device or the order in which the sample solution was added. The measured dependence of this ratio on glucose concentration followed the Hill-Langmuir equation for equilibrium ligand-receptor binding:

$$\frac{\Delta V_{NP,G}(c)}{\Delta V_{NP,B}} = A \frac{\left(\frac{c}{K_d}\right)^n}{1 + \left(\frac{c}{K_d}\right)^n} + A_0$$

where A is the sensor saturation response when all boronic acid sites are occupied, c is the glucose concentration, A_0 is an offset that accounts for the response to the fresh buffer, K_d is the dissociation constant for the glucose and boronic acid binding, and n is the Hill coefficient describing binding cooperativity. A best fitting yields a K_d of 38.6 μM , A of 0.538, A_0 of -0.0037 and n of 0.345.

While the exact mechanisms for the graphene affinity sensing remain open, some theoretical considerations can offer insight into the observed doping effects induced by chemical functionalization and glucose-boronic acid binding. First, to explain the observed p-type doping due to the attachment of PBA, we note that while pyrene group is electron-rich and not expected to induce p-doping, boronic acid is electron deficient and its electron-withdrawing nature could induce p-doping in the graphene. This is supported by our experiments in which immobilization of electron-rich groups on graphene (such as butyric acid, a carboxylic acid) resulted in n-type doping in the graphene (Figures 3.11), and also in agreement with experimental observations

reported by others^{82,84}. Second, the observed n-type doping due to the boronic acid-glucose binding was likely the result of an increase in the local electrostatic potential in the proximity of graphene, as suggested by results from a potentiometric study of glucose detection by boronic acid^{85,86}, which resembles our graphene nanosensor in electrode configuration. This electrostatic potential increase could be attributed to the formation of boronate, which would increase the electron donating ability of boronic acid while weakening its electron-withdrawing ability⁸⁶.

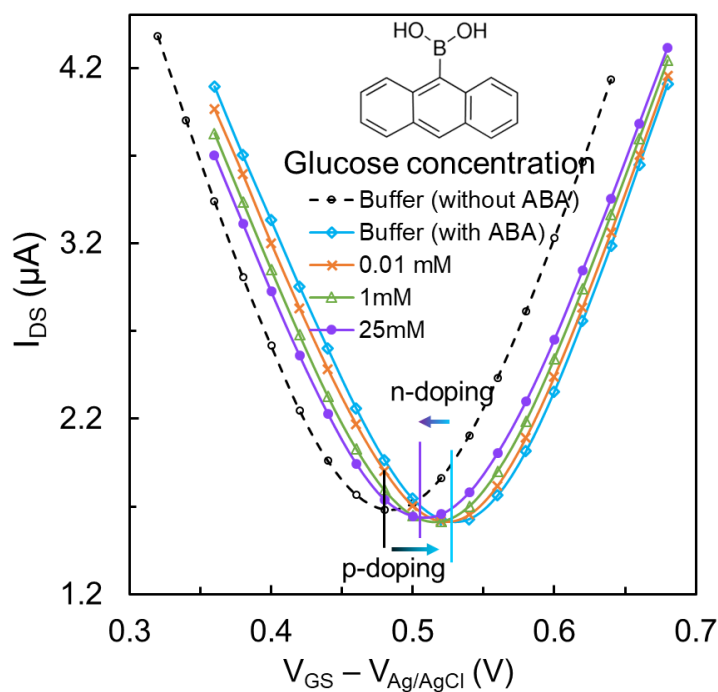


Figure 3.13: Measurements of fructose using 9-anthracene-boronic acid (ABA) as receptor. The p-doping induced by boronic acid, and the n-doping upon glucose binding were qualitatively consistent with the observations in glucose measurements using PBA.

These conjectured sensing mechanisms suggest that immobilization of boronic acid on graphene or even other semiconducting materials, using other attachment groups should also allow for glucose recognition. Indeed, measurements of glucose using graphene that was modified with 9-

anthracene-boronic acid (Figure 3.13) were found to be qualitatively consistent with results obtained with PBA as presented above. The corroboration of these mechanisms, however, requires a systematic study in future work. Further insight into the underlying physics may also lead to important improvements in the sensor performance. In particular, affinity sensors that use boronic acid (which forms boronate by binding to diol groups), including our current nanosensor (Figure 3.14), is in general not capable of distinguishing between different diol-containing monosaccharides. Although they may still be adequate for practical glucose detection in physiological fluids where glucose is present at dominant concentrations^{87,88}, we anticipate that it is possible to chemically modify boronic acid-based receptors to impart glucose-specificity to the nanosensor over other monosaccharides⁸⁹, which will also be a major subject of our future investigation.

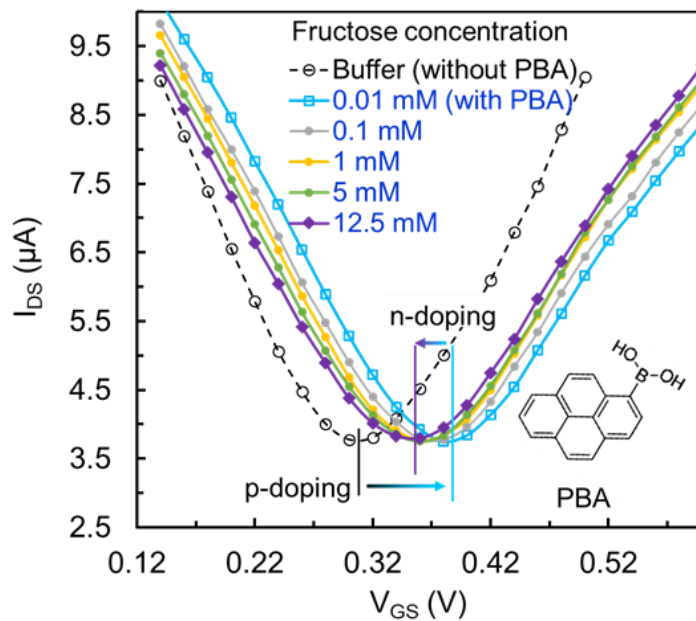


Figure 3.14: Measurements of fructose using PBA as receptor. The p-doping induced by boronic acid, and the n-doping upon glucose binding were comparable to the observations in glucose measurements.

3.2.3 Real-time monitoring of insulin level

Control of glucose level in blood is critical for patients suffering from both Type 1 and 2 Diabetes⁹⁰. Most of the therapy options eventually require administration of insulin, an endocrine peptide hormone promoting absorption of blood sugar. While insulin can be injected or inhaled by patients, it remains a challenge to choose a correct dose schedule, as the effective durations and strengths of different types of insulins vary significantly^{91,92}. Blood sugar levels are usually measured to assist to determine the dose of insulin injection, which unfortunately lacks accuracy because of the lag from insulin introduction to effective glucose regulation⁹³. Therefore, use of insulin in a timely manner is strongly dependent on accurate predictions of insulin levels.

Conventional antigen-antibody based methods to quantify insulin concentrations, such as the radioimmunoassay (RIA) and enzyme-linked immunosorbent assay (ELISA), are time-consuming and not amenable to real-time monitoring⁹⁴. Electrochemical or optical sensors have been developed to largely reduce the required detection time (< 2 hours)^{93,95-98}. However, due to the low molecular mass (5807.57 g/mol) and weak charges of insulin, the sensitivities (1.34 nM) obtained using these methods have not allowed us to perform label-free detection of insulin at physiologically relevant levels (lower than 270 pM)⁹² without pretreatment of samples.

This section presents a graphene field effect-transistor (GFET) based aptameric nanosensor for the real-time monitoring of insulin levels, relying on the affinity binding of insulin and its aptameric receptor IGA3. The short time required for monolayer aptamer-insulin binding and the rapid response of graphene to external disturbances enable the nanosensor to respond to changes

in the insulin level within 260 s. Furthermore, physiologically relevant levels of insulin, as low as 35 pM, can be detected. This is attributable to the high sensitivity of the GFET to the changes in the charge distribution on and in the immediate vicinity of the graphene surface, which is offered by the high mobility and large surface-volume ratio of graphene. Moreover, as aptamers can discriminate between insulin and other closely related analogs on the basis of subtle structural differences, the aptameric nanosensor showed significant improvements in the specificity to insulin over the devices based on antigen-antibody reactions. Here, we have experimentally demonstrated that the aptameric nanosensor could be used for label-free, specific and real-time measurement of insulin at physiologically relevant levels. The nanosensor is configured as a graphene based field effect transistor. The electrical double layer at the interface of the graphene and electrolytes serves as a gate dielectric. A drain-source bias V_{ds} generates a current I_{ds} through the graphene channel, as a function of the applied gate voltage V_g .

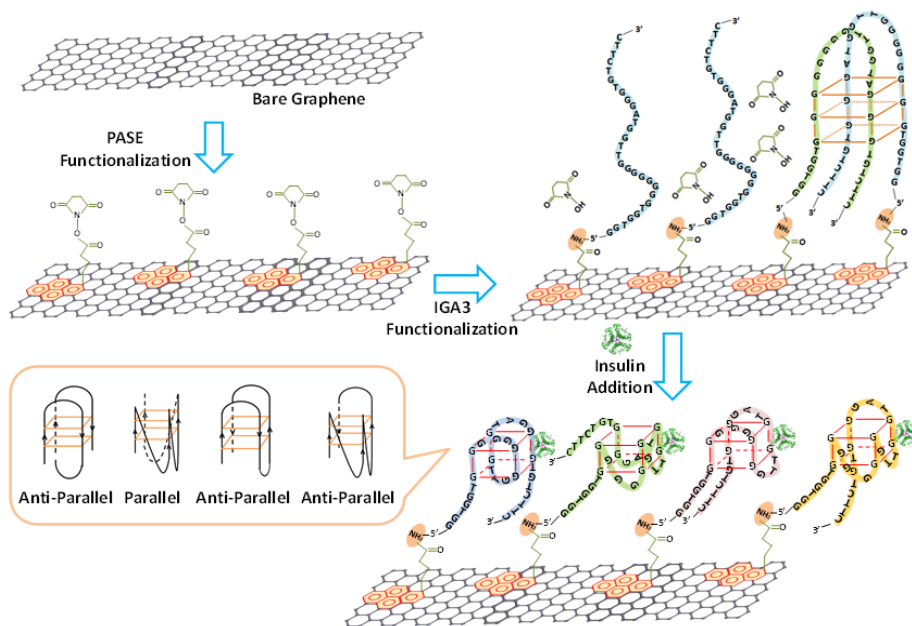


Figure 3.15: Principle of the graphene nanosensor for insulin detection. The sensing surface is prepared through Schiff-base reaction between aptamer IGA3 and the graphene immobilized

PASE linker. The aptamer specifically binds to insulin in the sample solution, promoting the formation of both parallel and anti-parallel G-quadruplex, which brings negatively charged insulin and DNA strands to the close vicinity of graphene surface, causing disturbances to the carrier concentration in the bulk of graphene and yielding detectable signals.

Detection of insulin was allowed by the structural change of the insulin-specific aptamer (IGA3) when interacting with insulin (Figure 3.15). IGA3 is a guanine-rich oligonucleotide strand, in which G-quartet planes can form via Hoogsteen base-pairing, consisted of four hydrogen-bonded guanine bases. G-quadruplex can then be generated by stacking of two or more G-quartet structures. These structural changes of the aptamer in the close vicinity of graphene cause disturbances to the charge carriers in graphene and result in detectable changes in the measured I_{ds} . To biochemically activate graphene surface for insulin binding, the graphene channel was functionalized as follows. 1-pyrenebutanoic acid succinimidyl ester (PASE) was noncovalently coupled to graphene *via* π - π interaction, after which the IGA3 aptamer was immobilized on the surface *via* the reaction of amine group on the aptamer with the NHS ester on PASE. Further details of the device fabrication and surface functionalization can be found in Supplementary Information.

The nanosensor was then used to measure insulin levels in phosphate buffered saline (PBS). Insulin solutions of increasing concentrations from 100 pM to 1 μ M were sequentially introduced to the PDMS chamber of the nanosensor. The binding of insulin to the IGA3 aptamer was allowed to reach equilibrium before the replenishment of sample solutions. After exposure to insulin, the measured V_{NP} decreased significantly, at a rate of ~ 0.075 mV/pM within

physiologically relevant insulin levels (Figure 3.16), indicating that binding of insulin to the IGA3 aptamer generated n-type doping to graphene.

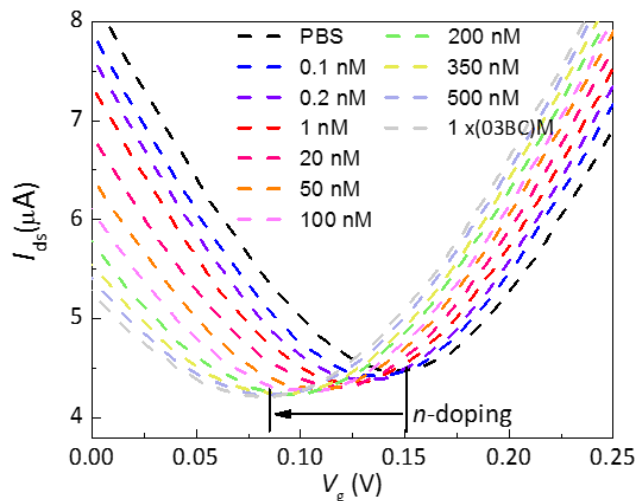


Figure 3.16 Detection of insulin using the aptameric nanosensor. (a) Transfer characteristics measured when the aptamer-functionalized graphene was exposed to insulin solutions (concentration: 100 pM to 1 μ M). The transfer characteristic curve shifted to the left as a result of the increase of the insulin concentration.

It was observed that the transconductance of both hole and electron conduction branches remained constant, at $40.476 \pm 0.686 \mu\text{S}$. Given that the ionic strength of the buffer did not change, the double layer capacitance was also deemed unchanged. Therefore, the carrier mobility was not expected to be varied significantly by insulin binding. Instead, the left-shift of the V_{NP} clearly suggested that more electrons (n-type carrier) were doped into graphene upon the interaction of insulin to the IGA3 aptamer. Typically, the detection of large biomarkers, such as proteins, using a solution-gated graphene FET is based on the electrostatic gating effect generated by the highly charged biomarkers on graphene. Under these circumstances, the charges

induced in graphene were opposite to and hence in balance with the charges carried by the target molecules. In our experiments, while the insulin, whose isoelectric point (PI) is 5.8, was weakly and negatively charged at pH of 7.4, n-type doping was generated in graphene upon the binding of insulin to the IGA3 aptamer. Thus, the increase in the electron (n-type carrier) concentration in the graphene was not considered as a result of the electrostatic gating effect but could be attributed to the direct charge transfer to the graphene, from either insulin or the deformed IGA3 aptamer.

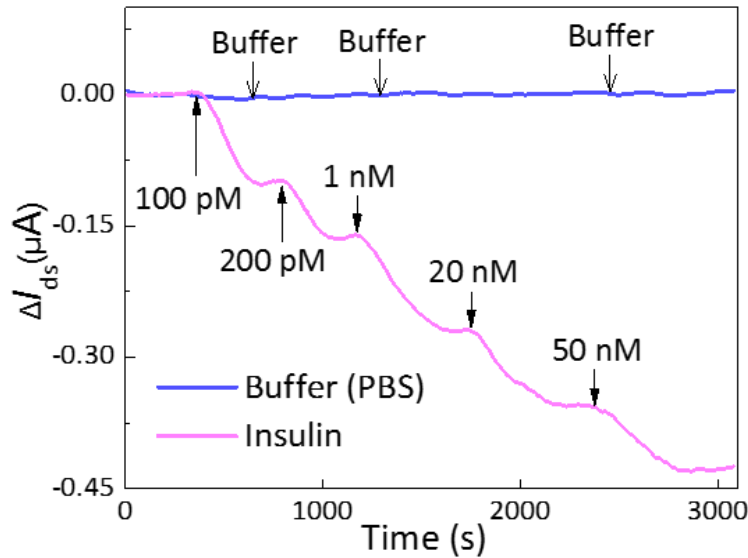


Figure 3.17: Real-time measurement of insulin concentration changes. The responses are demonstrated by the changes of the drain-source current I_{ds} .

Time-resolved measurements (Figure 3.17) of insulin were performed on the nanosensor with fixed drain- source bias $V_{ds} = 50$ mV and gate bias $V_g = -50$ mV. With increase in insulin concentrations from 100 pM to 1 μM , the measured I_{ds} monotonically decreased from 8.09 to 7.16 μA . The binding of insulin with the monolayer IGA3 aptamer reached equilibrium within 260 s (Figure), appropriate for real-time monitoring of insulin levels. With a noise level of 8.66

nA, the limit of detection (LOD) was estimated to be 35 pM, outperforming most of the existing methods^{99,100}.

3.2.4 Tumor necrosis factor alpha sensing on flexible substrate

In this section, we introduce a flexible graphene aptameric nanosensor fabricated on polyethylene naphthalate (PEN) film, which can work properly under bending, for rapid, direct, highly sensitive and label-free detection of tumor necrosis factor α (TNF- α) at physiologically relevant levels. TNF- α is a pro-inflammatory factor that acts as a biomarker of many kinds of pathologies. Hence, to develop wearable biosensors to monitor the TNF- α level is of great significance for clinical diagnostics. Currently, existing methods to quantify the TNF- α concentration, such as surface plasmon resonance and fluorescence measurement, are still hampered by sensitivity and not amenable to be used in wearable applications. Graphene has demonstrated excellent potential for flexible electronics and wearable devices. The mechanical flexibility of the PEN film also accommodates the deformation of the substrate and allows the nanosensor to conform to nonplanar surfaces that can potentially be useful in applications with geometries with curvature. In addition, thanks to the short time required for the binding between the monolayer aptamer and TNF- α , the graphene nanosensor can be used for rapid detection of TNF- α with enhanced sensitivity.

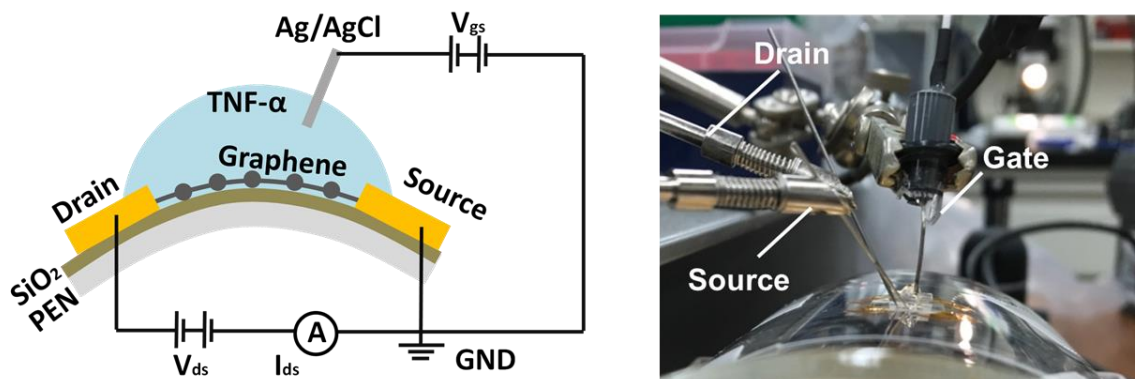


Figure 3.18: Device design and measurement setup of the flexible graphene FET sensor.

The flexible nanosensor is configured as an electrolyte-gated graphene field-effect transistor (Fig. 3.18). A 50 nm thick SiO₂ layer is first coated on the PEN substrate. Drain and source electrodes are fabricated using standard microfabrication technologies, and graphene is subsequently transferred onto the substrate.

PASE is coupled to graphene via π - π stacking. Then aptamer VR11 is conjugated to PASE by forming amide bonds. Captured TNF- α by the aptamer varies the carrier concentration in graphene, yielding a detectable signal. We then tested the aptamer-functionalized nanosensor with TNF- α under different bending radii. As the TNF- α concentration increased from 0 to 500 nM, the V_{Dirac} of graphene at different bending radii (flat and 40.3 mm) were found to decrease by 35 mV and 12 mV, respectively (Figure 3.19). This indicated that TNF- α captured by the aptamer altering the surface charge distribution and changing the carrier concentration of graphene.

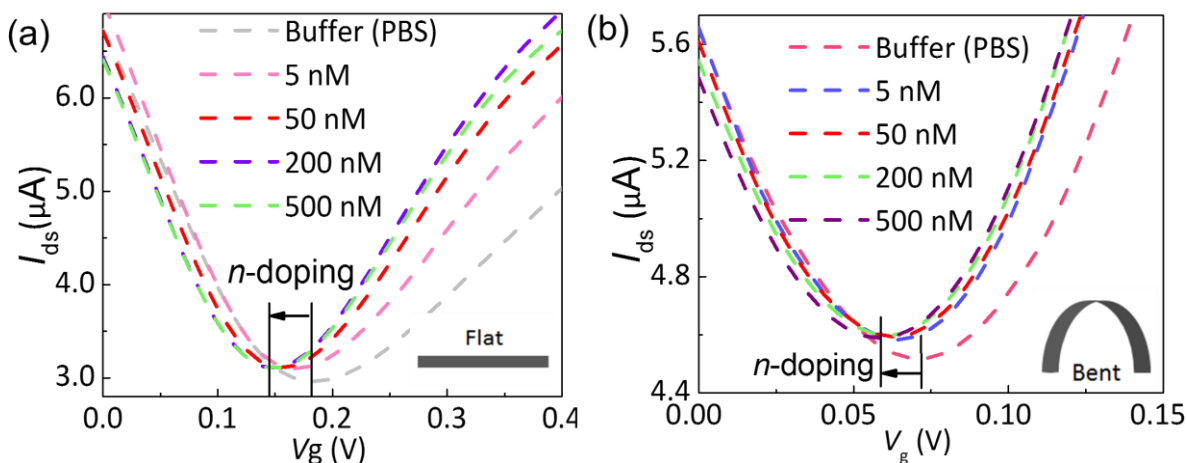


Figure 3.19: Transfer characteristics measured when the aptamer-functionalized graphene, in flat (a) and bent (b) status, exposed to TNF- α solutions (concentration: 5 nM to 500 nM). The transfer characteristic curve shifted to the left as a result of the increase of the TNF- α concentration.

3.3 Bottom local-gate graphene field effect sensors

As described in the previous sections, graphene has been used to form a conducting channel in field effect transistors (FET), allowing highly sensitive electric detection of analytes. Such graphene FET (GFET) sensors, when operating in liquid media, are generally constructed in a solution-gated or solid-gated configuration. In a solution-gated GFET sensor, a reference electrode is inserted into the electrolyte solution that is in contact with graphene to serve as the gate electrode, while the electric double layer (EDL) formed at the solution-graphene interface plays the role of the gate dielectric. Using various compositions of an electrolyte solution or graphene-immobilized functional groups, such sensors have been used to demonstrate the detection of physicochemical parameters such as glucose and insulin.

These solution-gated sensors typically require an external electrode inserted into the electrolyte solution, which hinders the integration and miniaturization of the device. In addition, the gate capacitance, or the capacitance across the EDL dielectric layer is susceptible to disturbances in liquid media, which can result in fluctuations in electrical measurements of properties of graphene including the position of the Dirac point. In contrast, in a typical back-gate GFET, the gate capacitance is provided by a SiO₂ dielectric layer sandwiched between graphene and the underlying silicon substrate, which serves as the gate electrode. By eliminating the need for the external wire insertion into the electrolyte solution, solid-gated sensors can be highly miniaturized and integrated. However, due to the intrinsically low capacitance of the SiO₂ layer, usually the solid-gated GFET sensors require undesirably high gate voltages (40~50 V), consequently impeding their application to biosensing in liquid media. This section presents a GFET nanosensor in liquid media using a thin layer of HfO₂ with a high dielectric constant (κ) as a gate dielectric layer. This sensor is operational at a gate voltage of less than 1.5 V, which is approximately a factor of 30 lower than that used in conventional SiO₂ solid-gated sensors.

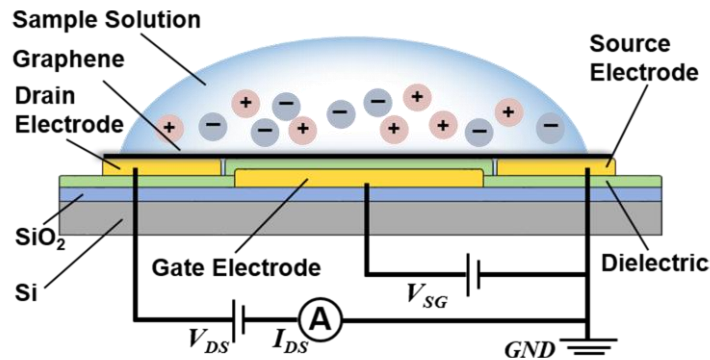


Figure 3.20: Schematic of the graphene-based FET nanosensor. Graphene serves as the conducting channel, while a 20-nm-thick HfO₂ layer between the graphene and the substrate-supported gate electrode serves as the dielectric layer.

3.3.1 Sensor design and fabrication

The HfO_2 layer is sandwiched between the conducting-channel graphene and a gate electrode (Figure 3.20) and is hence embedded within the sensor. This enables a high level of integration in the construction and passivation of electrically conducting elements in the sensor, as is highly desirable for analyte detection in liquid media. The use of the high- κ dielectric material (HfO_2) provides two orders of magnitude higher specific capacitance than conventional SiO_2 solid-gated sensors, thereby rendering high transconductance and allowing the device to operate at low gate voltages. In addition, the gate dielectric is isolated from the liquid media, thus eliminating errors caused by disturbances (e.g., bulk motion of sample solution).

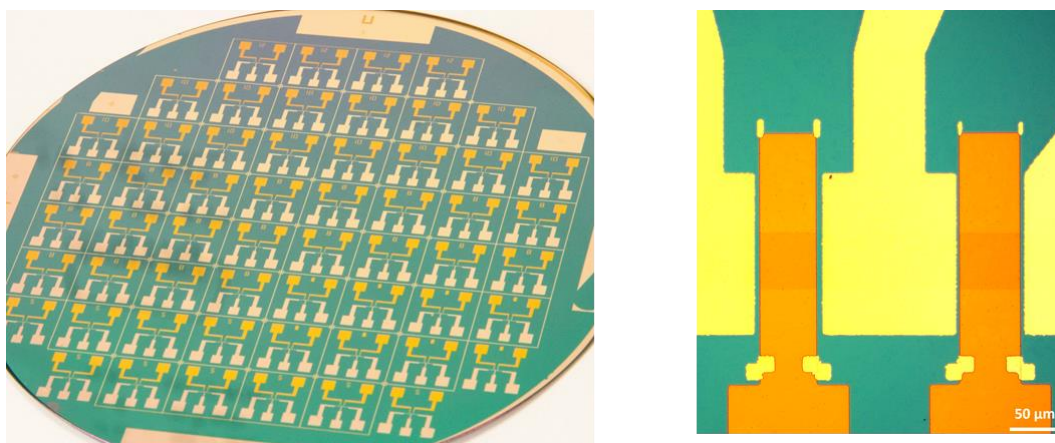


Figure 3.21: Fabricated sensors. Left: Photograph of a 4-inch wafer on which the devices were fabricated. Right: Microscopic photo of close-up of the channel region.

The nanosensor (Figure 3.21) was fabricated on a SiO_2 -coated silicon substrate. After cleaning of the SiO_2 , 5/45 nm Cr/Au was deposited. Photoresist (S1811, Shipley) was then spin-coated on top of Au at 5000 rpm for 1 min, and baked at 115°C for 1 min. Photolithography (MA6, Suss

MicroTec) was then used to pattern the shape of the gate electrode on the wafer. The wafer was then developed in developer (AZ MIF 300, AZ Electronic Materials) and local wet etched in gold and chrome etchant subsequently. The wafer was cleaned with piranha solution followed by oxygen plasma. Next, a 20 nm HfO₂ layer was deposited on top of the gate electrode using atomic layer deposition (ALD, Savannah 200, Cambridge Nano Tech) at 3.6×10^{-1} torr and the temperature as high as 200°. Another layer of photoresist (S1811, Shipley) was spin-coated and patterned to define the shape of source and drain electrodes, followed by deposition of 5/45 nm Cr/Au. Lastly, the wafer was immersed in photoresist stripper (AZ MIF 400 Stripper) and acetone sequentially to dissolve the photoresist and shape the drain and source electrodes.

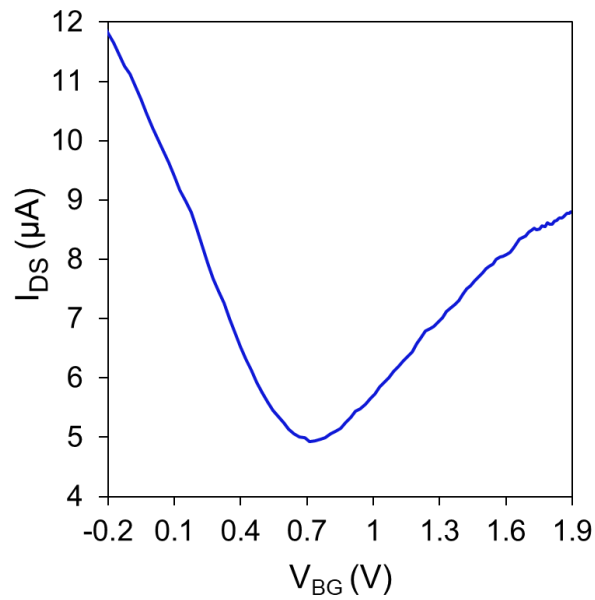


Figure 3.22: Transfer characteristic of the bottom local-gate graphene FET in air.

We then investigated the transfer characteristics of bare graphene in air. I_{DS} was measured while the solid-gate voltage V_{SG}, which makes a major contribution to the overall gate voltage (below), was varied from -0.2 to 1.9 V. An ambipolar curve was observed; the Dirac point solid-gate

voltage, or the gate voltage value at which the I_{DS} achieves the minimum (Figure 3.22), was hence determined to be $V_{SG,NP} = 0.7$ V. This confirmed the functionality of the bottom local-gate FET devices.

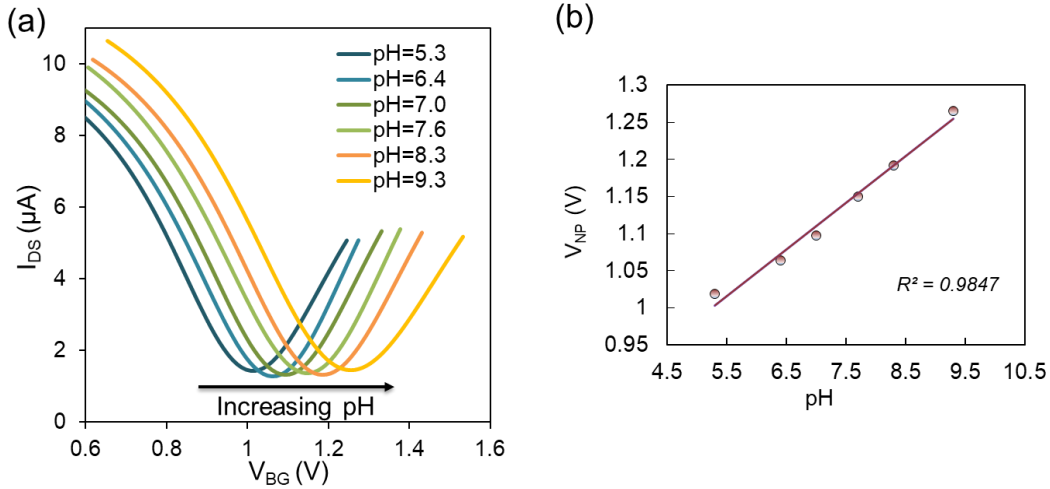


Figure 3.23: Dependence of the nanosensor characteristics on pH. (a) Transfer characteristic curves obtained at varying pH values. The $V_{SG, DP}$ shifts linearly to higher gate voltages with increasing pH (57.6 mV/pH). (b) Dependence of the Dirac point voltage on pH. The solid line represents a linear fit.

3.3.2 Real-time monitoring of solution pH level

We next tested our nanosensor for pH sensing in liquid media. Samples at various pH values (5.3 to 9.3) were prepared by mixing NaOH or HCl with phosphate buffered saline (PBS) buffer (Life Technologies, ionic strength ~ 150 mM). A sample solution was incubated with our nanosensor, during which I_{DS} values were measured while the gate voltage V_{BG} was swept from 0.6 V to 1.6 V. We found that $V_{SG,NP} < 1.5$ V at all pH levels (Figure 3.23). These significantly reduced gate voltage values, compared to 40-50 V for SiO_2 based solid-gated sensor, can be attributed to the high gate capacitance and hence the high transconductance provided by the high- κ HfO_2

dielectric layer. $V_{SG,NP}$ was found to linearly increase with the pH value at a sensitivity of ~ 57.6 mV/pH, which would otherwise not be attainable by a conventional dielectric (SiO_2)-based device operating at similarly low gate voltages. We have also determined that these measurements were reproducible, with a different device of the same design yielding a closely agreeing sensitivity of 58.2 mV/pH. When pH increases, the electrostatic potential above graphene increases due to the decrease of H^+ (see below); therefore, the curve shifts to the right to compensate for the increase in the electrostatic potential. The leakage current between drain/source and gate electrodes was found to be much smaller than I_{DS} and therefore negligible.

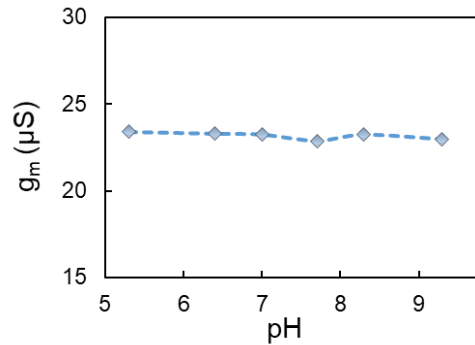


Figure 3.24: Independence of transconductance of the pH levels.

There are two possible physical processes that have been used to explain how adsorption of ions on graphene causes variations in the conductivity¹⁰¹. The first process involves the charging of the EDL capacitor by adsorbed ions, thereby causing variations in the potential in the solution in contact with the graphene, and therefore changing the Fermi level and carrier density of graphene, e.g., the electric field tuning¹⁰². In the second process, which is known as the surface charge transfer doping¹⁰¹, adsorbed ions serve as dopants, from which electrons are exchanged into the graphene. Our solid-gated sensor, which avoids the influence of the externally applied top gate voltage on the EDL, can be used to investigate the effect of either the EDL capacitor

charging or the surface charge transfer doping. Derived from the transfer characteristics obtained at different pH levels, the transconductance was found to be within 0.3 μS of a constant value of 23.2 μS (Figure 3.24), implying that the carrier mobility was also approximately a constant regardless of the pH variations. Therefore, the surface transfer doping is not a dominant effect, which would otherwise have altered the carrier mobility significantly¹⁰³, in agreement with the study by Xia¹⁰⁴ and Mailly¹⁰⁵.

On the other hand, to investigate the effect of the charging of the EDL capacitor our sensor can be modeled as a dual-gate field effect transistor consisting of the solid gate (with HfO_2 as the dielectric) below the graphene and a solution gate formed by the EDL above the graphene at its interface with the solution. The voltage on the top solution gate, V_{LG} , which is equal to the potential drop across the EDL capacitor, depends on the ion concentration in the electrolyte solution. This solution gate voltage, which leads to the charging of the EDL capacitor, can be estimated by the Nernst equation¹⁰⁶, $V_{LG} = E_0 - 2.3 \log(\text{H}^+)RT/nF$, where E_0 is a constant reference potential, R the universal gas constant, T the temperature of 298.15 K, n the ionic charge (1 for H^+), F the Faraday constant. With $\text{pH} = -\log(\text{H}^+)$, we obtain $V_{LG} = E_0 + (59.2 \text{ mV}) \text{pH}$. Thus, the highly linear dependence of the experimentally determined $V_{SG,DP}$ on pH (Figure 3.23) allowed us to conclude that the right shift of $V_{SG,DP}$ with pH is due to the increase in V_{LG} . In addition, it was seen that $V_{SG,DP}$ depended on V_{LG} in a roughly linear manner in the pH range tested. As the slope of this dependence (estimated to be ~ 1) is equal to the ratio of the solution-gate capacitance (C_{LG}) to the solid-gate capacitance (C_{SG})^{107,108}, $C_{LG}/C_{SG} \approx 1$. That is, the solid-gate capacitance was comparable to the liquid-gate capacitance¹⁰⁹ (typically on the order of 1 $\mu\text{F}/\text{cm}^2$) in our nanosensor, representing a significance improvement over SiO_2 solid-gated

GFET devices. This should be attributable to the coupling between the C_{LG} and C_{SG} in parallel (Figure 3.25).

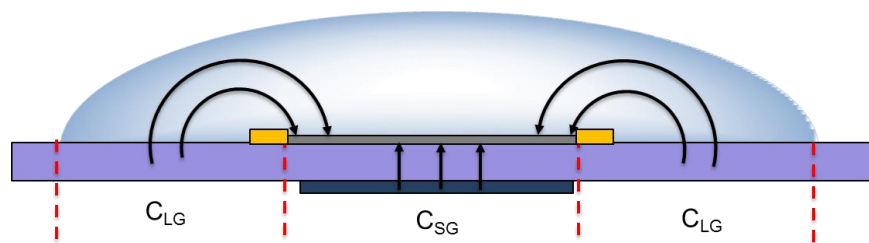


Figure 3.25: Schematics of the coupling effect between the C_{LG} and C_{SG}

Note that the area of the graphene gated by the electrode is significantly smaller than the area covered by the droplet of the electrolyte, the equivalent capacitance C_e would be dominated by the liquid gate capacitance. This means that, without exposing the metal electrode to the solution, the gate capacitance remains close to the very high double layer capacitance, which is difficult to achieve using solid dielectric materials. This allowed the nanosensor to operate at the low gate voltages as demonstrated. In addition, it should be noted that at a given pH level, a significant increase in the ionic strength of alkali cations (e.g. Na^+ , K^+) may decrease the measurement sensitivity. This is because the electrostatic gating effects produced by the alkali cations compete with the gating effects from the H^+ . Therefore, to measure the concentration of H^+ , the concentration of the nonspecific ions should be maintained at a constant level to obtain a constant sensitivity. Indeed, the concentrations of the alkali cations were approximately constant in our experiments, as the NaOH was added to the buffer at a very dilute concentration (~ 0.1 mM) and hence had negligibly effects on the on the ionic strength of the buffer (150 mM). Therefore, the sensitivity in pH measurements was approximately constant and not affected by the addition of NaOH for control of pH values.

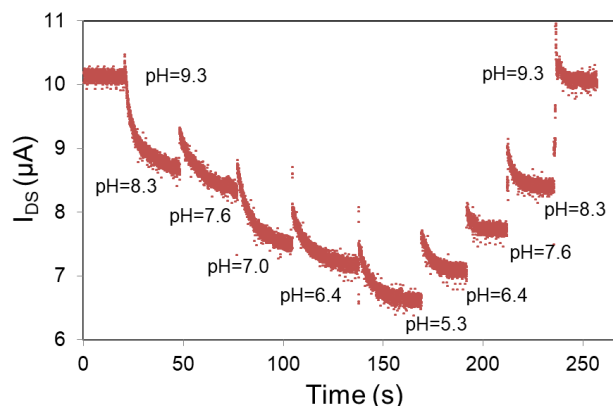


Figure 3.26: Real time measurements of pH: the source-drain current I_{DS} varied consistently and reversibly with pH at a fixed gate voltage ($V_{SG} = 0.75$ V).

To demonstrate the ability of the nanosensor to perform real-time pH measurements, we measured I_{DS} at a fixed gate voltage ($V_{BG} = 0.75$ V), while successively introducing samples with different pH values (Figure 3.26). As pH decreased from 9.3 to 5.3 (i.e., the solution becomes more acidic), the V_{TG} also decreased, and the EDL capacitor accordingly underwent partial discharging. This caused a decrease in the carrier concentration of the graphene, and I_{DS} hence correspondingly decreased. These phenomena were reversed as pH continued to change, but now in a reversed direction by increasing from 5.3 to 9.3. This reflected that the EDL capacitor underwent charging, thereby causing the carrier concentration in the graphene, and hence I_{DS} , to increase. Throughout the entire set of measurements, the values of I_{DS} were found to be consistent at a given pH value, regardless of whether this value was reached by pH increasing from a lower value or decreasing from a higher value, with small deviations attributable to the hysteresis in the electronic transport in the graphene¹¹⁰. Thus, it was concluded that pH measurements by the nanosensor were reversible, which is important for practical applications. The compact and integrable sensor design could potentially enable detection of other biomarkers.

3.4 Chapter summary

In this chapter, we introduced our works on the graphene based field effect biosensing, with focus on addressing the difficulties in detection of low-molecular-weight small molecules. First, the solution-gate FET sensor was presented for affinity-based detection of low-charge, low-molecular-weight molecules, using glucose as a representative analyte. The nanosensor employed a graphene field-effect transistor in which graphene was functionalized with boronic acid for glucose recognition. The boronic acid is attached to graphene via the interaction between graphene and pyrene groups, allowing sensitive detection of electrically neutral glucose molecules. Testing results demonstrated that the nanosensor was capable of measuring glucose in a practically relevant range of 2 μM to 25 mM, with a resolution of 0.46 μM . Second, we presented real-time monitoring of insulin using the GFET sensors. Experimental results indicated that the graphene nanosensor used by this approach demonstrated a distinctive ability in quantitatively monitoring of insulin levels ranging from 100 pM to 1 μM with a limit of detection (LOD) down to 35 pM. Third, the GFET sensors were fabricated on flexible substrates for detection of dry-eye disease related biomarker TNF- α .

In addition to the solution-gate GFET sensors, we also proposed a bottom local-gate FET sensor. The embedded solid gate eliminates the need for an external gate electrode and is hence amenable to the complete integration of the nanosensor as is highly desirable for analyte detection in liquid media. The use of a high- κ dielectric allows the device to operate at low gate voltages and avoids errors caused by gate capacitance variations. Experimental data from the nanosensor showed measurements of pH in a range of 5.3 to 9.3 with a sensitivity of ~ 57.6

mV/pH. The pH-dependent electrical responses of the nanosensor responsible for the measurements were found to be caused by the charging of the electric double layer capacitor, rather than surface transfer doping. These results suggest that the GFET nanosensor can be potentially used to enable highly integrated sensing of chemical and biological analytes.

Further improvements of the GFET sensor could include complement of the data collection and processing part toward a more integrated and fully functional system. Also, the specificity, long-term stability, resistance to environmental perturbances need to be tested, with efforts on reducing the influences of biofouling for measurements in real biochemical samples.

Chapter 4

Graphene-metallic metasurface plasmonic sensors

4.1 Introduction to plasmonic sensors

4.1.1 Standard surface plasmonic resonance sensor

The surface plasmon polariton is a surface wave that propagates along the interface of metal and dielectric material. Since the wave is at the interface of the metallic and the environmental medium (air, water or vacuum for example), these oscillations are very sensitive to any changes applied to boundary, and therefore it can be used to detect the molecules that adsorbs on the conducting surface. The biosensors based on the surface plasmon resonance (SPR) has become a standard instrument in biological study¹¹¹. In addition to detecting or quantifying biomolecules, they are also used to study the binding kinetics of a target analyte with its receptor.

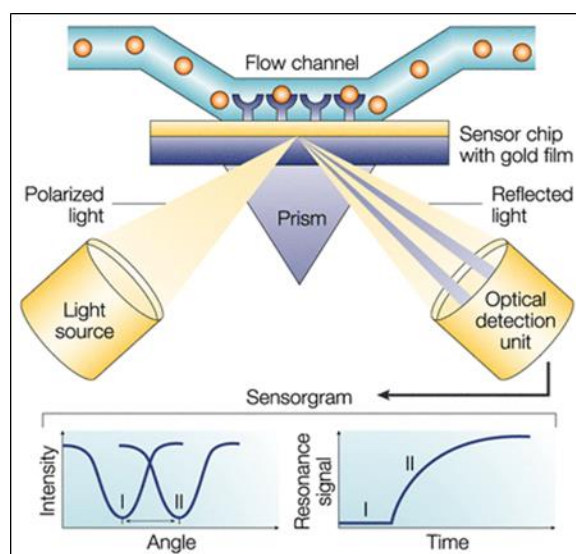


Figure 4.1: Schematics of the setup of a standard SPR sensor. [Adapted from M. Cooper *et al.* Nature Reviews, 2002]

The surface plasmon can be excited using a prism which can control the angle of the light transmission to the interface of metal and dielectric (for example the biological fluid). With receptor molecules functionalized on the metal surface, upon presence of corresponding target analytes in the fluid, their interaction will cause changes in refractive index at the interface and therefore changes the transmission of the light, for example the incidence angle at which the light can resonate with the surface plasmon.

To ensure the signals come from the analyte of interest, specific receptors need to be firstly functionalized on the surface of the metal. While the SPR sensor have enabled detection and characterization of behaviors of large molecules, its sensitivity is limited by the molecular-mass and therefore insufficient to detect small molecules, of which the molecular-mass is below 500 g/mol. This is because the classic SPR sensor mainly detect the changes in the bulk refractive index, which does not significantly change due to the binding of the monolayer small molecules on the surface of the metal.

4.1.2 Refractive-index based localized plasmonic sensors

Different from the surface plasmon propagating along a flat surface, the localized surface plasmon (LSP) is the plasmon confined to a particle that in size is comparable to the wavelength of light (λ), usually nanostructures with designed geometries. The free electrons of the nanostructures can interact with the collective oscillation of the plasmon, which generates enhancement in the electrical field close to the surface of the nanostructure, although the enhancement rapidly decays with the distance to the nanostructure. For the LSP, there is a

plasmonic resonance frequency (λ_r), at which the extinction of the nanostructures reaches maximum, dependent on the refractive index of the surrounding environment¹¹².

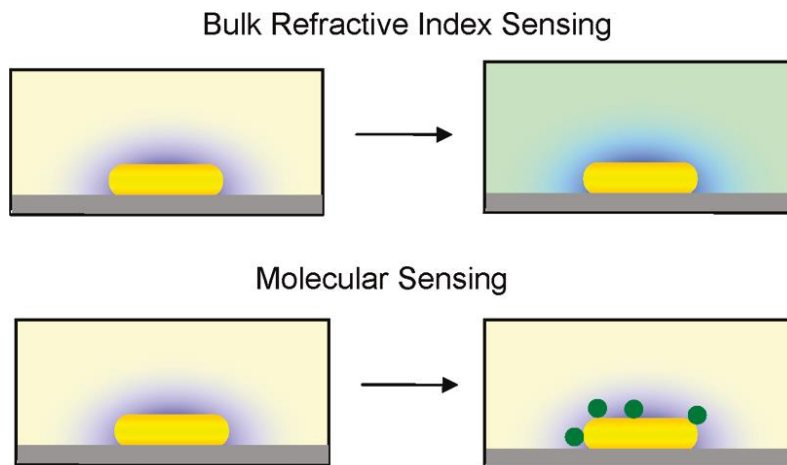


Figure 4.2: Two modes of the LSPR sensors: bulk refractive index sensing and local refractive index-based molecular sensing. [Adapted from K. Mayer *et al.* Chemical Reviews, 2011.]

The dependence of λ_r on refractive index makes the LSP resonance (LSPR) based sensors able to detect changes in bulk refractive index, like the SPR sensors. But it is unique to LSPR sensors to be able to detect the changes in local refractive index because the electrical field is strongly confined to the local area near the surface of the nanostructures (Figure 4.2). Therefore, the LSPR sensors can more sensitively respond to the binding between the target analytes and the receptors immobilized at the surface of the nanostructures, especially when the concentrations of the analytes are too low to introduce significant changes in bulk refractive index of the medium such as buffer.

While the sensitivity of the LSPR based sensors has been in general improved over that of the conventional SPR sensor, some issues still exist with the refractive-index based sensors. First, as

the refractive index can be changed by any materials adsorbed on the surface, or even variations in temperature and humidity, the shifts of the plasmonic resonance frequency may not result from the binding of the target analytes of interest. Second is the incapability of detecting very small molecules with low-molecular-weight. While the LSPR sensors have demonstrated higher sensitivity in sensing of some small protein molecules such as insulin, it remains challenging to quantify even smaller molecules such as metal ions, monosaccharides and so forth, in particular at low concentrations.

Here, employing engineered metasurface with its plasmonic resonance frequency in mid-IR region, we demonstrated sensors that allows both quantification and identification of biomolecules in a single measurement. Then we present a hybrid metasurface-based sensor by loading monolayer graphene on the metallic metasurface. The plasmonic resonance frequency of the hybrid metasurface is no longer solely dependent on the refractive index, but also a function of the optical conductivity of graphene. Therefore, it can detect molecular doping from small molecules to graphene, independent of the molecular-mass of the analytes.

4.2 Metallic metasurface based mid-infrared sensors

This section presents a plasmonic biosensor that allows for detection of both concentrations and fingerprints of biomolecules. Human immunoglobulin G (IgG) concentrations down to 30 pM was resolved from the plasmonic resonance shift, corroborated by the increase in the intensities of protein amide I and amide II bands. Thanks to the enhancement of the interactions between microscale infrared light and nanoscale molecules, vibrational fingerprints of protein molecules (amide I and II) were achieved at the level of monolayer protein.

4.2.1 Sensor design and fabrication

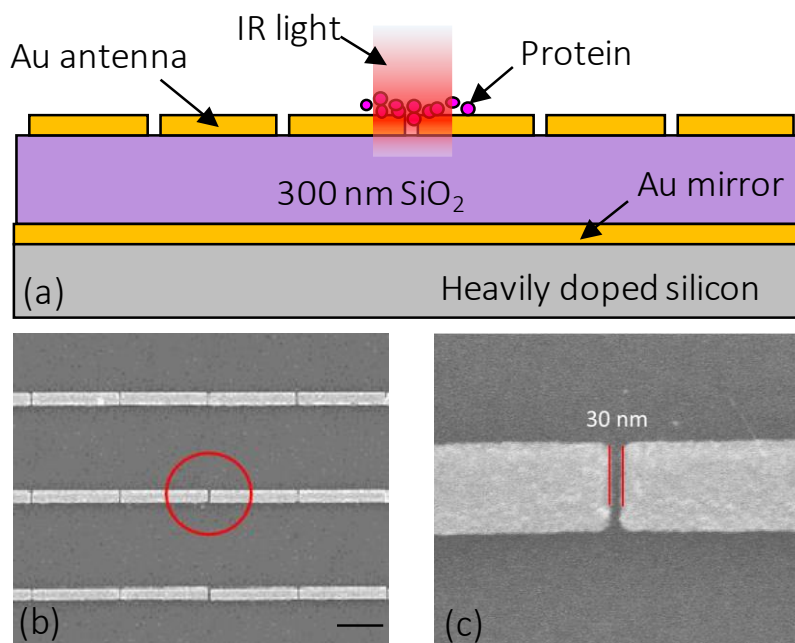


Figure 4.3: Sensor design. (a) Schematics of the sensor without graphene. (b) Scanning electron microscope photo of the fabricated sensor. Scale bar 1 μm . (c) Close-up of the circled region in (b). The gaps between neighboring antenna nanorods were approximately 30 nm.

The sensor consisted of an array of plasmonic nano-antennas on SiO₂ (Figure 4.3). Each antenna nanorod is 1.84 μm long separated from the neighboring antenna by a 30-nm gap. These antenna nanorods showed an intrinsic plasmon resonance at $\sim 1420\text{ cm}^{-1}$, in the mid-infrared range that overlaps with vibrational bands of most organic chemicals and biochemical molecules. A gold film under SiO₂ served as the back mirror to create a cavity with the oxide dielectric layer to further enhance the interactions of IR light and molecular vibration. Enhancement of the molecular vibrational spectral signal was a result of coupling of the vibrational resonance and the localized surface plasmon resonance. As the micro meter wavelength of IR significantly

mismatch with the size of nanometric biomolecules, confinement of the electric field in the close vicinity (~ 10 nm) of nanorods (Figure 4.4) can highly enhance the interactions between IR light and the biomolecules. The enhancement effect would be stronger when the plasmonic resonance frequency is closer to that of the molecular vibrational resonance. To fabricate the metasurface, 50 nm thick Au mirror were deposited on heavily doped silicon substrate, followed by deposition of 285 nm thick SiO₂ using plasma enhanced chemical vapor deposition (PECVD). Gold nanorods (thickness 50 nm) array was fabricated over a 400 μm by 400 μm area on the oxide layer using electron beam lithography, electron beam evaporation and lift-off.

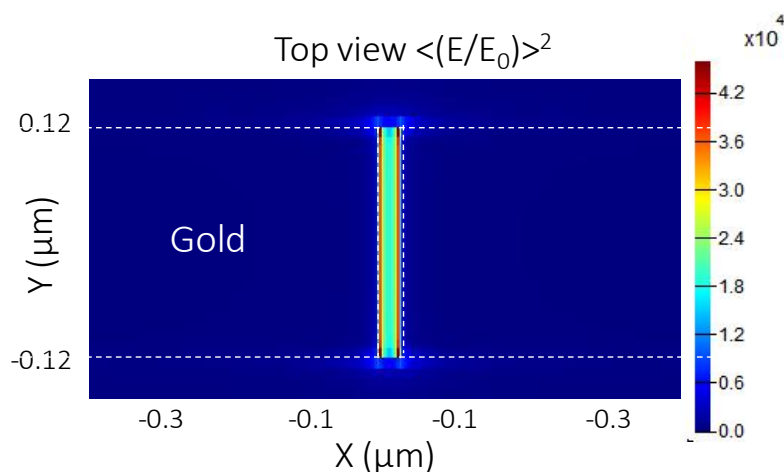


Figure 4.4: Top view of the electrical field distribution over a pair of gold antenna nanorods, calculated using finite-difference time-domain (FDTD) simulation. It is found that the near field is strongly confined in the close vicinity of the gold nano-antennas.

4.2.2 Quantification and fingerprinting of human Immunoglobulin G

We then performed measurement of human Immunoglobulin G (IgG). The optical absorption of the metasurface was characterized using Fourier transfer infrared spectroscopy (FTIR). Firstly, a monolayer of protein A/G was immobilized on the metasurface via physical adsorption. Protein

A/G at 1 mg/mL in phosphate buffer solution (PBS, pH 7.4) was drop-coated on the device and incubated for 1.5 hours at room temperature. The device was then gently washed by fresh buffer and deionize water for three times respectively, to remove free protein molecules. Upon immobilization of the monolayer protein (thickness ~ 3 nm), the plasmonic resonance was red-shifted by ~ 13 cm^{-1} . Also, the spectral signal around 1650 cm^{-1} and 1550 cm^{-1} were clearly observable in the measured IR spectra (Figure 4.5), thanks to the enhancement of the interaction between IR light and the protein molecules; they are respectively attributable to the protein amide I and amide II bands¹¹³, and further confirmed the successful immobilization of protein monolayer on the metasurface.

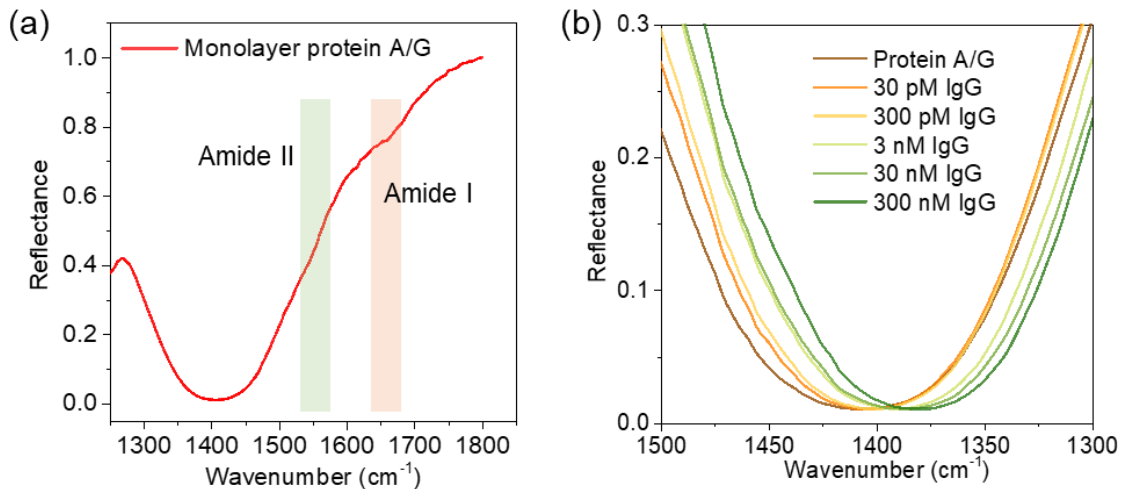


Figure 4.5: Detection of IgG. (a) Amide I and II bands after immobilization of monolayer protein A/G. (b) Shift of plasmon resonance caused by the binding of IgG and protein A/G.

In quantitative measurement of IgG, an antibody that can be specifically captured by the protein A/G via affinity binding, the sensor was then exposed to IgG solutions from 30 pM to 300 nM. Increase of the IgG concentration generated red-shifts of the resonance peak were, by increasing the local refractive index near the nano-antennas (Figure 4.5). The measured resonance shifts as

a function of IgG concentration $\Delta\omega_r$ were fitted to Langmuir isotherm model:

$$\Delta\omega_r = \Delta\omega_{\max} [C] / (K_d + [C])$$

where $\Delta\omega_{\max}$ is the maximum shift in wavenumber introduced by the IgG binding, approached when the binding is saturated the; K_d is the dissociation constant in nM as a measure of the affinity of the target to the receptor; and $[C]$ is the concentration of the IgG in buffer. The estimated dissociation constant was around 1.1 nM (Figure 4.6), slightly lower than the K_d for rabbit or mouse IgG binding to the same protein A/G, implying stronger affinity of human IgG to the protein A/G¹¹⁴.

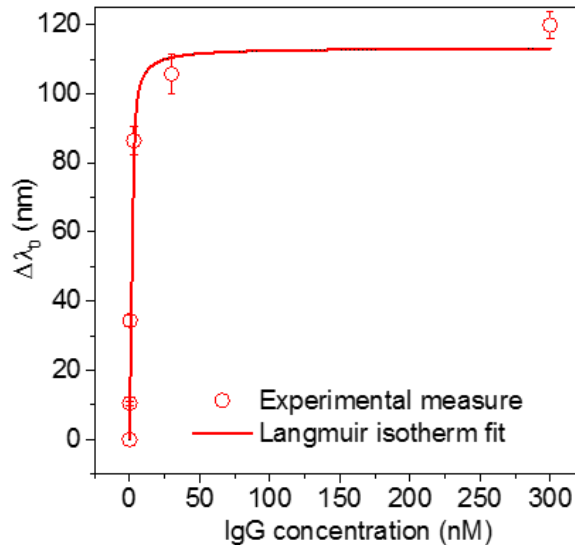


Figure 4.6: Fitting of the data points to the Langmuir isotherm yields a dissociation constant ~1.1 nM.

In addition to the plasmonic resonance shift, it was also found that the intensities of amide I monotonically increased with the IgG concentration, further confirming that the resonance shift was due to the addition of protein (Figure 4.7).

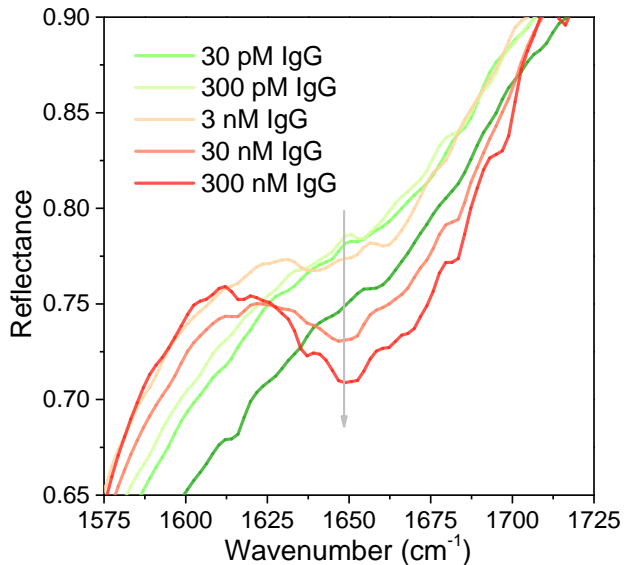


Figure 4.7: Increase in the intensity of amide I band confirmed successful binding of IgG.

This demonstrated that the sensor was able to in parallel monitor the molecule-binding-introduced refractive index changes and deliver the structural fingerprints of the molecules. This will not only effectively minimize possible false signals in optical measurements caused by environmental variances or contaminations, but also lead to achievement of molecular structural information in a more cost and time efficient manner using a small amount of sample.

4.3 Graphene-metallic hybrid metasurface based sensors

Small molecules such as amino acids, metal ions and monosaccharides play critical roles in biological processes including gene expression, protein-protein interaction and metabolic regulation. Experimental studies of their behaviors are in general challenging due to the difficulties in manipulating and detecting these low-molecular-mass molecules. For example, the sensitivity of standard surface plasmon resonance (SPR) biosensors is insufficient for detecting the binding of small molecules that occurs at the sensor surface. There has been intense interest

to develop methods for highly sensitive and efficient detection of small molecules. Metasurface based localized plasmonic sensors have become particularly promising because of their significantly improved sensitivity compared to conventional SPR sensors. Responses of these sensors, however, mostly still depend on the analyte mass or changes in local refractive index, which is not amenable to the detection of small molecules at low concentrations. This limitation is more significant for sensors operating in infrared (IR) region due to the weaker interaction between microscale IR light and nanometric molecules¹¹⁵. Thus, IR based biosensors have been rarely demonstrated for highly sensitive quantification of small molecules, although they typically can reveal molecular fingerprints and offer distinctive selectivity in biosensing¹¹⁶.

In this section, exploiting the unique optoelectronic properties of graphene in combination with engineered metallic metasurfaces, we present a solid-state mid-IR plasmonic nanosensor for ultrasensitive detection of small molecules. The graphene-metallic hybrid metasurface has its plasmonic resonance frequency in mid-IR region as a function of the optical conductivity, or carrier density of graphene¹¹⁷, thus can detect carrier doping from adsorbed molecules. The optical conductivity based plasmonic biosensor exhibits important advantages. First, the sensitivity of this sensor is no longer limited by the molecular mass and drastically improved thanks to the high sensitivity of graphene to molecular doping^{103,118}. The semi-metallic graphene, by strongly confining the electrical field near its surface, enhances its interaction with the field and in turn also improves the sensitivity. Second, molecules with similar molecular masses can be differentiated from the resonance shifts introduced by the changes in graphene optical conductivity rather than refractive index. Third, the sensitivity of our plasmonic sensor, mainly determined by the quality factor of the metallic metasurface, is highly stable and not susceptible

to degradation of graphene carrier mobility, in contrast to the field effect transistor based sensors^{119,120}. Finally, the vibrational fingerprints, especially when the analyte quantity is limited, can be largely enhanced by the strongly confined electrical field on the metasurface. This facilitates fast identification of analytes but has been non-trivial for most other biosensors.

Using this hybrid metasurface based nanosensor we demonstrated sensitive detection of small molecules. Monolayer low-molecular-mass pyrene derivatives were optically detected and differentiated from each other. Sub-monolayer glucose was reversibly quantified via its affinity binding with boronic acid on the graphene surface, from 2 nM to 20 mM, almost 5 orders of magnitude more sensitive than refractive index based plasmonic sensors. We also studied the effects of the antenna geometries on the sensitivity and further improved the sensitivity by shrinking the gap size to 10 nm between adjacent antennas using new fabrication methods.

4.3.1 Sensor principle, design and fabrication

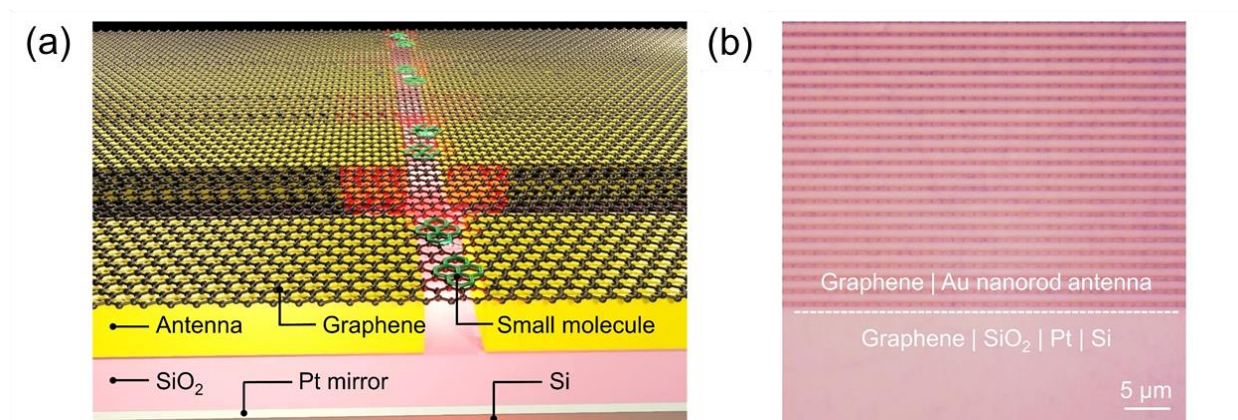


Figure 4.8: Schematic illustration and microscopy characterization of the hybrid metasurface.

(a) Schematic of the graphene-metallic metasurface, with pyrene groups adsorbed on the graphene surface. (b) Optical micrograph of the device.

The sensor consisted of Au antenna nanorods (length $L=1.64\ \mu\text{m}$) on SiO_2 with small gaps ($g\approx 30\ \text{nm}$) between neighboring nanorods (Figure 4.8). A Pt mirror under the SiO_2 created a cavity to suppress the optical transmission and enhance the quality factor of the plasmonic peak¹⁶.

Monolayer graphene was transferred onto the metallic antenna to create the graphene-metallic hybrid metasurface. Benefiting from its excellent mechanical strength and flexibility, graphene tightly wrapped the nanorods over the $400\ \mu\text{m}$ by $400\ \mu\text{m}$ region and suspended over the $30\ \text{nm}$ gaps (Figure 4.9). The plasmonic resonance exhibited by the device with as-transferred graphene was at around $1500\ \text{cm}^{-1}$, in the mid-IR region where the optical conductivity of graphene was highly tunable. The optical absorbance at the plasmonic resonance frequency (ω_r) of the hybrid metasurface was nearly 90% and dominantly stronger than that of the phonon resonances of dielectric oxide or organic residue. In contrast to the intrinsic graphene plasmon resonance that usually only generates an absorption of $\sim 5\%$, the more pronounced resonance peak offers a higher signal-to-noise ratio for sensing.

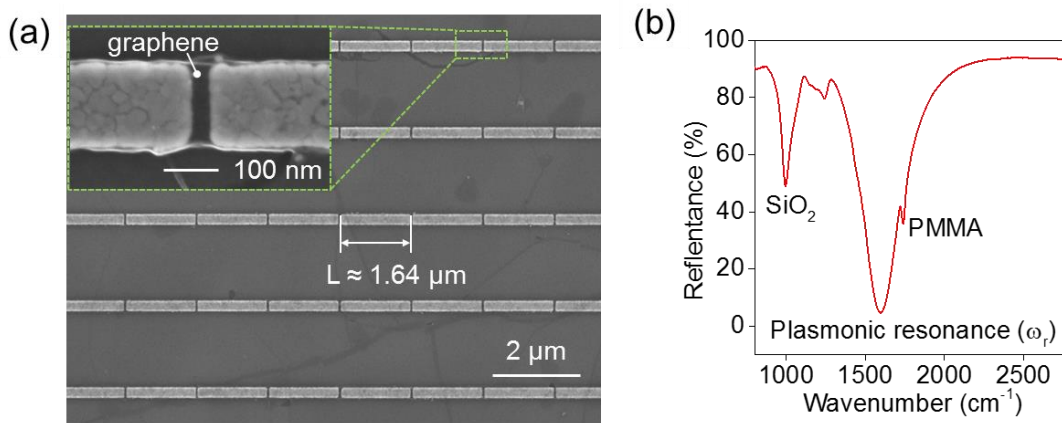


Figure 4.9: (a) Scanning electron microscopy photo of the nanorod antennas coated by monolayer graphene. Inset: Close-up image of the graphene suspended over the $30\ \text{nm}$ nanogap. (b) Optical absorbance of the metasurface with as-transferred graphene.

To fabricate graphene-metallic hybrid metasurface, 50 nm thick Pt mirror were deposited on heavily doped silicon substrate, followed by deposition of 285 nm thick SiO₂ using plasma enhanced chemical vapor deposition (PECVD). Gold nanorods (thickness 50 nm) array was fabricated over a 400 μm by 400 μm area on the oxide layer using electron beam lithography, electron beam evaporation and lift-off. Monolayer graphene grown on copper foil via chemical vapor deposition (CVD) was then transferred on the prepared gold nanorods using polymer (PMMA)-assisted wet transfer method. The polymer layer was lastly removed by rinsing the device in acetone for over 3 hours at room temperature.

4.3.2 Detection of sub-nanometer chemical molecules

To verify that the plasmonic resonance can be tuned by molecular doping, we altered the carrier density of graphene by chemical treatment in acetonitrile (ACN) and solutions (in ACN) of two pyrene derivatives - amino-pyrene (AP, 217.27 g/mol) and boronic acid-pyrene (BAP, 246.07 g/mol) (Figure 4.10), respectively. Raman spectroscopy indicated that the AP or BAP molecule was successfully immobilized on graphene and implied that the pure ACN bath could also generated doping to graphene.

This should be due to the charge transfer between the adsorbed molecules from or to graphene as these small organic molecules are typically non-charge but some of them may serve as n-type or p-type dopants. For example, the molecules containing boron may tend to withdraw electrons because there is an empty orbital on boron atom, which makes boron strong p-type dopants as frequently used in semiconductor industry.

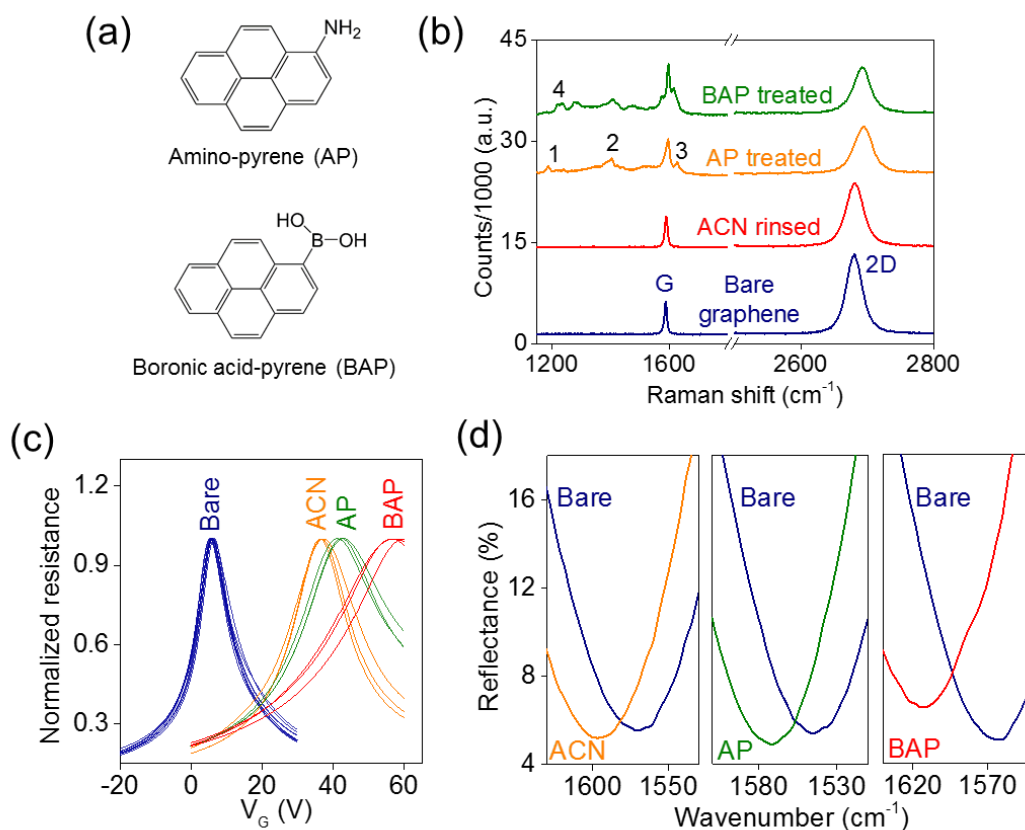


Figure 4.10: Detection of sub-nanometer chemical molecules. (a) Chemical structure of ACN, AP, and BAP. (b) Raman spectroscopy of graphene treated by different chemicals. (c) Characterization of the carrier doping (Δn) using field effect transistors. (d) Shift of the plasmonic resonance frequency by the molecular doping.

Transfer characteristics (Figure 4.10) measured using graphene field effect transistors (FET) confirmed that the pure acetonitrile bath introduced strong p-doping, increasing the hole density (Δn_h) by $2.3 \times 10^{12} \text{ cm}^{-2}$. Immobilization of AP and BAP molecules produced additional increase in hole density of $0.46 \times 10^{12} \text{ cm}^{-2}$ and $1.58 \times 10^{12} \text{ cm}^{-2}$, respectively. Fourier transform infrared spectroscopy (FTIR) was then used to characterize the plasmonic resonance frequency (ω_r) of the

metasurface. Compared to with untreated graphene, after treatment of ACN, AP and BAP, ω_r shifted to higher wavenumber by 23 cm^{-1} , 27 cm^{-1} , and 46 cm^{-1} , respectively.

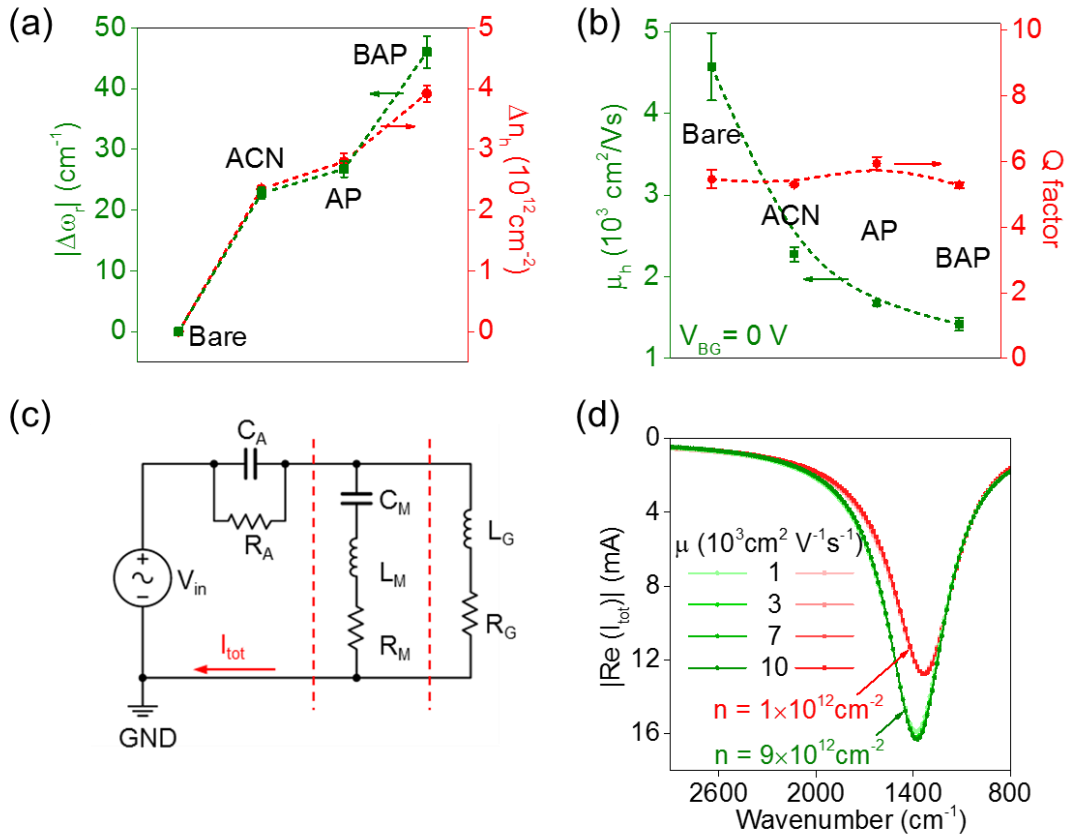


Figure 4.11: Influence of carrier density and mobility to the absorption spectroscopy of the metasurface. (a) Dependence of the amount of resonance shift on the carrier density. (b) Independence of the Q factor of the carrier mobility. (c) Equivalent circuit model of the metasurface. (d) Frequency response of the current I_{tot} .

The consistent blue-shifts are apparently not due to the increase in local refractive index, which should have red-shifted the resonance frequency as observed in typical plasmonic sensing. They instead should be attributed to the modulation of the graphene optical conductivity by the molecular doping. Increase in the graphene optical conductivity, as the molecules introduced

stronger p-doping, decreased the real-part of the graphene permittivity, thereby blue-shifting the plasmonic resonance¹²¹. The shift value $|\Delta\omega_r|$ strongly depended on the carrier density doped into graphene by the molecules (Figure 4.11) and allowed us to differentiate these molecules despite their similar and low molecular masses. This made the optical-conductivity based sensor more selective than refractive index-based sensors, especially for analytes with similar molecular structures and weights.

Besides the carrier density (n), the carrier mobility (μ) of graphene can also substantially influence the performance of graphene-based optoelectronic devices. For example, the sensitivity of the FET sensors linearly depends on the carrier mobility of graphene; also the magnitude and quality factor of the plasmonic resonance excited on graphene nanoribbons vary with graphene carrier density and mobility. Interestingly, for our hybrid metasurface sensor, the profile of the plasmonic resonance peak did not show appreciable deformation while the carrier mobility of graphene decreased significantly after chemical treatment, as is evident from the considerably less sharp transfer characteristics. The quality factor (Q) of the plasmonic resonance peak remained approximately constant at 5.5 within a deviation of 5.6% (Figure 4.11), although the hole mobility was lowered by nearly 70%, from $4570 \text{ cm}^2 \text{ V}^{-1}\text{s}^{-1}$ to $1420 \text{ cm}^2 \text{ V}^{-1}\text{s}^{-1}$.

To understand the impact of each component on the resonance frequency and quality factor, we developed an equivalent circuit to simulate the absorbance of the hybrid metasurface. The capacitance (C_A) and resistance (R_A) from the surrounding environment (i.e. air in our experiments) were in serial with the capacitance, inductance and resistance of the metal antenna array (C_M, L_M, R_M) and graphene (L_G, R_G). The minimum of the real-part of the current (I_{tot}) was

reached at the resonance frequency, i.e. ω_r . Similar to the experimental and FDTD simulation results, the frequency responses of the circuit, at different carrier densities and mobilities, also indicated that the Q factor was not sensitive to the graphene mobility. Thus, the plasmonic sensor offers robust solution to biosensing because biochemical functionalization and exposure to high-ionic strength solution can significantly vary the carrier mobility. In the circuit model, the initial values of R_A , C_A , R_M , L_M , and C_M were adapted from reference¹²¹ and graphene inductance L_G and resistance R_G were determined by theoretical calculation (Figure 4.12).

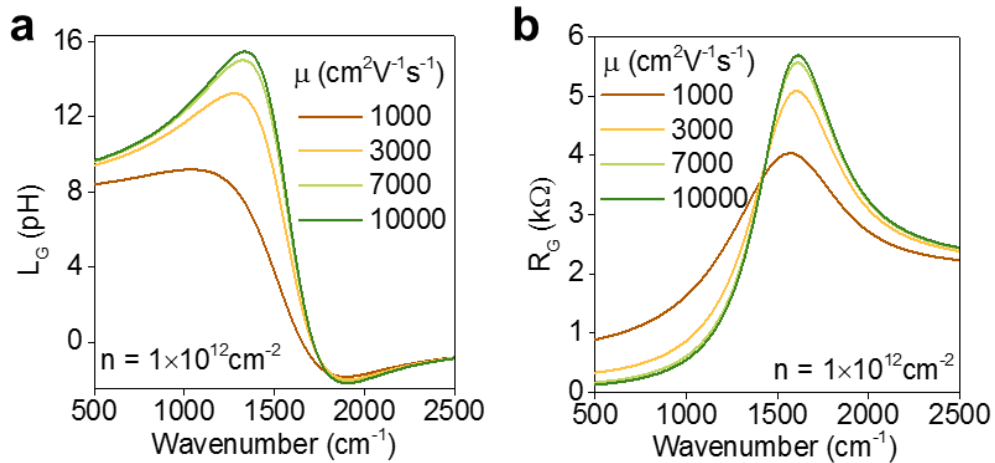


Figure 4.12: Calculation of the effective graphene inductance and resistance in the circuit model. Frequency dependent inductance L_G (a) and resistance R_G (b) at $n=1 \times 10^{12} \text{ cm}^{-2}$ and different mobilities.

In study of the effects of graphene carrier mobility, the L_G and R_G were set as constants equal to the values at wavelength of $7 \mu\text{m}$ (i.e. 1430 cm^{-1}) which was close to the plasmon resonance frequency. The parameter values for each component at different graphene carrier mobility was listed in Table 4.1. The simulation was run on the software Multisim.

Table 4-1: Parameter setup for simulation of the equivalent circuit.

V_{in} (V)	R_A (Ω)	C_A (F)	R_M (Ω)	L_M (H)	C_M (F)
100	1k	0.0321f	63	0.92p	0.0384f

Graphene carrier density $n=1 \times 10^{12} \text{cm}^{-2}$			Graphene carrier density $n=9 \times 10^{12} \text{cm}^{-2}$		
μ ($\text{cm}^2\text{V}^{-1}\text{s}^{-1}$)	R_G (Ω)	L_G (pH)	μ ($\text{cm}^2\text{V}^{-1}\text{s}^{-1}$)	R_G (Ω)	L_G (pH)
1000	3900	3.7	1000	117	3.3
3000	4500	8.9	3000	48	3.3
7000	4800	11.2	7000	28	3.3
10000	4900	11.7	10000	24	3.3

4.3.3 Detection of sub-nanometer metallic nanoparticles

To more carefully examine the contributions of the changes in optical conductivity and refractive index to the plasmonic resonance shift, a ultrathin layer (0.8 nm) aluminum (Al) was physically deposited on the bare Au nanorods and the graphene/Au hybrid metamaterials. Different from the pyrene derivatives that selectively couple with graphene, the Al nanoparticles could be homogeneously coated over the sensor surface, including the nanometric gaps regardless of graphene, so that the effects of the refractive index and the graphene optical conductivity could be equally evaluated. As the work function of Al ($W_{Al}=4.28$ eV) is lower than that of pristine graphene ($W_{Gr}=4.6$ eV), the Al nanoparticles in contact with the graphene upshifted the graphene Fermi level and donated electrons to graphene. From the measured transfer characteristics, it was found that the slightly p-doped (hole density $n_h=2.65 \times 10^{11} \text{cm}^{-2}$) graphene was converted to n-doped (electron density $n_e=3.48 \times 10^{12} \text{cm}^{-2}$), with an absolute carrier density increase of $3.21 \times 10^{12} \text{cm}^{-2}$ (Figure 4.13). FTIR measurements then found that these sub-nanometer Al

particles generated a large blue-shift of 24.1 cm^{-1} on the graphene-metallic hybrid metasurface but a much smaller red-shift of 2.2 cm^{-1} on the pure Au antenna. This suggested that the variation in graphene optical conductivity blue-shifted the plasmonic resonance by $24.1+2.2=26.3 \text{ cm}^{-1}$, 12 folds of the shift due to the change in the refractive index. This affirmed the dominant contribution of the graphene optical conductivity in detection of these sub-nanometer molecules. The BAP molecules were found even smaller which an apparent diameter of around 0.5 nm^{122} , therefore the shift of the plasmonic resonance caused by the refractive index change upon binding of BAP could be even smaller than 2.2 cm^{-1} and almost negligible.

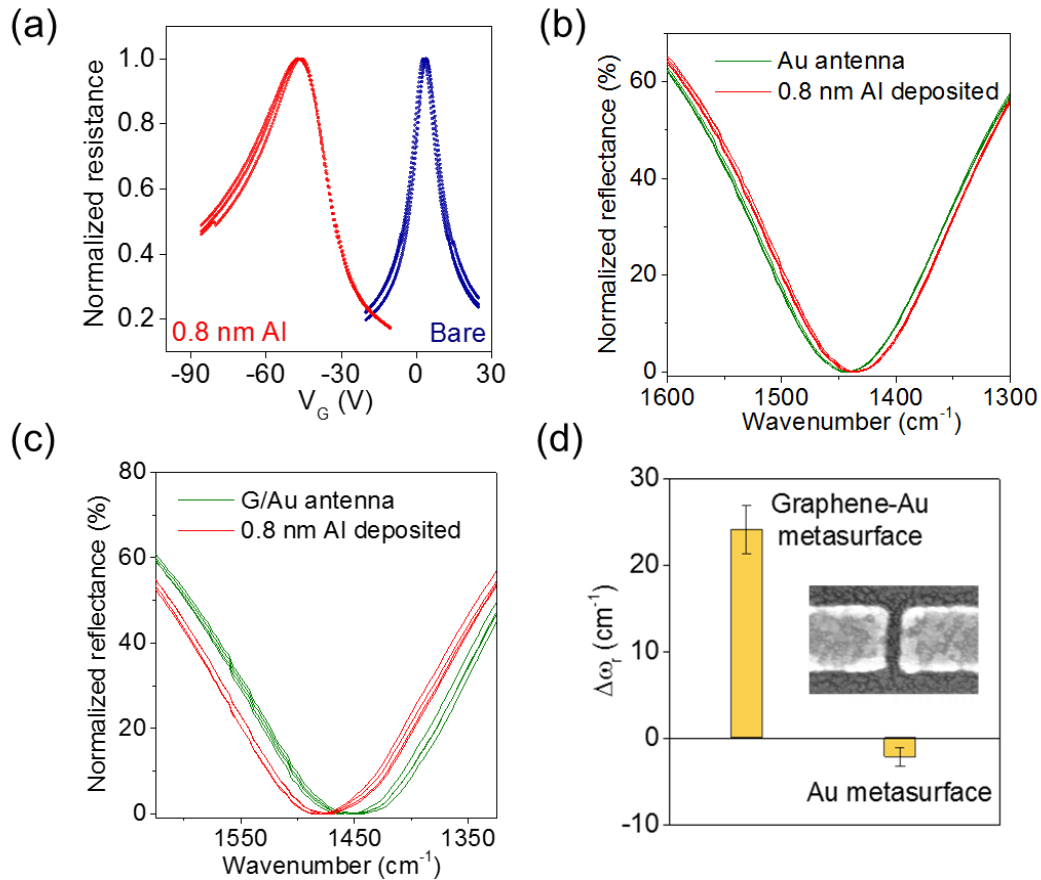


Figure 4.13: Detection of 0.8 nm Al nanoparticles. (a) Characterization of carrier doping of Al particles. Inset: Bandgap diagram before and after deposition of Al. (b) Measurement results on

pure Au metasurface. (c) Measurement results on hybrid metasurface. (d) Comparison of the results. Inset: SEM photo of the deposited Al nanoparticles on graphene.

4.3.4 Reversible measurement of glucose

As a proof of concept to demonstrate sensitive measurements of small-molecule biomarkers using the hybrid metasurface, in the following we performed measurement of glucose, a monosaccharide that serves as important source of energy in cellular respiration. Recently the affinity binding between glucose and boronic acid has attracted much attention in development of next-generation, enzyme-free and oxygen independent synthetic chemosensors¹²³. However, affinity binding-based optical methods for accurate detection of the monosaccharide at low concentrations are scarce, possibly due to the low molecular mass of glucose. It has been shown that, upon glucose binding, the boronic acid could be converted from an electron-withdrawing group to an electron-donating group^{86,124}. This transition of the boronic acid is expected to give rise to changes in the graphene optical conductivity and allow for glucose sensing on the hybrid metasurface.

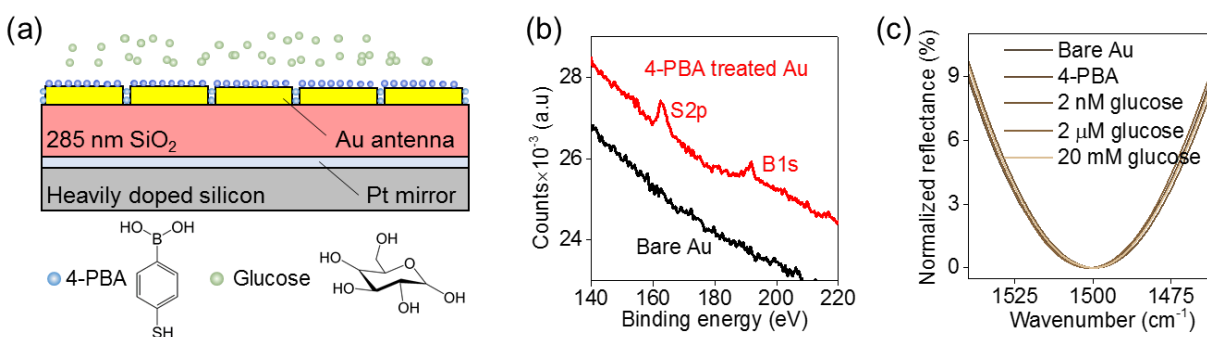


Figure 4.14: Control experiments on pure metallic metasurface functionalized with boronic acid.

(a) Schematics of sensor configuration. (b) X-ray photoelectron spectroscopy of 4-PBA functionalized Au antenna. (c) Measurement results.

To first examine possible responses introduced by refractive index variation, control experiments were conducted on pure Au metasurface treated by 4-mercaptophenylboronic acid (4-PBA) (Figure 4.14). The total shift of the plasmonic resonance from bare Au antenna to 4-PBA immobilization and exposure to 20 mM glucose solutions was merely 2 cm^{-1} , hardly distinguishable from each other. This corroborated the inability of monolayer small molecule to introduce significant variation in the refractive index.

We then performed measurements on the hybrid metasurface (Figure 4.15). When the graphene was treated by BAP, the plasmonic resonance significantly shifted to lower wavenumber after exposure of the device to glucose solutions. This was because that the p-doping of boronic acid to graphene was reduced by the glucose binding, and the graphene optical conductivity was decreased. The increase and decrease in hole density could be described by the molecular doping effects in the situation that the boronic acid was directly immobilized on graphene with no distance. Binding of boronic acid and 2 nM (0.36 ng/mL) glucose led to a clearly resolvable red-shift of 1.5 cm^{-1} . Compared with existing affinity based optical glucose sensors that measured the changes in local or bulk refractive index^{14,125,126}, the detection limit is improved by almost 5 orders of magnitude. Increasing glucose concentration to 20 mM monotonically red-shifted the plasmonic resonance. Fitting of the experimental results to the Hill-Langmuir equation gave an estimated dissociation constant of $99.2\text{ }\mu\text{M}$. Thanks to the reversibility of the glucose-boronic acid binding, the sensor can also detect both increasing and decreasing glucose levels. The wide detection range (2 nM – 20 mM, 7 orders of magnitude) is physiologically relevant as it covers the glucose levels in blood and in other body fluid such as tear and urine (μM to mM), making

the sensor not only important in fundamental research, but potentially applicable in non-invasive glucose monitoring.

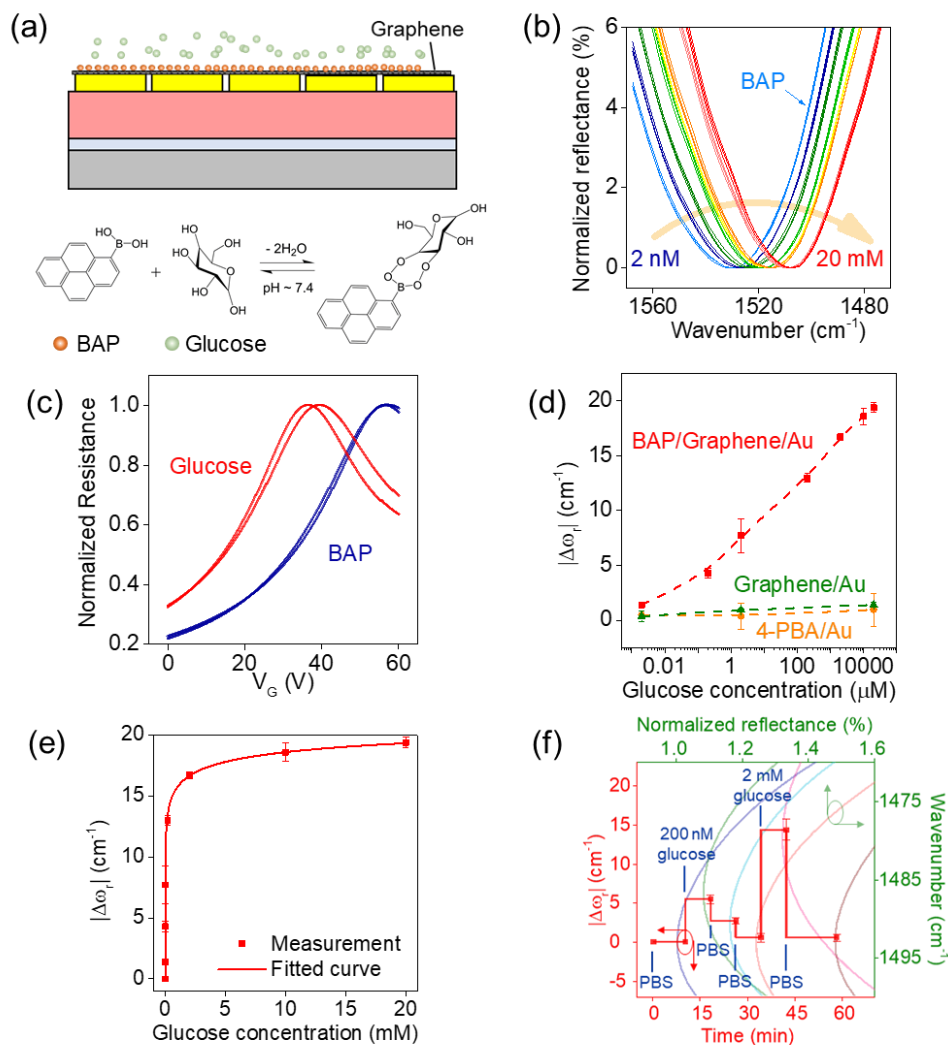


Figure 4.15: Quantitative measurements of glucose on the hybrid metasurface. (a) Configuration of the hybrid metasurface sensor. (b) Measurement of glucose from 2 nM to 20 mM on the hybrid metasurface. (c) FET characterization of the n-doping introduced by glucose-boronic acid binding. (d) Dependence of $|\Delta\omega_r|$ on the glucose concentration. (e) Langmuir fitting of the measured $|\Delta\omega_r|$. (f) Reversible measurement of glucose. Each data point is the average of 9 measurements on three devices and the error bar represents the standard deviation.

4.3.5 Dependence of sensitivity on metasurface geometry

Typically, on plasmonic biosensors higher sensitivity to local refractive index is achieved on antenna geometry with sharper corners, e.g. triangle, where electromagnetic field hot-spots are generated¹²⁷. To understand if this principle is applicable to the optical conductivity-based biosensor, we designed another two shapes of antenna, disk and diamond, to compare with the rod antenna and study the influence of the antenna geometry on the sensitivity. The nearest distances between the adjacent antennas were kept at ~ 30 nm for all the three shapes of antenna (Figure 4.16). Measurements of 2 mM glucose caused relative shifts ($\Delta\omega_r/\omega_{r0}$) of 1.09%, 0.54% and 0.38% for rod, disk and diamond antennas respectively. The sensitivities of the disk and diamond antenna metasurfaces were reduced to 49.5% and 34.9% of that on rod antenna, in agreement with the simulation results, where the relative shifts introduced by a large modulation of graphene carrier density ($\Delta n = 8 \times 10^{12}/\text{cm}^2$) on disk and diamond were 57.8% and 54.1% of that on rod antenna.

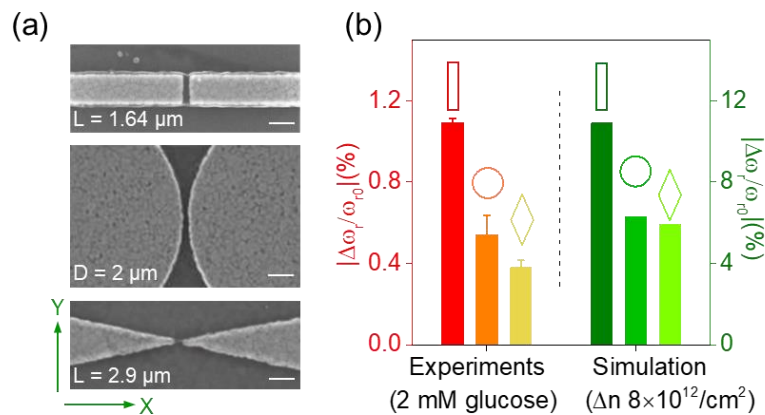


Figure 4.16: Dependence of the sensitivity on antenna geometry. Left: SEM photos of rod, disk and diamond antennas. Gap length $g=30$ nm. Scale bars, 100 nm. Right: Comparison of the relative shifts obtained with different geometries.

The sharp end on the diamond antenna did not bring up an increase in sensitivity, implying that the field confinement on the graphene-metallic metasurface was different from the pure metallic metasurface. The near field simulation (Figure 4.17) showed that while the field was mainly confined at the edge or corners on the pure metallic antennas, the semi-metallic graphene membrane led the field to be confined and distributed over the gap at the graphene surface and thus created more hot spots for graphene to interact with light. In this scenario, the shift of the plasmonic resonance would be influenced by both the intensity of the confined light and the area of graphene interacting with the light, as indicated by the equation below.

$$\frac{\Delta\omega_r}{\Delta\omega_{r0}} \approx \frac{-t \iiint_S dS (\Delta\bar{\varepsilon} \cdot \bar{E}) \cdot \bar{E}_0^*}{\iiint_V dV (\varepsilon \cdot \bar{E}_0) \cdot \bar{E}_0^*}$$

Here $\Delta\bar{\varepsilon}$ is perturbations of material permittivity (ε), \bar{E} is the electric field upon perturbation. \bar{E}_0 presents unperturbed fields while \bar{E}_0^* its conjugate. While both the denominator and numerator integrate over the space (V) of the system, the integration term in the numerator is non-zero only in the area (S) where the confined field overlap the graphene monolayer (thickness t). Note that on both disk and diamond antennas, the field intensity decayed very rapidly with the gap length. Therefore, it is possible that the broadening of the gap, while increasing the overlapping area S , overall weakened the interaction between graphene and the EM field and decreased the sensitivity.

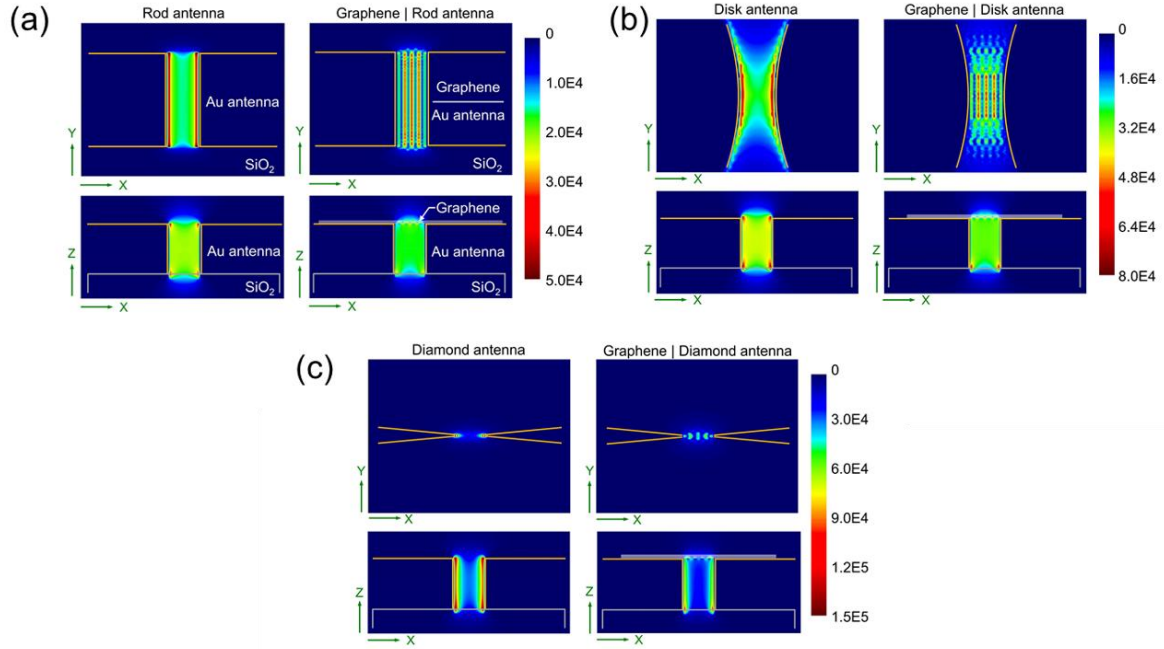


Figure 4.17: Near-field simulation for three antenna geometries. Left: pure metallic antennas. Right: Graphene-coated antennas.

Study of the effect of gap length g on the sensitivity was then conducted on nanorod antenna. With g increased from 30 nm to 100 and 200 nm (Figure 4.18), the relative shifts introduced by 20 mM glucose decreased from 1.28% to 0.62% and 0.22% cm^{-1} , by nearly 50% and 80% respectively. Similar to the observation on the disk and diamond antennas, increasing g reduced the field intensity, possibly by weakening the coupling or interference between the field confined by each single antenna. Based on the near-field distribution, we also theoretically evaluated the relative shifts. Writing $(\Delta\omega_r/\omega_{r0})$ in its scalar form gives an expression of the relative shift as a sum of two terms:

$$\left| \frac{\Delta\omega_r}{\omega_{r0}} \right| \propto |\Delta\varepsilon| \cdot \left| \frac{\iiint dS (\vec{E} \cdot \vec{E}_0^*)}{\iiint dV (\varepsilon |\vec{E}_0|^2)} \right| = |\Delta\varepsilon| \cdot K$$

$$K = \left| \frac{\iiint dS (\vec{E} \cdot \vec{E}_0^*)}{\iiint dV (\mu |\vec{H}_0|^2 + \varepsilon |\vec{E}_0|^2)} \right|$$

Here $\Delta\varepsilon$ represents the change of the local permittivity due to the variation of graphene optical conductivity, which is constant for a given carrier doping to graphene. The factor K is a variant representing relative change of electric field energy distribution, which is dependent on the antenna geometry and can be calculated from the electric near-field distribution (Figure 4.17, Figure 4.18c). The trends of the theoretically calculated K and the simulated $\Delta\omega_r/\omega_{r0}$ agreed nicely with each other for the above five antenna geometries. This confirmed that the nanorod antenna with 30 nm gap offers higher sensitivity than disk and diamond antennas, as well as the rod antennas with larger gaps. According to the theory, these results indicate that the nanorod antenna have achieved a strongest energy confinement among the three commonly used geometric shapes, thanks to the excellent balance between the electric field enhancement and the volume where the electric field is enhanced. On the other hand, for nanorod antennas, broadening of the gap leads to an increase in perturbation area but a more rapid decay of the electric field enhancement, thus overall lowers the integral of the electric field energy and degrades the sensitivity.

It is noteworthy that the electric field distribution is changed significantly by adding a monolayer graphene on the metallic antennas. In presence of graphene at the nanometric gap, the electric fields forms standing waves with a maximum enhancement at the center of the suspended graphene, whereas the electric field is only efficiently enhanced at the edges of the antennas for bare metallic metasurface. Superior to the very limited binding sites at the antenna edges, the

suspended graphene offers more binding sites for target molecules, hence can additionally improve the sensitivity of the sensor by increasing the light-matter interaction volume.

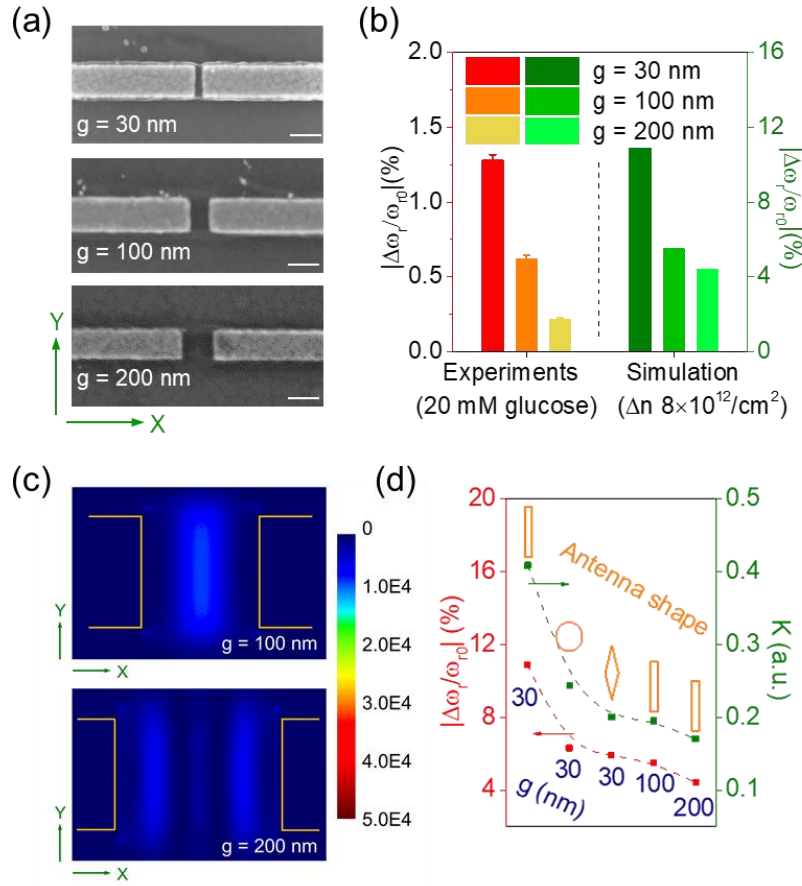


Figure 4.18: Study of the effects of the gap size on the sensitivity. (a) SEM photos of rod antennas with $g=30$, 100, and 200 nm. (b) Comparison of the relative shifts obtained with different gap sizes. (c) Near-field simulation for $g=100$ and 200 nm. (d) Plots of $|\Delta\omega_r/\omega_{r0}|$ and K at $\Delta n=10^8 \text{cm}^{-2}$ for different antenna geometries.

The monotonic increase of the sensitivity with the decrease of the gap length predicts that the sensitivity would continue to improve by bringing the neighboring antennas even closer to each other. Reducing the gap to below 30 nm would be very challenging for standard lithography and

lift-off process considering the high aspect ratio and the high density of the antennas (~50000 antennas in a $400 \times 400 \mu\text{m}^2$ area). We hence developed unconventional methods to fabricate the antenna array with g of 10 nm (Figure 4.19). First, a layer of Al_2O_3 was deposited on the SiO_2 as protection layer using atomic layer deposition (ALD), on which Pt antennas with initial gap of 30 nm were fabricated and additional 10 nm Pt was homogenously grown using ALD. Then 10 nm thick Pt was etched using inductively coupled plasma (ICP) to create the 10 nm gaps between adjacent antennas.

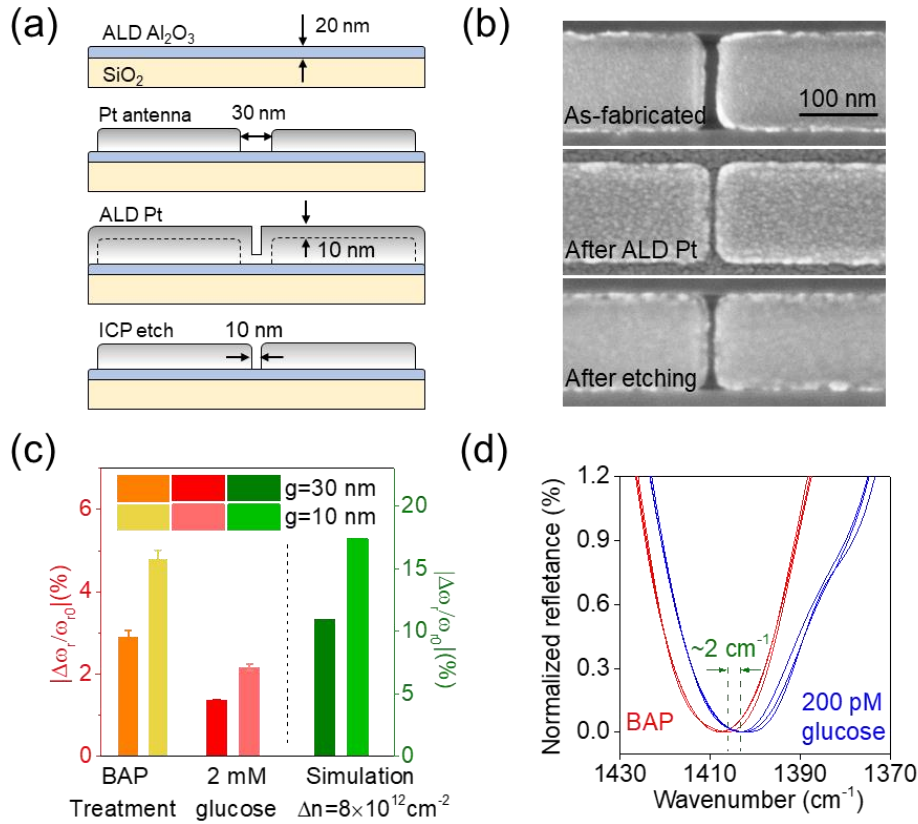


Figure 4.19: Further improvement of sensitivity by shrinking the gap length. (a) Fabrication process of the 10 nm gap between neighboring antennas. (b) SEM photos of a pair of antennas at each step of fabrication. (c) Comparison of the sensitivities for $g=30$ and 10 nm. (d) Detection of 200 pM glucose with $g=10$ nm.

On the 10 nm gap antennas, treatment of graphene with BAP generated a relative blue shift of 4.77%, which was 64% larger than that on nanorods with 30 nm gaps. Exposure of the BAP activated metasurface to 2 mM glucose introduced a relative shift of 1.76%, which was also improved by 60% compared to $g=30$ nm. On the side of low concentration, 200 pM (36 pg/mL) glucose was detectable on the 10 nm gap metasurface, indicating that the detection limit of the sensor was further improved by approximately one order of magnitude.

4.3.6 Enhancement of molecule vibrational fingerprints

The IR spectroscopy can also probe the fingerprints of the target molecules for identification of the analytes. More importantly, the fingerprints of the small molecules, when close to the plasmonic resonance of the metasurface, can be enhanced by the plasmon-phonon interaction. Here, to avoid interference of SiO₂ fingerprints, we mainly examined the enhancement effects for the glucose fingerprints^{128,129} located at 1300 - 1500 cm⁻¹ (OCH deformation) which were typically less stronger than other bands such as the OH vibration near 3000 cm⁻¹. First, 500 picomolar glucose was applied on the device. On the substrate (SiO₂/Pt), when the absorbance (ΔR) of the OH band was as weak as 4.2%, other peaks of glucose was hardly recognizable (Figure 4.20).

In contrast, given the similar intensity of the OH group, the spectrum measured on the metasurface unambiguously exhibited peaks at 1470 cm⁻¹ and 1320 cm⁻¹ corresponding to the OCH deformation of glucose molecules. This suggested that the plasmonic resonance contributed enhancement to the phonon resonances at the frequencies near the plasmonic

resonance. Specifically, in our case, with the plasmonic resonance at $\sim 1500\text{ cm}^{-1}$ and a bandwidth of $\sim 250\text{ cm}^{-1}$, the fingerprints (e.g. C-O-H) lying between $1250 - 1750\text{ cm}^{-1}$ can achieve much higher enhancement than those at other frequencies, for example, the O-H band and other fingerprints of glucose. The enhancement effect was also observed on the peak at 1740 cm^{-1} that is assigned to the C=O bond of the polymethyl methacrylate (PMMA)¹³⁰ residue from the fabrication, while the other, weaker peaks of PMMA were not revealed. When the glucose was reduced to 50 picomolar, the OCH band at 1470 cm^{-1} was still acknowledgeable although there was no recognizable signal of OH band. These results demonstrated that the metasurface provided remarkable enhancement of the vibrational fingerprints, which can help identify analytes and exclude false signals in biochemical sensing, especially when the analyte quantity is limited.

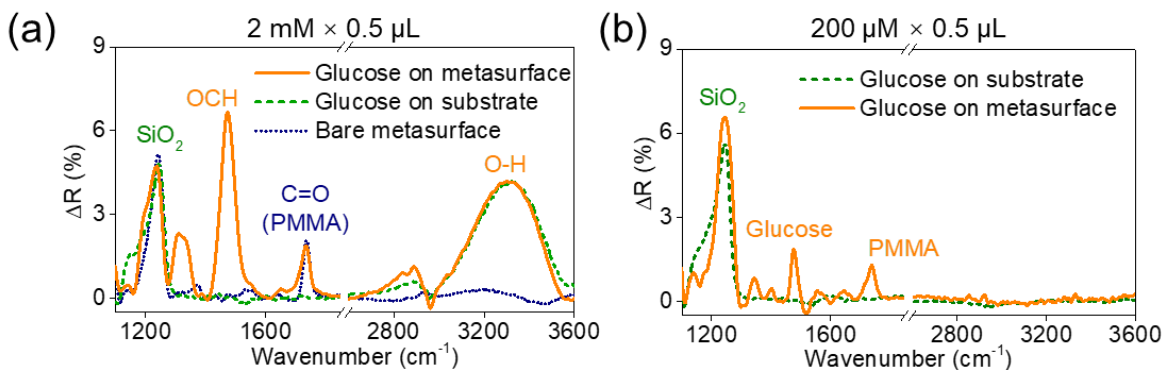


Figure 4.20: Enhancement of glucose fingerprints. Optical absorption (ΔR) measured before and after drop-coating (a) 500 picomolar and (b) 50 picomolar glucose on the device.

4.4 Chapter summary

In summary, in this chapter we presented metasurface based mid-infrared plasmonic biosensors for measurements of both analyte concentrations and fingerprints. In detection of large

biomolecules such as protein, pure metallic metasurface was used. the plasmonic resonance of the metallic metasurface was designed to be $\sim 1420 \text{ cm}^{-1}$. Spectral signals of vibrational resonance of amide I and amide II were achieved on monolayer protein A/G. Binding of human IgG from 30 pM to 300 nM to protein A/G was quantitatively resolved via the red-shift of the plasmonic resonance, confirmed by the increase in the intensities of protein amide I and amide II bands.

In detection of low-molecular-weight small molecules, graphene was loaded on the metallic metasurface to create a hybrid metasurface. The optical conductivity-based mediation of the plasmonic resonance enables ultrasensitive optical detection of small molecules on the graphene-metallic hybrid metasurface. This method relieves the optical detection limit from the molecular mass and allows for differentiation of certain analytes without additional receptors. Being able to detect sub-nanometer molecules such as monosaccharides, the sensor could also be used to detect other low-molecular-weight analytes, such as gas molecules, that are difficult to detect using conventional methods. Moreover, the molecules vibrational fingerprints can be sensitively revealed for structural analysis and classification of the analytes. The robust, power source-free sensor therefore holds promise for applications that require both high sensitivity and long-term stability, such as monitoring of disease biomarkers and inspection of safety-related poisons and explosives.

Chapter 5

Graphene bottom local-gated molybdenum disulfide transistors

In the third section of the Chapter 2, we presented a bottom local-gated graphene field effect biosensor, which provide multiple advantages over solution-gated sensors. Unfortunately, the tall sidewall of the metallic gate electrode is significantly higher than the 2D materials, therefore severely damages the material structure and affects the transport of electrons. It also increases the risk of gate leakage at the edges or the corners of the metal gate. Also, the zero band-gap of graphene fundamentally limits its sensitivity and hinders use of graphene in logic circuitry.

5.1 Introduction to transition metal dichalcogenide

Transition metal chalcogenide (TMDC), defined by its name, consists of transition metal and chalcogen atoms. These materials are typically formulated as MX_2 , in which M represents an transition metal element such as Ti, Zr, Hf, Nb, Ta, Mo, W and so forth, while X is an chalcogen element including S, Se and Te. The atomic structure of the TMDCs, like other 2D materials, is layered structure, typically with a layer of M atoms sandwiched by X atoms, i.e. X-M-X. The atomically thin layer of TMDCs have exhibited important and unique electrical and optical properties, including the semiconducting properties that is fundamental for developing logic electrical circuitries but not available on graphene. The direct bandgaps of some of the monolayer TMDCs, also lead to photoluminescence which have triggered extensive studies^{131,132} and found many applications in optoelectronics and photonics^{133,134}. Monolayer or few-layer TMDC materials can be achieved using either mechanical and chemical methods, as described below.

5.1.1 Preparation of two-dimensional transition metal dichalcogenide

Mechanical exfoliation can be used to isolate the thin layer TMDCs from its bulk material¹³⁵. This method has allowed for obtainment of very clean and high-quality single-crystal flake of 2D materials but unfortunately is not scalable. Large quantities of thin layer TMDCs can also be generated using ultrasonication in appropriate solutions¹³⁶⁻¹³⁸. The ultrasonication is equivalent to solution-phase exfoliation but apparently more efficient than mechanical cleavage using hands. But the layer number and flake quality and area are still out of control in this process. Upon exposure to solutions such organic solvents, the surface of the crystal would also degrade, possibly due to the non-covalent adsorption of organic molecules on the surface of the TMDCs.

The CVD method, as described in Chapter 2, is in general more promising for creating large-area, uniform high-quality thin-film materials including the atomically thin TMDCs. In a typical CVD synthesis of the 2D layers of TMDCs, for example the MoS₂, the source of Mo (e.g. MoO₂ powder) and the source of S (e.g. sulfur powder) are brought to each other under high temperature. The layer number and crystal area are highly dependent on the amount of the precursors, temperature and other experimental conditions. The recently demonstrated metal-oxide CVD (MOCVD) method has enabled growth of wafer-scale, spatially uniform monolayer MoS₂, MoSe₂, and WS₂, representing important advances in preparation of the large-area 2D semiconducting materials^{139,140}. The reported growth usually take place on insulating materials such SiO₂, which is compatible with Si based micro- and nano-electronic fabrication. Due to the diffusion of the precursors into the insulating materials, the dielectric strength of the insulating layer may degrade and therefore fabrication of electronic devices using the 2D materials needs transfer of the material onto separate substrates. Etching the growth substrate can directly release

the 2D layers but consumes much time and materials. Thanks to the weak interaction between the TMDCs and the substrate, delamination transfer of these materials from the smooth substrate proves easier than delamination of graphene. Wafer-scale monolayer TMDCs have been successfully transferred without significant damage using thermal release tape (TRT)^{139,141}. More interestingly, the water can easily diffuse into the interface of the TMDCs and the substrate, then lift the TMDC layers off the substrate¹⁴², thereby making the transfer more efficient.

5.1.2 Electrical properties of transition metal dichalcogenide

In pursuit of scaling of field effect transistors with high performance, it is vital to address increasing risks in undesired tunneling between electrodes as the critical feature sizes are reduced to few nanometers^{140,143-147}. Emerging low-dimensional materials with intrinsic nanometric sizes have become promising candidates to replace silicon in typical transistors (FET) and to develop novel complex circuitry architectures. Two-dimensional (2D) materials such as graphene and transition metal dichalcogenides (TMDs) are especially attractive as they can be uniformly prepared with atomic-level thickness at wafer scale, readily transferrable and stackable. Also, high-efficiency electrostatic gating of the ultrathin and flat 2D materials can be realized from either top or bottom, in contrast to the multi-gate required on bulk (and some 1D) materials¹⁴⁷. Excellent switching characteristics, such as high on-off ratio, low hysteresis and high mobility have been respectively demonstrated on TMDs transistors in individual works, although collective achievement of more of ideal device parameters, together with these listed above, would be required toward developing commercial devices but remains challenging. For example, it was found that surface treatment or thick dielectric layer is needed for scaled and reliable integration of high-k (k: relative dielectric constant) dielectrics on MoS₂ (molybdenum

disulfide) surface¹⁴⁸, at expense of degradation of material properties or need of higher operation voltage. Also, due to their atomic thickness, TMDs monolayers exhibit higher resistivity and lower mobility than their multilayer counterparts¹⁴⁹. Many high-performance devices with low subthreshold slope and high on-state current are demonstrated with exfoliated thick TMDs crystals instead of monolayers¹⁵⁰⁻¹⁵². In general, control of layer number in large-scale preparation of 2D materials remains very difficult while growth of wafer-level high-quality monolayer MoS₂ and graphene have been demonstrated¹⁵³. On the other side, atomically thin monolayer semiconductors would allow for ultimate scaling of the channel body, thus, it is important to explore methods that enable scalable high-performance transistors based on monolayer TMDs. Owing to their strong interactions with the substrate on which they are produced, TMDs monolayers are mostly handled at the level of individual exfoliated flakes¹⁵⁴, not amenable to large-scale fabrication and integration with other components.

5.2 Field effect transistors with graphene bottom local gate

In this section we present bottom-local-gate MoS₂ field effect transistors with monolayer graphene as the gate electrodes. The single-atomic-thick graphene shrinks the height of the gate electrode to physical limit and provides a smooth surface for growth of thin layer dielectric. The graphene gate significantly minimizes the gate leakage, thereby allowing use of ultrathin gate dielectric and high gate bias. Using a single graphene gate, high doping levels of MoS₂ (above $5 \times 10^{13} \text{ cm}^{-2}$) were achieved electrostatically without chemical treatment, leading to a low contact resistance of $2.3 \text{ k}\Omega \cdot \mu\text{m}$ between Ni and monolayer MoS₂, as well as a nearly ideal subthreshold slope (SS) of 64 mV/decade at room temperature. Scaled devices with 50 nm and 14 nm short channels and 3.7 nm gate dielectric showed excellent switching characteristics. Furthermore, the

graphene gate makes the device highly transparent on flexible polymeric substrate, which can potentially be used in optical-related applications and wearable devices. Both the graphene and MoS₂ were prepared using chemical vapor deposition (CVD). This work utilized transfer techniques that allow reuse of both growth substrates, thus demonstrating a path to scalable fabrication.

5.2.1 Device design and fabrication

The devices utilized in this study consist of monolayer MoS₂ channel, contacted by metal electrodes, atop a graphite back gate with a thin high-*k* dielectric layer (Figure 5.1). To fabricate the devices, graphene grown on Cu foil was first electrochemically delaminated onto a thermally oxidized silicon substrate. The graphene was patterned using oxygen plasma etching with 1.2 nm thick Ti as the etch mask, which later also served as the seed layer for HfO₂ deposition¹⁵⁵. This avoided the use of hard-to-remove negative-tone resist and minimized damage to the graphene. Then HfO₂ (thickness varied) was deposited using atomic layer deposition, followed by aligned wet-dry transfer of the CVD MoS₂ monolayers. The average surface roughness of the channel region was approximately 4.1 Å, indicating an atomically flat surface. The Raman spectroscopy of the MoS₂/HfO₂/graphene stack displayed the E_{12g}¹ and A_{1g} bands separated by 19 cm⁻¹, as well as the G and 2D bands, which were characteristics of MoS₂ and graphene monolayers, respectively. The strong and spatially uniform signals of MoS₂ A_{1g} band and graphene G band in Raman mapping verified the undamaged MoS₂ flakes and the bottom graphene gates. The use of graphene as a back gate provided a major improvement in the quality of the dielectric layer. Figure 5.1 shows the measured leakage current through the graphene gate with 1.2 nm TiO₂ and HfO₂ of different thicknesses.

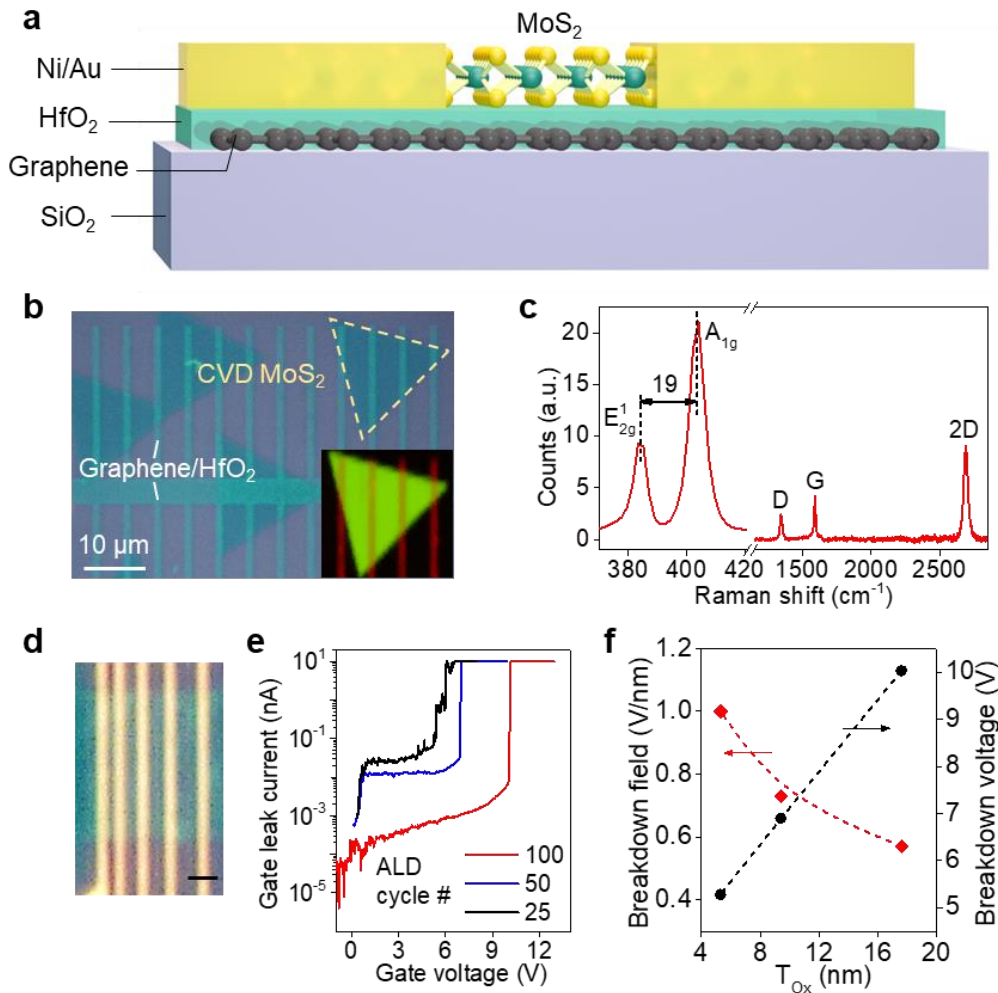


Figure 5.1: Device structure and characterization. (a) Schematic of the graphene bottom local-gate MoS₂ field effect transistor. (b) Microscopy photo of the MoS₂ dry-transferred onto the graphene/HfO₂. Inset: Raman mapping of the MoS₂ A_{1g} band (green) and the graphene 2D band (red). (c) Raman spectroscopy of the MoS₂ and graphene. (d) Optical micrograph of the fabricated devices with graphene gate (upper) and metal gate (lower). Scale bars: 1 μm. (e) Measurement of the gate leak current through the dielectric layer of different thickness, on graphene gate electrodes. (f) Breakdown field and voltage for the graphene gated devices as a function of the dielectric thickness.

For the graphene gate, the leakage remained below 10 pA before breakdown of the dielectric at a high voltage of 10 V, or a breakdown field of approximately 0.55 V/nm. Further decreasing the HfO₂ thickness (t_{Hf}) did not severely increase the gate leak. The breakdown field showed an increase with the decrease of the dielectric thickness. When only 25 cycles of HfO₂ was deposited, the breakdown field was increased to 1 V/nm. Such high field is critical to achieve high doping level but is in general very difficult to achieve, as oxide deposited on metal electrodes normally breaks down at displacement fields around 0.5 V/nm¹⁵⁶. We speculate that the improved performance arises from the the flatness and low profile of the graphene, which provides for a uniform dielectric thickness and eliminates field concentration at edges and sharp points found in thicker metal electrodes.

For position-specific transfer of CVD MoS₂, a wet-dry transfer method was developed (Figure 5.2). The monolayer MoS₂ flakes were firstly was delaminated from the growth substrate onto a polymer supporting layer (cellulose acetate butyrate, CAB) with assistance of water penetration, and then scooped using a glass slide. The atmospheric pressure allowed the MoS₂/CAB stack to be inverted and smoothly transferred onto the optically transparent elastomeric stamp on a foreign glass slide, made of poly-propylene carbonate and polydimethylsiloxane (PPC/PDMS). After attaching the MoS₂ flakes on the stamp, we performed further cleaning of MoS₂ using ultrapure water and gently blow dried the MoS₂ to remove impurities in water, which was important to attain clean MoS₂/oxide interface in the following but nontrivial in conventional transfer methods. The MoS₂ was then aligned with the graphene ribbon gates, and the PPC/CAB/MoS₂ was released from the stamp under heating. This transfer method provided notable improvement in handling CVD MoS₂ monolayers compared to direct pickup using polymer stack and may allow to build large-area 2D material heterostructures.

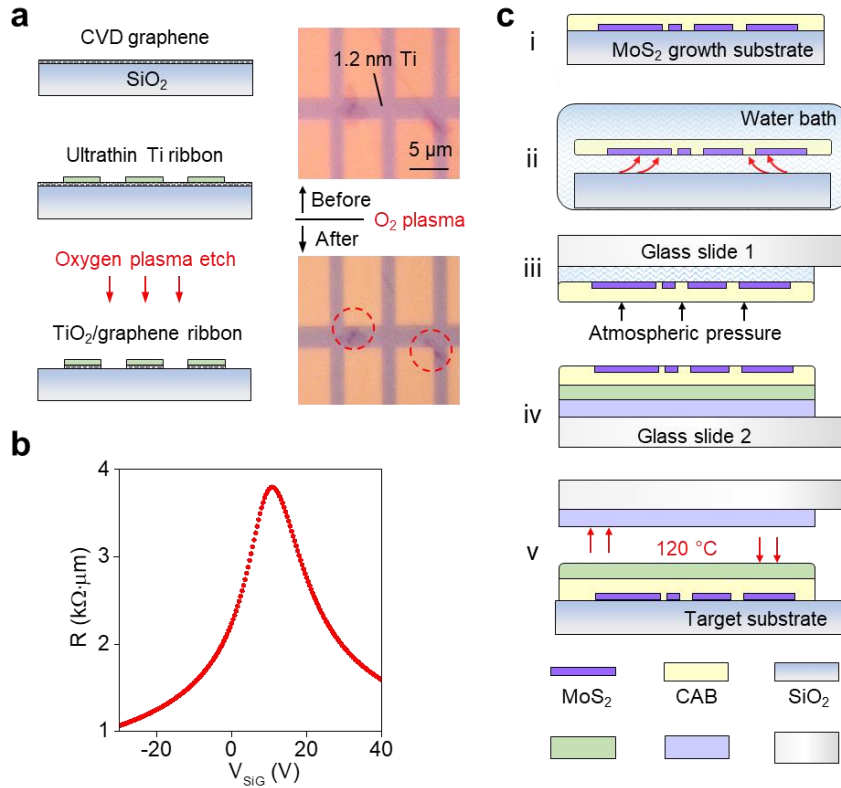


Figure 5.2: Fabrication process of the device. (a) Patterning of the graphene ribbon. (b) Gate voltage dependent conductivity of the patterned graphene ribbon. (c) Aligned transfer of the CVD monolayer MoS₂.

5.2.2 Electrical characterization

Figure 5.3 examines the performance of long-channel (1.5 μm) devices made with a relatively thick HfO₂ layer ($t_{\text{Hf}}=16$ nm) to demonstrate the device functionality and study the contact resistance (R_C). First, resembling conventional MOSFET configurations, the graphene gate was designed to only gate the channel region (partially gated). Upon sweeping the graphene gate voltage (V_{GG}) the device turned on with a subthreshold slope (SS) of 120 mV/decade. The channel conductance saturated at 0.4 μS/μm, with a low on/off ratio of 10⁵. This sub-optimal

performance can be attributed to large R_C as well as large lateral access resistance (R_U) of the ungated MoS_2 . Local chemical doping or phase transformation have been employed reduce R_C and R_U , but generally suffer from low stability. Alternatively, dual-gate operation, in which the contact areas are gated independently of the channel, can also reduce the contact resistance without the need of chemical treatment. However, it gives rise to more negative threshold voltages and complicates device fabrication and operation. Importantly, both chemical treatment and dual-gating make device scaling more challenging and difficult¹⁵⁷.

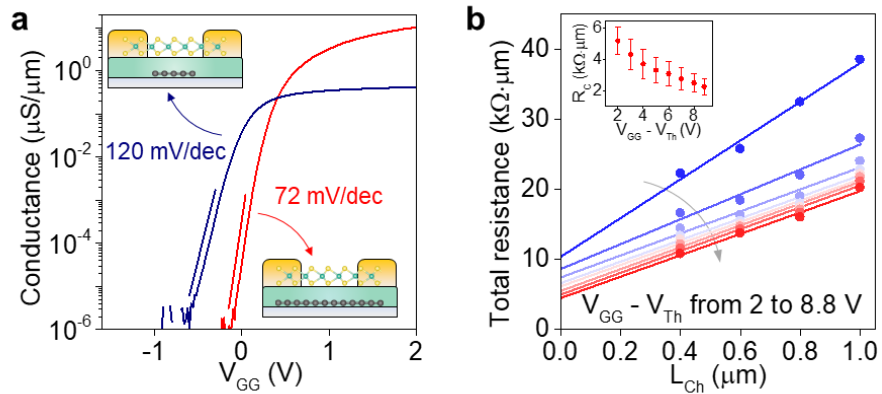


Figure 5.3: Comparison of device geometries and extraction of contact resistance. (a) Schematics and transport characteristics of the partially gated and fully gated devices. The channel lengths of both devices were $1.5 \mu\text{m}$. $T_{\text{Hf}} = 16 \text{ nm}$. (b) Extraction of R_C using transmission line method for the graphene gated device. Four channels with various channel lengths ($0.4, 0.6, 0.8$ and $1 \mu\text{m}$) were fabricated on a same MoS_2 flake. Inset: Gate voltage dependence of R_C . Error bars represent the standard error of the linear fitting.

Alternatively, dynamically modulating both the contact resistance R_C and the channel resistance R_{Ch} using a single gate can also overcome the issues associated with the large R_C . As shown in

Figure 5.3, when the graphene gate was extended to gate both the MoS₂ channel and the contact region, the device turned on more quickly, with a subthreshold slope of 72 mV/decade. In addition, the on-state conductance exceeded 10 $\mu\text{S}/\mu\text{m}$, giving an on/off ratio of 10^7 at low gate voltage of $V_{\text{GG}} = 2$ V, with threshold voltage (V_{Th}) of 0.4 V. Using the transmission line method we extracted R_{C} for this device, which reached values as low as 2.3 $\text{k}\Omega\cdot\mu\text{m}$ at gate voltage 8.8 V above V_{Th} , corresponding to a doping level of 5×10^{13} cm^{-2} . This high carrier density would be needed to meet the requirements of the International Technology Roadmap for Semiconductors (ITRS)¹⁵⁸ but have been scarcely demonstrated on intrinsic monolayer MoS₂.

Based on these results, in the following sections we examine the performance of devices with the graphene gate extending under the contact region. First, shrinking the channel length for devices with $T_{\text{Hf}} = 10$ nm results in a commensurate increase in output current (I_{DS}) to above 70 $\mu\text{A}/\mu\text{m}$ for a 600 nm channel (Figure 5.4) and above 100 $\mu\text{A}/\mu\text{m}$ for a 400 nm channel, at a source-drain voltage (V_{DS}) of 1 V. Both the output curves ($I_{\text{DS}}-V_{\text{DS}}$) and the transport characteristics ($I_{\text{DS}}-V_{\text{GG}}$) showed saturation stages of I_{DS} at V_{GG} of 6 V. At higher bias, the current increased more rapidly, possibly due to band-to-band tunneling. The field effect carrier mobilities μ_{FE} (without exclusion of R_{C}) ranged from 10.4 to 20 $\text{cm}^2\text{V}^{-1}\text{s}^{-1}$, comparable to the best results so far reported on monolayer MoS₂ at room temperature^{140,158,159}.

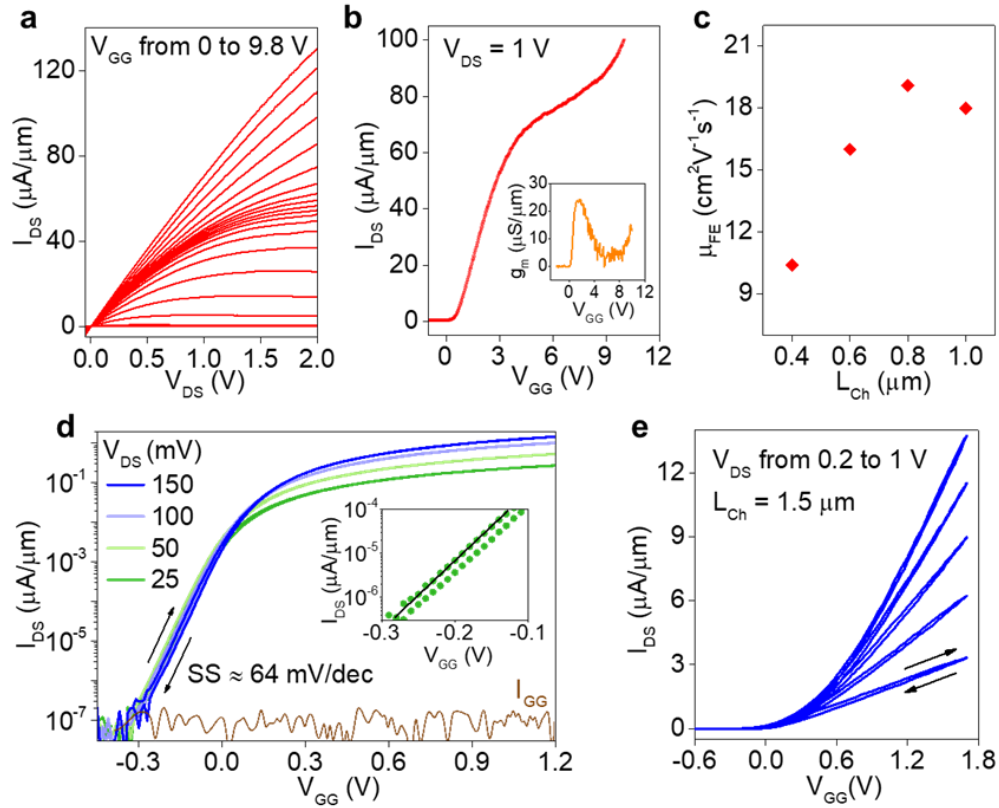


Figure 5.4: Electrical characterization of device performance. (a) – (c) Characterization of devices with $T_{Hf} = 16$ nm. (a) Output curves (I_{DS} as a function of V_{DS} at different V_{GG}) for a 600 nm long channel. V_{GG} increased from 0 to 9.5 V in 0.5 V steps, and then to 9.8 V. (b) Transport characteristics of a 400 nm channel. Inset: Transconductance g_m as a function of V_{GG} . (c) Field effect carrier mobilities (without exclusion of the contact resistance) at different channel length. (d) – (e) Transport characteristics of a device with $T_{Hf} = 8$ nm and $L_{Ch} = 1.5 \mu m$. (d) I_{DS} plotted in logarithmic scale, showing a SS of 64 mV/decade. Inset: zoom-in of the subthreshold regime; and (e) I_{DS} plotted in linear scale with V_{DS} increased up to 1 V and V_{GG} up to 1.7 V, which led to a high on/off ratio of 1.8×10^8 . Both (d) and (e) show very small hysteresis.

Figures 5.4d and 5.4e show the performance of a device with $L_{ch}=1.5 \mu\text{m}$, with the HfO_2 thickness reduced to 8 nm. The device exhibited a SS of 64 mV/decade over 3 orders of magnitude in I_{DS} , approaching the thermodynamic limit for field effect transistors at room temperature. Also, hysteresis was almost unrecognizable, allowing the device to be turned on and off at low gate voltages with a high on/off ratio of 1.8×10^8 . This low hysteresis indicates a lack of trapped charges in the dielectric stack, reflecting the lack of dangling bonds in graphene, clean transfer of MoS_2 , and high-quality HfO_2 growth.

5.2.3 Short-channel transistors

Finally, we examine more deeply scaled devices. In such devices, use of an ultrathin dielectric layer is critical to mitigate short channel effects such as the decrease in on/off ratio and increase in SS. In general, the length of the channel that can be effectively controlled by the gate should be 5 to 10 times the natural length scale $(\lambda)^{160}$, as a function of the dielectric constant and thickness of the gate dielectric layer. Here, we used 2.5 nm HfO_2 with 1.2 nm TiO_2 as the gate dielectric for fabrication of short-channel devices. Due to the high dielectric constant, λ for our device was approximately 0.9 nm, which should be suitable for devices with channels as short as ~ 10 nm. We fabricated 50 nm and 14 nm channels using e-beam lithography and lift-off methods. The gate leakage through the 3.7 nm oxide was on the level of 10 pA, which should still allow for effective gate modulation of the channel. The 50 nm device exhibited SS of 73 mV/decade, on-current exceeding $240 \mu\text{A}/\mu\text{m}$ and an on/off ratio of 3.5×10^7 (Figure 5.5) at V_{DS} of 1.6 V. The total source-drain resistance was $6.7 \text{ k}\Omega \cdot \mu\text{m}$, close to the value of $2R_C$ ($4.6 \text{ k}\Omega \cdot \mu\text{m}$) presented in Figure 2b. There was no appreciable saturation stage through the transport characteristics, reflecting that R_C rapidly decreased with V_{GG} to maintain a nearly linear increase

of I_{DS} . The 14 nm device showed slight short-channel effects, yet still reasonable SS of 86.5 mV/decade and on/off ratio of 3.3×10^6 . For both channel lengths, the on/off ratio decreased with V_{DS} but remained higher than 10^5 , demonstrating effective immunity to short-channel effects while the source and drain electrodes started to affect the channel conductance.

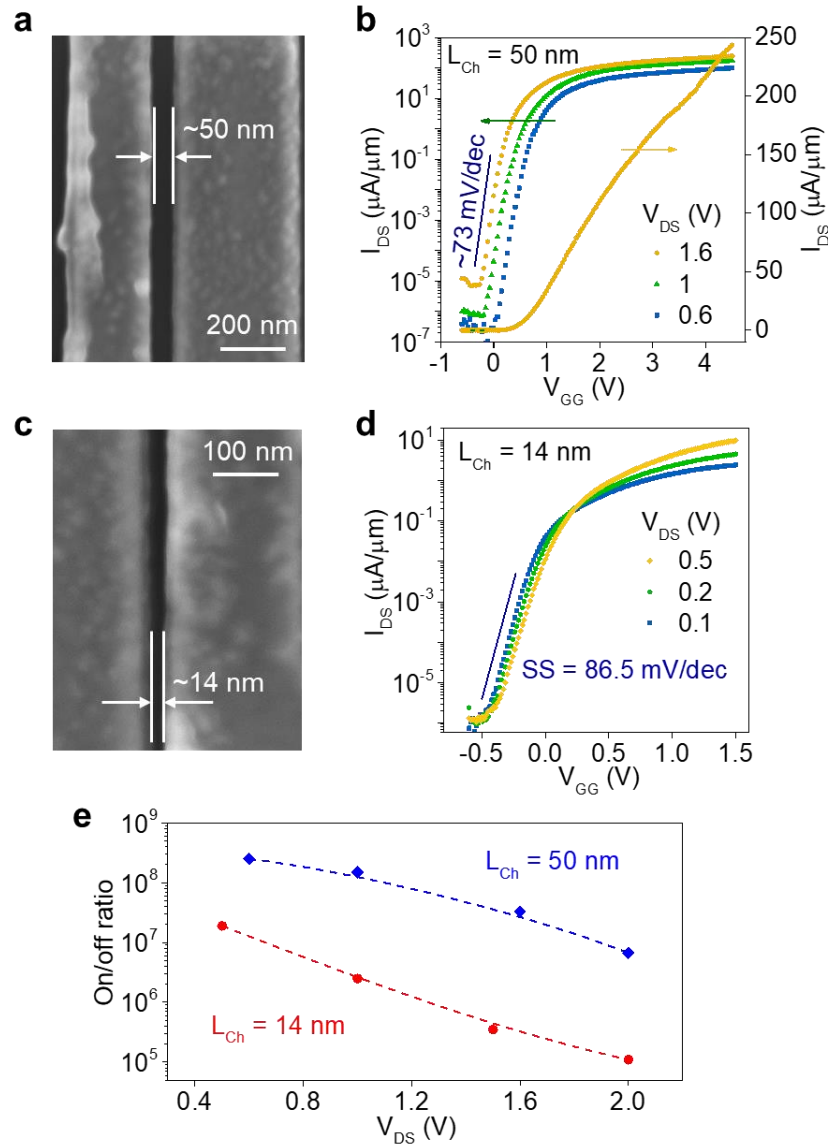


Figure 5.5: Characterization of short-channel devices. SEM photo and transport characteristics of a 50 nm channel (a-b) and a 14 nm channel (c-d). $T_{Hf} = 2.5$ nm. The SS was 73 mV/decade for the 50 nm channel and 86.5 mV/decade for the 14 nm channel. (e) On/off ratio as a function of

V_{DS} . The on/off ratio decreased with V_{DS} for both channels, reflecting that the source and drain electrodes started to control the channel conductance.

Overall, the results obtained with various T_{Ox} and L_{Ch} represent to date the best performance of intrinsic monolayer MoS_2 -based FET with standard device configuration, including direct metal contact, single-gate operation and solid dielectric. To satisfy the requirement of high-performance device, it is necessary to continue to lower the contact resistance and enhance the electrostatics¹⁶¹, which can be achieved by further device optimization such as passivation of the channel using boron nitride or use of 2D semiconductors with higher carrier mobilities, once large-scale synthesis of these materials is readily accessible.

5.2.4 Device performance on flexible substrate

The graphene gate also made the channel region fully transparent as desired in optical-related applications. The device can be fabricated on the transparent and flexible polymeric substrate thanks to the low temperature (200 °C) needed in the entire fabrication process. We preliminarily examined the performance of the device fabricated on polyethylene naphthalate (PEN) film. With 10 nm thick oxide layer sandwiched between the monolayer graphene and MoS_2 , the entire channel region was transparent under normal light conditions (Figure 5.6). Despite the increased gate leak, the thin film transistor exhibited excellent switching characteristics including a low SS of 75.5 mV/decade and an on/off ratio of 4.8×10^7 . The increase in the gate leak was attributable to the large roughness of the PEN and the strain built within the solid dielectric layer during fabrication and handling of the device. Better insulation of the dielectric under bending status

would be needed toward fully flexible and stretchable devices in the future, for example by reducing the surface roughness¹⁶² or using more flexible dielectric materials¹⁶³.

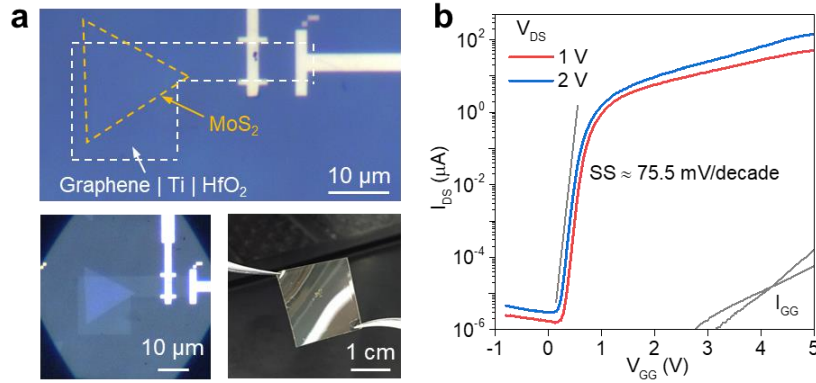


Figure 5.6: Characterization of the device fabricated on flexible PEN substrate. (a) Upper: Optical micrograph of the MoS₂ transferred on graphene gate. Lower left: High contrast micrograph for visualization of the MoS₂ flake and graphene gate. Lower right: Photograph of a fabricated device. (b) Transport characteristics of the device on flexible substrate.

5.3 Chapter summary

In this chapter, we presented monolayer MoS₂ transistors with single-atom thick graphene bottom local gate, of which the ultra-flat surface enabled use of ultra-thin gate dielectric. The decrease in the thickness of the gate dielectric improved the gate electrostatic control of the monolayer MoS₂ channel. An excellent subthreshold slope of 64 mV/decade was achieved. In addition, the gate leakage was also considerably suppressed compared to that on the metal gate, which in turn allowed us to more heavily dope the MoS₂ channel and lower the contact resistance between metal contact and MoS₂ monolayers. As such, both the extrinsic and intrinsic carrier mobility was increased, with a peak value of the extracted intrinsic mobility of $\sim 20 \text{ cm}^2\text{V}^{-1}\text{s}^{-1}$. We also demonstrated functionality of the MoS₂ channels as short as 14 nm using the graphene

bottom local-gate configuration. The on/off ration and the subthreshold slope did not show severe degradation, which serve strong evidence that the monolayer semiconductors would be ideal for use in developing extremely scaled electronic circuits. Finally, we characterized the device performance on flexible PEN substrate. Despite the larger surface roughness of the PEN than the polished SiO₂, the device still exhibited high transparency, low SS and high on/off ratio. Therefore, the graphene bottom local-gate have significantly improved the device performance over the metal gate as introduced in Chapter 3.

This design can be applied in various applications such as electronic circuits, display backplanes, biological sensors. Future study of the performance limit of the 2D semiconductors based devices includes further reducing the contact resistance by pretreatment of the materials, and development of integrated circuits.

Chapter 6

Conclusions and perspectives

6.1 Summary of contributions

Two-dimensional materials have become strong candidates for development of next-generation electronic devices. Their high sensitivity, optical transparency and mechanical flexibility are particularly attractive for biochemical sensing applications. The biosensors based on 2D materials, such as graphene, have been demonstrated in detection of various biomarkers such as protein and DNA, with high sensitivity and fast response. While the sensing principle for detection of these electrically charged, large molecules have been well studied, it remains challenging to quantitatively measure low-molecular-weight and charge-neutral analytes such as gas molecules as well as some organic chemicals.

This dissertation presents a study on the detection of small molecules using graphene field effect transistors, including an investigation of the sensing principles and improvement of the sensor design. Chapter 2 discusses the progress made toward time- and cost-efficient preparation of large-area graphene, which allows us to develop scalable graphene-based devices. Chapter 3 presents affinity binding-based glucose sensing on graphene FET sensors, study of the underlying physiochemical mechanism, as well as real-time monitoring of disease-related protein biomarkers on rigid and flexible substrates. Also, bottom local-gate graphene field effect biosensors are developed, which was more compact, integrable and stable than the solution-gated sensors. Chapter 4 introduces novel mid-infrared plasmonic biosensor based on the hybrid

graphene-metallic metasurface. Using the pure metallic metasurface we realized single measurement-based quantification and identification of protein molecules. By loading monolayer graphene on the metallic metasurface, we created a hybrid metasurface for ultrasensitive detection of small molecules. The metasurface based mid-IR biosensors addressed critical issues with existing optical biosensors such as insufficient sensitivities, and therefore hold promise in both fundamental studies and practical applications. Chapter 5 presents high-performance field effect transistors based on 2D semiconductors, i.e. MoS₂. Using monolayer graphene as the bottom local gate, we demonstrated high dielectric strength of the ultrathin gate dielectric as well as low contact resistance between metal and monolayer CVD MoS₂, which in turn allowed us to achieve nearly ideal switching characteristics as well as high-performance short-channel transistors.

6.2 Future work

The study and results presented in the thesis have demonstrated the unique and important functionalities of 2D materials in electronic and optoelectronic sensors. To ultimately achieve practical applications of such 2D material-based devices, more efficient methods for reliable preparation of high-quality 2D materials over very large areas must be developed. In particular, while the current CVD method and transfer process have enabled preparation of continuous graphene at the wafer scale for research purposes, further studies will be needed to realize defect-free and residue-free transfer of the wafer-scale single-crystal graphene on different substrates. The long-term stability of the 2D material-based devices also needs to be more systematically studied and improved. The highly sensitive biosensors based on the 2D materials now face interferences from background molecules, or biofouling issues in complex biochemical samples.

For example, passivation of graphene using appropriate coating nanolayers could improve the specificity and sensitivity of the sensors to target analytes.

In addition, to achieve deeply scaled devices, it would be required to not only fabricate very short channels, but also to ensure the efficient gate electrostatic control, low contact resistance and low subthreshold sweep with the short channels. Therefore, it is also important to accurately control the carrier density and maintain high carrier mobility of the 2D materials. Some of the current silicon-based methods, such as ion injection or chemical doping, may not be directly applicable to 2D materials. Controllable and nondestructive surface treatment, or heterostructures can possibly be used to further minimize the contact resistance between the 2D materials with the metal contacts. Other physical processes, such as annealing, can also be employed to improve the device performance.

Overall, to realize commercialization of the products based on 2D materials, the future studies should be focused on lowering the costs of wafer-scale single crystals and precise control of the material properties, together with enhancing the device performance. Rigorous international standards and quality control also need to be implemented to ensure device stability and device-to-device uniformity.

Bibliography

- 1 Duan, X. X., Li, Y., Rajan, N. K., Routenberg, D. A., Modis, Y. & Reed, M. A. Quantification of the affinities and kinetics of protein interactions using silicon nanowire biosensors. *Nat Nanotechnol* **7**, 401-407, (2012).
- 2 Kabashin, A. V., Evans, P., Pastkovsky, S., Hendren, W., Wurtz, G. A., Atkinson, R., Pollard, R., Podolskiy, V. A. & Zayats, A. V. Plasmonic nanorod metamaterials for biosensing. *Nat Mater* **8**, 867-871, (2009).
- 3 Luo, X. L., Morrin, A., Killard, A. J. & Smyth, M. R. Application of nanoparticles in electrochemical sensors and biosensors. *Electroanal* **18**, 319-326, (2006).
- 4 Jacobs, C. B., Peairs, M. J. & Venton, B. J. Review: Carbon nanotube based electrochemical sensors for biomolecules. *Anal Chim Acta* **662**, 105-127, (2010).
- 5 Huang, X., Leduc, C., Ravussin, Y., Li, S. Q., Davis, E., Song, B., Li, D. C., Xu, K. X., Accili, D., Wang, Q., Leibel, R. & Lin, Q. A differential dielectric affinity glucose sensor. *Lab Chip* **14**, 294-301, (2014).
- 6 Han, W. X., He, H. X., Zhang, L. L., Dong, C. Y., Zeng, H., Dai, Y. T., Xing, L. L., Zhang, Y. & Xue, X. Y. A Self-Powered Wearable Noninvasive Electronic-Skin for Perspiration Analysis Based on Piezo-Biosensing Unit Matrix of Enzyme/ZnO Nanoarrays. *Acs Appl Mater Inter* **9**, 29526-29537, (2017).
- 7 Cao, X. T., Cao, X., Guo, H. J., Li, T., Jie, Y., Wang, N. & Wang, Z. L. Piezotronic Effect Enhanced Label-Free Detection of DNA Using a Schottky-Contacted ZnO Nanowire Biosensor. *Acs Nano* **10**, 8038-8044, (2016).
- 8 Zhao, Y. Y., Fu, Y. M., Wang, P. L., Xing, L. L. & Xue, X. Y. Highly stable piezo-immunoglobulin-biosensing of a SiO₂/ZnO nanogenerator as a self-powered/active biosensor arising from the field effect influenced piezoelectric screening effect. *Nanoscale* **7**, 1904-1911, (2015).
- 9 Cao, C., Zhang, J., Wen, X. L., Dodson, S. L., Dao, N. T., Wong, L. M., Wang, S. J., Li, S. Z., Phan, A. T. & Xiong, Q. H. Metamaterials-Based Label-Free Nanosensor for Conformation and Affinity Biosensing. *Acs Nano* **7**, 7583-7591, (2013).
- 10 Kho, K. W., Dinish, U. S., Kumar, A. & Olivo, M. Frequency Shifts in SERS for Biosensing. *Acs Nano* **6**, 4892-4902, (2012).
- 11 Yu, C. X., Ganjoo, A., Jain, H., Pantano, C. G. & Irudayaraj, J. Mid-IR biosensor: Detection and fingerprinting of pathogens on gold island functionalized chalcogenide films. *Anal Chem* **78**, 2500-2506, (2006).
- 12 Ataka, K., Stripp, S. T. & Heberle, J. Surface-enhanced infrared absorption spectroscopy (SEIRAS) to probe monolayers of membrane proteins. *Bba-Biomembranes* **1828**, 2283-2293, (2013).

- 13 Xu, S. C., Zhan, J., Man, B. Y., Jiang, S. Z., Yue, W. W., Gao, S. B., Guo, C. G., Liu, H. P., Li, Z. H., Wang, J. H. & Zhou, Y. Q. Real-time reliable determination of binding kinetics of DNA hybridization using a multi-channel graphene biosensor. *Nat Commun* **8**, (2017).
- 14 Yetisen, A. K., Montelongo, Y., Vasconcellos, F. D., Martinez-Hurtado, J. L., Neupane, S., Butt, H., Qasim, M. M., Blyth, J., Burling, K., Carmody, J. B., Evans, M., Wilkinson, T. D., Kubota, L. T., Monteiro, M. J. & Lowe, C. R. Reusable, Robust, and Accurate Laser-Generated Photonic Nanosensor. *Nano Lett* **14**, 3587-3593, (2014).
- 15 Zhang, Y. D., Hei, T. T., Cai, Y. A., Gao, Q. Q. & Zhang, Q. Affinity Binding-Guided Fluorescent Nanobiosensor for Acetylcholinesterase Inhibitors via Distance Modulation between the Fluorophore and Metallic Nanoparticle. *Anal Chem* **84**, 2830-2836, (2012).
- 16 Zhu, A. Y., Yi, F., Reed, J. C., Zhu, H. & Cubukcu, E. Optoelectromechanical Multimodal Biosensor with Graphene Active Region. *Nano Lett* **14**, 5641-5649, (2014).
- 17 Novoselov, K. S., Geim, A. K., Morozov, S. V., Jiang, D., Katsnelson, M. I., Grigorieva, I. V., Dubonos, S. V. & Firsov, A. A. Two-dimensional gas of massless Dirac fermions in graphene. *Nature* **438**, 197-200, (2005).
- 18 Novoselov, K. S., Geim, A. K., Morozov, S. V., Jiang, D., Zhang, Y., Dubonos, S. V., Grigorieva, I. V. & Firsov, A. A. Electric field effect in atomically thin carbon films. *Science* **306**, 666-669, (2004).
- 19 Britnell, L., Gorbachev, R. V., Jalil, R., Belle, B. D., Schedin, F., Mishchenko, A., Georgiou, T., Katsnelson, M. I., Eaves, L., Morozov, S. V., Peres, N. M. R., Leist, J., Geim, A. K., Novoselov, K. S. & Ponomarenko, L. A. Field-Effect Tunneling Transistor Based on Vertical Graphene Heterostructures. *Science* **335**, 947-950, (2012).
- 20 Bonaccorso, F., Sun, Z., Hasan, T. & Ferrari, A. C. Graphene photonics and optoelectronics. *Nat Photonics* **4**, 611-622, (2010).
- 21 Heerema, S. J. & Dekker, C. Graphene nanodevices for DNA sequencing. *Nat Nanotechnol* **11**, 127-136, (2016).
- 22 Raccichini, R., Varzi, A., Passerini, S. & Scrosati, B. The role of graphene for electrochemical energy storage. *Nat Mater* **14**, 271-279, (2015).
- 23 Lee, C., Wei, X. D., Kysar, J. W. & Hone, J. Measurement of the elastic properties and intrinsic strength of monolayer graphene. *Science* **321**, 385-388, (2008).
- 24 Banszerus, L., Schmitz, M., Engels, S., Dauber, J., Oellers, M., Haupt, F., Watanabe, K., Taniguchi, T., Beschoten, B. & Stampfer, C. Ultrahigh-mobility graphene devices from chemical vapor deposition on reusable copper. *Sci Adv* **1**, (2015).
- 25 Akinwande, D., Petrone, N. & Hone, J. Two-dimensional flexible nanoelectronics. *Nat Commun* **5**, (2014).

- 26 Wang, Q. H., Kalantar-Zadeh, K., Kis, A., Coleman, J. N. & Strano, M. S. Electronics and optoelectronics of two-dimensional transition metal dichalcogenides. *Nat Nanotechnol* **7**, 699-712, (2012).
- 27 Radisavljevic, B., Radenovic, A., Brivio, J., Giacometti, V. & Kis, A. Single-layer MoS₂ transistors. *Nat Nanotechnol* **6**, 147-150, (2011).
- 28 Lee, G. H., Cui, X., Kim, Y. D., Arefe, G., Zhang, X., Lee, C. H., Ye, F., Watanabe, K., Taniguchi, T., Kim, P. & Hone, J. Highly Stable, Dual-Gated MoS₂ Transistors Encapsulated by Hexagonal Boron Nitride with Gate-Controllable Contact, Resistance, and Threshold Voltage. *Acs Nano* **9**, 7019-7026, (2015).
- 29 Ryou, J., Kim, Y. S., Santosh, K. C. & Cho, K. Monolayer MoS₂ Bandgap Modulation by Dielectric Environments and Tunable Bandgap Transistors. *Sci Rep-Uk* **6**, (2016).
- 30 Shulaker, M. M., Hills, G., Patil, N., Wei, H., Chen, H. Y., PhilipWong, H. S. & Mitra, S. Carbon nanotube computer. *Nature* **501**, 526+, (2013).
- 31 Holzinger, M., Le Goff, A. & Cosnier, S. Nanomaterials for biosensing applications: a review. *Front Chem* **2**, (2014).
- 32 Zhang, Y., Zhang, L. Y. & Zhou, C. W. Review of Chemical Vapor Deposition of Graphene and Related Applications. *Accounts Chem Res* **46**, 2329-2339, (2013).
- 33 Kim, K. S., Zhao, Y., Jang, H., Lee, S. Y., Kim, J. M., Kim, K. S., Ahn, J. H., Kim, P., Choi, J. Y. & Hong, B. H. Large-scale pattern growth of graphene films for stretchable transparent electrodes. *Nature* **457**, 706-710, (2009).
- 34 Hao, Y. F., Bharathi, M. S., Wang, L., Liu, Y. Y., Chen, H., Nie, S., Wang, X. H., Chou, H., Tan, C., Fallahazad, B., Ramanarayan, H., Magnuson, C. W., Tutuc, E., Yakobson, B. I., McCarty, K. F., Zhang, Y. W., Kim, P., Hone, J., Colombo, L. & Ruoff, R. S. The Role of Surface Oxygen in the Growth of Large Single-Crystal Graphene on Copper. *Science* **342**, 720-723, (2013).
- 35 Li, X. S., Colombo, L. & Ruoff, R. S. Synthesis of Graphene Films on Copper Foils by Chemical Vapor Deposition. *Adv Mater* **28**, 6247-6252, (2016).
- 36 Lee, H. C., Liu, W. W., Chai, S. P., Mohamed, A. R., Lai, C. W., Khe, C. S., Voon, C. H., Hashima, U. & Hidayah, N. M. S. Synthesis of Single-layer Graphene: A Review of Recent Development. *Procedia Chem* **19**, 916-921, (2016).
- 37 Tao, L., Lee, J., Holt, M., Chou, H., McDonnell, S. J., Ferrer, D. A., Babenco, M. G., Wallace, R. M., Banerjee, S. K., Ruoff, R. S. & Akinwande, D. Uniform Wafer-Scale Chemical Vapor Deposition of Graphene on Evaporated Cu (111) Film with Quality Comparable to Exfoliated Monolayer. *J Phys Chem C* **116**, 24068-24074, (2012).

- 38 Suk, J. W., Kitt, A., Magnuson, C. W., Hao, Y. F., Ahmed, S., An, J. H., Swan, A. K., Goldberg, B. B. & Ruoff, R. S. Transfer of CVD-Grown Monolayer Graphene onto Arbitrary Substrates. *Acs Nano* **5**, 6916-6924, (2011).
- 39 Feng, Y. & Chen, K. Dry transfer of chemical-vapor-deposition-grown graphene onto liquid-sensitive surfaces for tunnel junction applications. *Nanotechnology* **26**, (2015).
- 40 Gao, L. B., Ren, W. C., Xu, H. L., Jin, L., Wang, Z. X., Ma, T., Ma, L. P., Zhang, Z. Y., Fu, Q., Peng, L. M., Bao, X. H. & Cheng, H. M. Repeated growth and bubbling transfer of graphene with millimetre-size single-crystal grains using platinum. *Nat Commun* **3**, (2012).
- 41 Cherian, C. T., Giustiniano, F., Martin-Fernandez, I., Andersen, H., Balakrishnan, J. & Ozyilmaz, B. 'Bubble-Free' Electrochemical Delamination of CVD Graphene Films. *Small* **11**, 189-194, (2015).
- 42 Hao, Y. F., Wang, Y. Y., Wang, L., Ni, Z. H., Wang, Z. Q., Wang, R., Koo, C. K., Shen, Z. X. & Thong, J. T. L. Probing Layer Number and Stacking Order of Few-Layer Graphene by Raman Spectroscopy. *Small* **6**, 195-200, (2010).
- 43 Shearer, C. J., Slattery, A. D., Stapleton, A. J., Shapter, J. G. & Gibson, C. T. Accurate thickness measurement of graphene. *Nanotechnology* **27**, (2016).
- 44 Dean, C. R., Young, A. F., Meric, I., Lee, C., Wang, L., Sorgenfrei, S., Watanabe, K., Taniguchi, T., Kim, P., Shepard, K. L. & Hone, J. Boron nitride substrates for high-quality graphene electronics. *Nat Nanotechnol* **5**, 722-726, (2010).
- 45 Pizzocchero, F., Gammelgaard, L., Jessen, B. S., Caridad, J. M., Wang, L., Hone, J., Boggild, P. & Booth, T. J. The hot pick-up technique for batch assembly of van der Waals heterostructures. *Nat Commun* **7**, (2016).
- 46 Jang, C. W., Kim, J. H., Kim, J. M., Shin, D. H., Kim, S. & Choi, S. H. Rapid-thermal-annealing surface treatment for restoring the intrinsic properties of graphene field-effect transistors. *Nanotechnology* **24**, (2013).
- 47 Cheng, Z. G., Zhou, Q. Y., Wang, C. X., Li, Q. A., Wang, C. & Fang, Y. Toward Intrinsic Graphene Surfaces: A Systematic Study on Thermal Annealing and Wet-Chemical Treatment of SiO₂-Supported Graphene Devices. *Nano Lett* **11**, 767-771, (2011).
- 48 Choi, W., Shehzad, M. A., Park, S. & Seo, Y. Influence of removing PMMA residues on surface of CVD graphene using a contact-mode atomic force microscope. *Rsc Adv* **7**, 6943-6949, (2017).
- 49 Wood, J. D., Doidge, G. P., Carrion, E. A., Koepke, J. C., Kaitz, J. A., Datye, I., Behnam, A., Hewaparakrama, J., Aruin, B., Chen, Y. F., Dong, H., Haasch, R. T., Lyding, J. W. & Pop, E. Annealing free, clean graphene transfer using alternative polymer scaffolds. *Nanotechnology* **26**, (2015).

- 50 Bonaccorso, F., Lombardo, A., Hasan, T., Sun, Z. P., Colombo, L. & Ferrari, A. C. Production and processing of graphene and 2d crystals. *Mater Today* **15**, 564-589, (2012).
- 51 Chen, Y., Gong, X. L. & Gai, J. G. Progress and Challenges in Transfer of Large-Area Graphene Films. *Adv Sci* **3**, (2016).
- 52 Kaisti, M. Detection principles of biological and chemical FET sensors. *Biosens Bioelectron* **98**, 437-448, (2017).
- 53 Zanjani, S. M. M., Sadeghi, M. M., Holt, M., Chowdhury, S. F., Tao, L. & Akinwande, D. Enhanced sensitivity of graphene ammonia gas sensors using molecular doping. *Appl Phys Lett* **108**, (2016).
- 54 Zhang, C. C., Chen, P. L. & Hu, W. P. Organic field-effect transistor-based gas sensors. *Chem Soc Rev* **44**, 2087-2107, (2015).
- 55 Varghese, S. S., Lonkar, S., Singh, K. K., Swaminathan, S. & Abdala, A. Recent advances in graphene based gas sensors. *Sensor Actuat B-Chem* **218**, 160-183, (2015).
- 56 Liu, Y. X., Dong, X. C. & Chen, P. Biological and chemical sensors based on graphene materials. *Chem Soc Rev* **41**, 2283-2307, (2012).
- 57 Cervenka, J., Budi, A., Dontschuk, N., Stacey, A., Tadich, A., Rietwyk, K. J., Schenk, A., Edmonds, M. T., Yin, Y. F., Medhekar, N., Kalbac, M. & Pakes, C. I. Graphene field effect transistor as a probe of electronic structure and charge transfer at organic molecule-graphene interfaces. *Nanoscale* **7**, 1471-1478, (2015).
- 58 Dontschuk, N., Stacey, A., Tadich, A., Rietwyk, K. J., Schenk, A., Edmonds, M. T., Shimoni, O., Pakes, C. I., Praver, S. & Cervenka, J. A graphene field-effect transistor as a molecule-specific probe of DNA nucleobases. *Nat Commun* **6**, (2015).
- 59 Hao, Z., Zhu, Y. B., Wang, X. J., Rotti, P. G., DiMarco, C., Tyler, S. R., Zhao, X. Z., Engelhardt, J. F., Hone, J. & Lin, Q. Real-Time Monitoring of Insulin Using a Graphene Field-Effect Transistor Aptameric Nanosensor. *Acs Appl Mater Inter* **9**, 27504-27511, (2017).
- 60 Kong, J., Franklin, N. R., Zhou, C. W., Chapline, M. G., Peng, S., Cho, K. J. & Dai, H. J. Nanotube molecular wires as chemical sensors. *Science* **287**, 622-625, (2000).
- 61 Staii, C. & Johnson, A. T. DNA-decorated carbon nanotubes for chemical sensing. *Nano Lett* **5**, 1774-1778, (2005).
- 62 Schedin, F., Geim, A. K., Morozov, S. V., Hill, E. W., Blake, P., Katsnelson, M. I. & Novoselov, K. S. Detection of individual gas molecules adsorbed on graphene. *Nat Mater* **6**, 652-655, (2007).

- 63 Gao, N., Gao, T., Yang, X., Dai, X. C., Zhou, W., Zhang, A. Q. & Lieber, C. M. Specific detection of biomolecules in physiological solutions using graphene transistor biosensors. *P Natl Acad Sci USA* **113**, 14633-14638, (2016).
- 64 Kwak, Y. H., Choi, D. S., Kim, Y. N., Kim, H., Yoon, D. H., Ahn, S. S., Yang, J. W., Yang, W. S. & Seo, S. Flexible glucose sensor using CVD-grown graphene-based field effect transistor. *Biosens Bioelectron* **37**, 82-87, (2012).
- 65 Mansouri, S. & Schultz, J. S. A Miniature Optical Glucose Sensor Based on Affinity Binding. *Bio-Technol* **2**, 885-890, (1984).
- 66 Mansouri, S. & Schultz, J. S. A Miniature Optical Glucose Sensor Based on Affinity Binding. *Nat Biotechnol* **2**, 885-890, (1984).
- 67 Lei, M., Baldi, A., Nuxoll, E., Siegel, R. A. & Ziaie, B. A hydrogel-based implantable micromachined transponder for wireless glucose measurement. *Diabetes Technol The* **8**, 112-122, (2006).
- 68 Heo, Y. J., Shibata, H., Okitsu, T., Kawanishi, T. & Takeuchi, S. Long-term in vivo glucose monitoring using fluorescent hydrogel fibers. *P Natl Acad Sci USA* **108**, 13399-13403, (2011).
- 69 Shibata, H., Heo, Y. J., Okitsu, T., Matsunaga, Y., Kawanishi, T. & Takeuchi, S. Injectable hydrogel microbeads for fluorescence-based in vivo continuous glucose monitoring. *P Natl Acad Sci USA* **107**, 17894-17898, (2010).
- 70 Badugu, R., Lakowicz, J. R. & Geddes, C. D. Ophthalmic glucose sensing: a novel monosaccharide sensing disposable and colorless contact lens. *Analyst* **129**, 516-521, (2004).
- 71 Yan, Q. Y., Peng, B., Su, G., Cohan, B. E., Major, T. C. & Meyerhoff, M. E. Measurement of Tear Glucose Levels with Amperometric Glucose Biosensor/Capillary Tube Configuration. *Anal Chem* **83**, 8341-8346, (2011).
- 72 Jurysta, C., Bulur, N., Oguzhan, B., Satman, I., Yilmaz, T. M., Malaisse, W. J. & Sener, A. Salivary Glucose Concentration and Excretion in Normal and Diabetic Subjects. *J Biomed Biotechnol* **430426**, (2009).
- 73 Sen, D. K. & Sarin, G. S. Tear Glucose-Levels in Normal People and in Diabetic-Patients. *Brit J Ophthalmol* **64**, 693-695, (1980).
- 74 Zhang, L., Zhang, Z. Y., Liang, R. P., Li, Y. H. & Qiu, J. D. Boron-Doped Graphene Quantum Dots for Selective Glucose Sensing Based on the "Abnormal" Aggregation-Induced Photoluminescence Enhancement. *Anal Chem* **86**, 4423-4430, (2014).
- 75 Lerner, M. B., Kybert, N., Mendoza, R., Villechenon, R., Lopez, M. A. B. & Johnson, A. T. C. Scalable, non-invasive glucose sensor based on boronic acid functionalized carbon nanotube transistors. *Appl Phys Lett* **102**, (2013).

- 76 Huang, X., Li, S. Q., Davis, E., Leduc, C., Ravussin, Y., Cai, H. G., Song, B., Li, D. C., Accili, D., Leibel, R., Wang, Q. & Lin, Q. A MEMS differential viscometric sensor for affinity glucose detection in continuous glucose monitoring. *J Micromech Microeng* **23**, (2013).
- 77 Yoon, G. Dielectric properties of glucose in bulk aqueous solutions: Influence of electrode polarization and modeling. *Biosens Bioelectron* **26**, 2347-2353, (2011).
- 78 Li, X. S., Cai, W. W., An, J. H., Kim, S., Nah, J., Yang, D. X., Piner, R., Velamakanni, A., Jung, I., Tutuc, E., Banerjee, S. K., Colombo, L. & Ruoff, R. S. Large-Area Synthesis of High-Quality and Uniform Graphene Films on Copper Foils. *Science* **324**, 1312-1314, (2009).
- 79 Li, J. W., Liu, Y. Y., Qian, Y., Li, L., Xie, L. H., Shang, J. Z., Yu, T., Yi, M. D. & Huang, W. Describing curved-planar pi-pi interactions: modeled by corannulene, pyrene and coronene. *Phys Chem Chem Phys* **15**, 12694-12701, (2013).
- 80 Li, S. S., Zhou, Q., Chu, W. Y., Zhao, W. & Zheng, J. W. Surface-enhanced Raman scattering behaviour of 4-mercaptophenyl boronic acid on assembled silver nanoparticles. *Phys Chem Chem Phys* **17**, 17638-17645, (2015).
- 81 Krishnan, K. The Raman spectrum of boric acid. *Proc. Indian Acad. Sci.* **57**, 103-108, (1963).
- 82 Dong, X. C., Fu, D. L., Fang, W. J., Shi, Y. M., Chen, P. & Li, L. J. Doping Single-Layer Graphene with Aromatic Molecules. *Small* **5**, 1422-1426, (2009).
- 83 Das, A., Pisana, S., Chakraborty, B., Piscanec, S., Saha, S. K., Waghmare, U. V., Novoselov, K. S., Krishnamurthy, H. R., Geim, A. K., Ferrari, A. C. & Sood, A. K. Monitoring dopants by Raman scattering in an electrochemically top-gated graphene transistor. *Nat Nanotechnol* **3**, 210-215, (2008).
- 84 Farmer, D. B., Golizadeh-Mojarad, R., Perebeinos, V., Lin, Y. M., Tulevski, G. S., Tsang, J. C. & Avouris, P. Chemical Doping and Electron-Hole Conduction Asymmetry in Graphene Devices. *Nano Lett* **9**, 388-392, (2009).
- 85 Ciftci, H., Tamer, U., Sen Teker, M. & Pekmez, N. O. An enzyme free potentiometric detection of glucose based on a conducting polymer poly (3-aminophenyl boronic acid-co-3-octylthiophene). *Electrochim Acta* **90**, 358-365, (2013).
- 86 Shoji, E. & Freund, M. S. Potentiometric saccharide detection based on the pKa changes of poly(aniline boronic acid). *J Am Chem Soc* **124**, 12486-12493, (2002).
- 87 Kawasaki, T., Akanuma, H. & Yamanouchi, T. Y. Increased fructose concentrations in blood and urine in patients with diabetes. *Diabetes Care* **25**, 353-357, (2002).
- 88 Sugnaux, C. & Klok, H. A. Glucose-Sensitive QCM-Sensors Via Direct Surface RAFT Polymerization. *Macromol Rapid Comm* **35**, 1402-1407, (2014).

- 89 Wu, X., Li, Z., Chen, X.-X., Fossey, J. S., James, T. D. & Jiang, Y.-B. Selective sensing of saccharides using simple boronic acids and their aggregates. *Chem Soc Rev* **42**, 8032-8048, (2013).
- 90 Olansky, L. & Kennedy, L. Finger-stick glucose monitoring issues of accuracy and specificity. *Diabetes Care* **33**, 948-949, (2010).
- 91 Vashist, S. K. Continuous glucose monitoring systems: A review. *Diagnostics* **3**, 385-412, (2013).
- 92 El-Khatib, F. H., Russell, S. J., Nathan, D. M., Sutherlin, R. G. & Damiano, E. R. A bihormonal closed-loop artificial pancreas for type 1 diabetes. *Science translational medicine* **2**, 27ra27-27ra27, (2010).
- 93 Gerasimov, J. Y., Schaefer, C. S., Yang, W., Grout, R. L. & Lai, R. Y. Development of an electrochemical insulin sensor based on the insulin-linked polymorphic region. *Biosensors and Bioelectronics* **42**, 62-68, (2013).
- 94 Gosling, J. P. A decade of development in immunoassay methodology. *Clinical Chemistry* **36**, 1408-1427, (1990).
- 95 Pu, Y., Zhu, Z., Han, D., Liu, H., Liu, J., Liao, J., Zhang, K. & Tan, W. Insulin-binding aptamer-conjugated graphene oxide for insulin detection. *Analyst* **136**, 4138-4140, (2011).
- 96 Kubo, I. & Eguchi, T. Study on Electrochemical Insulin Sensing Utilizing a DNA Aptamer-Immobilized Gold Electrode. *Materials* **8**, 4710-4719, (2015).
- 97 Cha, T.-G., Baker, B. A., Sauffer, M. D., Salgado, J., Jaroch, D., Rickus, J. L., Porterfield, D. M. & Choi, J. H. Optical nanosensor architecture for cell-signaling molecules using DNA aptamer-coated carbon nanotubes. *Acs Nano* **5**, 4236-4244, (2011).
- 98 Vignali, D. A. Multiplexed particle-based flow cytometric assays. *Journal of immunological methods* **243**, 243-255, (2000).
- 99 Kunkel, A., Gunter, S., Dette, C. & Watzig, H. Quantitation of insulin by capillary electrophoresis and high-performance liquid chromatography - Method comparison and validation. *J Chromatogr A* **781**, 445-455, (1997).
- 100 Wang, Y. & Li, J. H. A carbon nanotubes assisted strategy for insulin detection and insulin proteolysis assay. *Anal Chim Acta* **650**, 49-53, (2009).
- 101 Ristein, J. Surface transfer doping of semiconductors. *Science* **313**, 1057-1058, (2006).
- 102 Williams, J. R., Low, T., Lundstrom, M. S. & Marcus, C. M. Gate-controlled guiding of electrons in graphene. *Nat Nanotechnol* **6**, 222-225, (2011).
- 103 Chen, J. H., Jang, C., Adam, S., Fuhrer, M. S., Williams, E. D. & Ishigami, M. Charged-impurity scattering in graphene. *Nat Phys* **4**, 377-381, (2008).

- 104 Xia, J. L., Chen, F., Wiktor, P., Ferry, D. K. & Tao, N. J. Effect of Top Dielectric Medium on Gate Capacitance of Graphene Field Effect Transistors: Implications in Mobility Measurements and Sensor Applications. *Nano Lett* **10**, 5060-5064, (2010).
- 105 Mailly-Giacchetti, B., Hsu, A., Wang, H., Vinciguerra, V., Pappalardo, F., Occhipinti, L., Guidetti, E., Coffa, S., Kong, J. & Palacios, T. pH sensing properties of graphene solution-gated field-effect transistors. *J Appl Phys* **114**, (2013).
- 106 Feiner, A. S. & Mcevoy, A. J. The Nernst Equation. *J Chem Educ* **71**, 493-494, (1994).
- 107 Kim, S., Nah, J., Jo, I., Shahrjerdi, D., Colombo, L., Yao, Z., Tutuc, E. & Banerjee, S. K. Realization of a high mobility dual-gated graphene field-effect transistor with Al₂O₃ dielectric. *Appl Phys Lett* **94**, (2009).
- 108 Meric, I., Han, M. Y., Young, A. F., Ozyilmaz, B., Kim, P. & Shepard, K. L. Current saturation in zero-bandgap, topgated graphene field-effect transistors. *Nat Nanotechnol* **3**, 654-659, (2008).
- 109 Xia, J. L., Chen, F., Li, J. H. & Tao, N. J. Measurement of the quantum capacitance of graphene. *Nat Nanotechnol* **4**, 505-509, (2009).
- 110 Wang, H. M., Wu, Y. H., Cong, C. X., Shang, J. Z. & Yu, T. Hysteresis of Electronic Transport in Graphene Transistors. *Acs Nano* **4**, 7221-7228, (2010).
- 111 Cooper, M. A. Optical biosensors in drug discovery. *Nat Rev Drug Discov* **1**, 515-528, (2002).
- 112 Mayer, K. M. & Hafner, J. H. Localized Surface Plasmon Resonance Sensors. *Chem Rev* **111**, 3828-3857, (2011).
- 113 Yang, H. Y., Yang, S. N., Kong, J. L., Dong, A. C. & Yu, S. N. Obtaining information about protein secondary structures in aqueous solution using Fourier transform IR spectroscopy. *Nat Protoc* **10**, (2015).
- 114 Reuel, N. F., Grassbaugh, B., Kruss, S., Mundy, J. Z., Opel, C., Ogunniyi, A. O., Egodage, K., Wahl, R., Helk, B., Zhang, J. Q., Kalcioglu, Z. I., Tvrdy, K., Bellisario, D. O., Mu, B., Blake, S. S., Van Vliet, K. J., Love, J. C., Wittrup, K. D. & Strano, M. S. Emergent Properties of Nanosensor Arrays: Applications for Monitoring IgG Affinity Distributions, Weakly Affined Hypermannosylation, and Colony Selection for Biomanufacturing. *Acs Nano* **7**, 7472-7482, (2013).
- 115 Limaj, O., Etezadi, D., Wittenberg, N. J., Rodrigo, D., Yoo, D. H., Oh, S. H. & Altug, H. Infrared Plasmonic Biosensor for Real-Time and Label-Free Monitoring of Lipid Membranes. *Nano Lett* **16**, 1502-1508, (2016).
- 116 Pleitez, M. A., Lieblein, T., Bauer, A., Hertzberg, O., von Lilienfeld-Toal, H. & Mantele, W. In Vivo Noninvasive Monitoring of Glucose Concentration in Human Epidermis by Mid-Infrared Pulsed Photoacoustic Spectroscopy. *Anal Chem* **85**, 1013-1020, (2013).

- 117 Kim, J., Son, H., Cho, D. J., Geng, B. S., Regan, W., Shi, S. F., Kim, K., Zettl, A., Shen, Y. R. & Wang, F. Electrical Control of Optical Plasmon Resonance with Graphene. *Nano Lett* **12**, 5598-5602, (2012).
- 118 Medina, H., Lin, Y. C., Obergfell, D. & Chiu, P. W. Tuning of Charge Densities in Graphene by Molecule Doping. *Adv Funct Mater* **21**, 2687-2692, (2011).
- 119 Dong, X. C., Shi, Y. M., Huang, W., Chen, P. & Li, L. J. Electrical Detection of DNA Hybridization with Single-Base Specificity Using Transistors Based on CVD-Grown Graphene Sheets. *Adv Mater* **22**, 1649-+, (2010).
- 120 Wang, C., Li, Y., Zhu, Y., Zhou, X., Lin, Q. & He, M. High-kappa Solid-Gate Transistor Configured Graphene Biosensor with Fully Integrated Structure and Enhanced Sensitivity (vol 42, pg 7668, 2016). *Adv Funct Mater* **26**, 8575-8575, (2016).
- 121 Yao, Y., Kats, M. A., Genevet, P., Yu, N. F., Song, Y., Kong, J. & Capasso, F. Broad Electrical Tuning of Graphene-Loaded Plasmonic Antennas. *Nano Lett* **13**, 1257-1264, (2013).
- 122 Lerner, M. B., Reszczenski, J. M., Amin, A., Johnson, R. R., Goldsmith, J. I. & Johnson, A. T. C. Toward Quantifying the Electrostatic Transduction Mechanism in Carbon Nanotube Molecular Sensors. *J Am Chem Soc* **134**, 14318-14321, (2012).
- 123 Wu, X., Li, Z., Chen, X. X., Fossey, J. S., James, T. D. & Jiang, Y. B. Selective sensing of saccharides using simple boronic acids and their aggregates. *Chem Soc Rev* **42**, 8032-8048, (2013).
- 124 Zhu, Y. B., Hao, Y. F., Adogla, E. A., Yan, J., Li, D. C., Xu, K. X., Wang, Q., Honea, J. & Lin, Q. A graphene-based affinity nanosensor for detection of low-charge and low-molecular-weight molecules. *Nanoscale* **8**, 5815-5819, (2016).
- 125 Mesch, M., Zhang, C. J., Braun, P. V. & Giessen, H. Functionalized Hydrogel on Plasmonic Nanoantennas for Noninvasive Glucose Sensing. *Acs Photonics* **2**, 475-480, (2015).
- 126 Li, D. C., Wu, J. W., Wu, P., Lin, Y., Sun, Y. J., Zhu, R., Yang, J. & Xu, K. X. Affinity based glucose measurement using fiber optic surface plasmon resonance sensor with surface modification by borate polymer. *Sensor Actuat B-Chem* **213**, 295-304, (2015).
- 127 Anker, J. N., Hall, W. P., Lyandres, O., Shah, N. C., Zhao, J. & Van Duyne, R. P. Biosensing with plasmonic nanosensors. *Nat Mater* **7**, 442-453, (2008).
- 128 Shao, D., Tang, D. P., Mai, Y. J. & Zhang, L. Z. Nanostructured silicon/porous carbon spherical composite as a high capacity anode for Li-ion batteries. *J Mater Chem A* **1**, 15068-15075, (2013).

- 129 Han, J. S., Zhang, J. J., Yang, M., Cui, D. X. & de la Fuente, J. M. Glucose-functionalized Au nanoprisms for optoacoustic imaging and near-infrared photothermal therapy (vol 8, pg 492, 2016). *Nanoscale* **8**, 1704-1704, (2016).
- 130 Liu, Y. S., Hu, W. H., Lu, Z. S. & Li, C. M. Photografted poly(methyl methacrylate)-based high performance protein microarray for hepatitis B virus biomarker detection in human serum. *Medchemcomm* **1**, 132-135, (2010).
- 131 Wang, Z., Dong, Z. G., Gu, Y. H., Chang, Y. H., Zhang, L., Li, L. J., Zhao, W. J., Eda, G., Zhang, W. J., Grinblat, G., Maier, S. A., Yang, J. K. W., Qiu, C. W. & Wee, A. T. S. Giant photoluminescence enhancement in tungsten-diselenide-gold plasmonic hybrid structures. *Nat Commun* **7**, (2016).
- 132 Rivera, P., Schaibley, J. R., Jones, A. M., Ross, J. S., Wu, S. F., Aivazian, G., Klement, P., Seyler, K., Clark, G., Ghimire, N. J., Yan, J. Q., Mandrus, D. G., Yao, W. & Xu, X. D. Observation of long-lived interlayer excitons in monolayer MoSe₂-WSe₂ heterostructures. *Nat Commun* **6**, (2015).
- 133 Yin, Z. Y., Li, H., Li, H., Jiang, L., Shi, Y. M., Sun, Y. H., Lu, G., Zhang, Q., Chen, X. D. & Zhang, H. Single-Layer MoS₂ Phototransistors. *Acs Nano* **6**, 74-80, (2012).
- 134 Loan, P. T. K., Zhang, W. J., Lin, C. T., Wei, K. H., Li, L. J. & Chen, C. H. Graphene/MoS₂ Heterostructures for Ultrasensitive Detection of DNA Hybridisation. *Adv Mater* **26**, 4838+, (2014).
- 135 Benameur, M. M., Radisavljevic, B., Heron, J. S., Sahoo, S., Berger, H. & Kis, A. Visibility of dichalcogenide nanolayers. *Nanotechnology* **22**, (2011).
- 136 Coleman, J. N., Lotya, M., O'Neill, A., Bergin, S. D., King, P. J., Khan, U., Young, K., Gaucher, A., De, S., Smith, R. J., Shvets, I. V., Arora, S. K., Stanton, G., Kim, H. Y., Lee, K., Kim, G. T., Duesberg, G. S., Hallam, T., Boland, J. J., Wang, J. J., Donegan, J. F., Grunlan, J. C., Moriarty, G., Shmeliov, A., Nicholls, R. J., Perkins, J. M., Grievson, E. M., Theuwissen, K., McComb, D. W., Nellist, P. D. & Nicolosi, V. Two-Dimensional Nanosheets Produced by Liquid Exfoliation of Layered Materials. *Science* **331**, 568-571, (2011).
- 137 Smith, R. J., King, P. J., Lotya, M., Wirtz, C., Khan, U., De, S., O'Neill, A., Duesberg, G. S., Grunlan, J. C., Moriarty, G., Chen, J., Wang, J. Z., Minett, A. I., Nicolosi, V. & Coleman, J. N. Large-Scale Exfoliation of Inorganic Layered Compounds in Aqueous Surfactant Solutions. *Adv Mater* **23**, 3944+, (2011).
- 138 Zhou, K. G., Mao, N. N., Wang, H. X., Peng, Y. & Zhang, H. L. A Mixed-Solvent Strategy for Efficient Exfoliation of Inorganic Graphene Analogues. *Angew Chem Int Edit* **50**, 10839-10842, (2011).

- 139 Kang, K., Lee, K. H., Han, Y. M., Gao, H., Xie, S. E., Muller, D. A. & Park, J. Layer-by-layer assembly of two-dimensional materials into wafer-scale heterostructures. *Nature* **550**, 229-233, (2017).
- 140 Kang, K., Xie, S. E., Huang, L. J., Han, Y. M., Huang, P. Y., Mak, K. F., Kim, C. J., Muller, D. & Park, J. High-mobility three-atom-thick semiconducting films with wafer-scale homogeneity. *Nature* **520**, 656-660, (2015).
- 141 Zhao, J., Yu, H., Chen, W., Yang, R., Zhu, J. Q., Liao, M. Z., Shi, D. X. & Zhang, G. Y. Patterned Peeling 2D MoS₂ off the Substrate. *Acs Appl Mater Inter* **8**, 16546-16550, (2016).
- 142 Lai, S., Jeon, J., Song, Y. J. & Lee, S. Water-penetration-assisted mechanical transfer of large-scale molybdenum disulfide onto arbitrary substrates. *Rsc Adv* **6**, S7497-S7501, (2016).
- 143 Franklin, A. D. & Chen, Z. H. Length scaling of carbon nanotube transistors. *Nat Nanotechnol* **5**, 858-862, (2010).
- 144 Qiu, C. G., Zhang, Z. Y., Xiao, M. M., Yang, Y. J., Zhong, D. L. & Peng, L. M. Scaling carbon nanotube complementary transistors to 5-nm gate lengths. *Science* **355**, 271-+, (2017).
- 145 Desai, S. B., Madhvapathy, S. R., Sachid, A. B., Llinas, J. P., Wang, Q. X., Ahn, G. H., Pitner, G., Kim, M. J., Bokor, J., Hu, C. M., Wong, H. S. P. & Javey, A. MoS₂ transistors with 1-nanometer gate lengths. *Science* **354**, 99-102, (2016).
- 146 Cheng, R., Jiang, S., Chen, Y., Liu, Y., Weiss, N., Cheng, H. C., Wu, H., Huang, Y. & Duan, X. F. Few-layer molybdenum disulfide transistors and circuits for high-speed flexible electronics. *Nat Commun* **5**, (2014).
- 147 Ferain, I., Colinge, C. A. & Colinge, J. P. Multigate transistors as the future of classical metal-oxide-semiconductor field-effect transistors. *Nature* **479**, 310-316, (2011).
- 148 McDonnell, S., Brennan, B., Azcatl, A., Lu, N., Dong, H., Buie, C., Kim, J., Hinkle, C. L., Kim, M. J. & Wallace, R. M. HfO₂ on MoS₂ by Atomic Layer Deposition: Adsorption Mechanisms and Thickness Scalability. *Acs Nano* **7**, 10354-10361, (2013).
- 149 Kim, S., Konar, A., Hwang, W. S., Lee, J. H., Lee, J., Yang, J., Jung, C., Kim, H., Yoo, J. B., Choi, J. Y., Jin, Y. W., Lee, S. Y., Jena, D., Choi, W. & Kim, K. High-mobility and low-power thin-film transistors based on multilayer MoS₂ crystals. *Nat Commun* **3**, (2012).
- 150 Xu, J., Chen, L., Dai, Y. W., Cao, Q., Sun, Q. Q., Ding, S. J., Zhu, H. & Zhang, D. W. A two-dimensional semiconductor transistor with boosted gate control and sensing ability. *Sci Adv* **3**, (2017).

- 151 Perera, M. M., Lin, M. W., Chuang, H. J., Chamlagain, B. P., Wang, C. Y., Tan, X. B., Cheng, M. M. C., Tomanek, D. & Zhou, Z. X. Improved Carrier Mobility in Few-Layer MoS₂ Field-Effect Transistors with Ionic-Liquid Gating. *Acs Nano* **7**, 4449-4458, (2013).
- 152 Zou, X. M., Wang, J. L., Chiu, C. H., Wu, Y., Xiao, X. H., Jiang, C. Z., Wu, W. W., Mai, L. Q., Chen, T. S., Li, J. C., Ho, J. C. & Liao, L. Interface Engineering for High-Performance Top-Gated MoS₂ Field-Effect Transistors. *Adv Mater* **26**, 6255-6261, (2014).
- 153 Lee, J. H., Lee, E. K., Joo, W. J., Jang, Y., Kim, B. S., Lim, J. Y., Choi, S. H., Ahn, S. J., Ahn, J. R., Park, M. H., Yang, C. W., Choi, B. L., Hwang, S. W. & Whang, D. Wafer-Scale Growth of Single-Crystal Monolayer Graphene on Reusable Hydrogen-Terminated Germanium. *Science* **344**, 286-289, (2014).
- 154 Xie, L., Liao, M. Z., Wang, S. P., Yu, H., Du, L. J., Tang, J., Zhao, J., Zhang, J., Chen, P., Lu, X. B., Wang, G. L., Xie, G. B., Yang, R., Shi, D. X. & Zhang, G. Y. Graphene-Contacted Ultrashort Channel Monolayer MoS₂ Transistors. *Adv Mater* **29**, (2017).
- 155 Jandhyala, S., Mordi, G., Lee, B., Lee, G., Floresca, C., Cha, P. R., Ahn, J., Wallace, R. M., Chabal, Y. J., Kim, M. J., Colombo, L., Cho, K. & Kim, J. Atomic Layer Deposition of Dielectrics on Graphene Using Reversibly Physisorbed Ozone. *Acs Nano* **6**, 2722-2730, (2012).
- 156 Si, M., Su, C.-J., Jiang, C., Conrad, N. J., Zhou, H., Maize, K. D., Qiu, G., Wu, C.-T., Shakouri, A., Alam, M. A. & Ye, P. D. Steep-slope hysteresis-free negative capacitance MoS₂ transistors. *Nat Nanotechnol*, (2017).
- 157 Liu, Y., Guo, J., Wu, Y. C., Zhu, E. B., Weiss, N. O., He, Q. Y., Wu, H., Cheng, H. C., Xu, Y., Shakir, I., Huang, Y. & Duan, X. Pushing the Performance Limit of Sub-100 nm Molybdenum Disulfide Transistors. *Nano Lett* **16**, 6337-6342, (2016).
- 158 English, C. D., Shine, G., Dorgan, V. E., Saraswat, K. C. & Pop, E. Improved Contacts to MoS₂ Transistors by Ultra-High Vacuum Metal Deposition. *Nano Lett* **16**, 3824-3830, (2016).
- 159 Liu, H., Si, M. W., Najmaei, S., Neal, A. T., Du, Y. C., Ajayan, P. M., Lou, J. & Ye, P. D. Statistical Study of Deep Submicron Dual-Gated Field-Effect Transistors on Monolayer Chemical Vapor Deposition Molybdenum Disulfide Films. *Nano Lett* **13**, 2640-2646, (2013).
- 160 Sarkar, D., Liu, W., Xie, X. J., Anselmo, A. C., Mitragotri, S. & Banerjee, K. MoS₂ Field-Effect Transistor for Next-Generation Label-Free Biosensors. *Acs Nano* **8**, 3992-4003, (2014).
- 161 Cao, W., Kang, J. H., Sarkar, D., Liu, W. & Banerjee, K. 2D Semiconductor FETs-Projections and Design for Sub-10 nm VLSI. *Ieee T Electron Dev* **62**, 3459-3469, (2015).

- 162 Chang, H. Y., Yang, S. X., Lee, J. H., Tao, L., Hwang, W. S., Jena, D., Lu, N. S. & Akinwande, D. High-Performance, Highly Bendable MoS₂ Transistors with High-K Dielectrics for Flexible Low-Power Systems. *Acs Nano* **7**, 5446-5452, (2013).
- 163 Lee, G. H., Yu, Y. J., Cui, X., Petrone, N., Lee, C. H., Choi, M. S., Lee, D. Y., Lee, C., Yoo, W. J., Watanabe, K., Taniguchi, T., Nuckolls, C., Kim, P. & Hone, J. Flexible and Transparent MoS₂ Field-Effect Transistors on Hexagonal Boron Nitride-Graphene Heterostructures. *Acs Nano* **7**, 7931-7936, (2013).